TU Delft

Delft University of Technology

Rayleigh-Bénard convection of a supercritical fluid
PIV and heat transfer study

Valori, Valentina

DOI
10.4233/uuid:9aca5d9a-df0a-4f73-aab6-669681a4f327

Publication date
2018

Document Version
Final published version

Citation (APA)
Valori, V. (2018). *Rayleigh-Bénard convection of a supercritical fluid: PIV and heat transfer study*. [Dissertation (TU Delft), Delft University of Technology]. https://doi.org/10.4233/uuid:9aca5d9a-df0a-4f73-aab6-669681a4f327

Important note
To cite this publication, please use the final published version (if applicable).
Please check the document version above.

Copyright
Other than for strictly personal use, it is not permitted to download, forward or distribute the text or part of it, without the consent of the author(s) and/or copyright holder(s), unless the work is under an open content license such as Creative Commons.

Takedown policy
Please contact us and provide details if you believe this document breaches copyrights.
We will remove access to the work immediately and investigate your claim.

This work is downloaded from Delft University of Technology.
For technical reasons the number of authors shown on this cover page is limited to a maximum of 10.

Rayleigh-Bénard convection of a supercritical fluid:

PIV and heat transfer study

Proefschrift

ter verkrijging van de graad van doctor
aan de Technische Universiteit Delft,
op gezag van de Rector Magnificus prof. dr. ir. T. H. J. J. van der Hagen,
voorzitter van het College voor Promoties,
in het openbaar te verdedigen op maandag 8 januari 2018 om 12:30 uur

door

Valentina VALORI

Master in Energy Engineering,
Università di Pisa, Italië,
geboren te Città di Castello, Italië.

Dit proefschrift is goedgekeurd door de promotoren:

Prof. dr. ir. T. H. J. J. van der Hagen & prof. dr. ir. J. Westerweel
Copromotor: Dr. ir. M. Rohde

Samenstelling promotiecommissie:

Rector Magnificus,	voorzitter
Prof. dr. ir. T. H. J. J. van der Hagen,	Technische Universiteit Delft, promotor
Prof. dr. ir. J. Westerweel,	Technische Universiteit Delft, promotor
Dr. ir. M. Rohde,	Technische Universiteit Delft, copromotor
Onafhankelijke leden:	
Prof. dr. H.-M. Prasser,	Eidgenössische Technische Hochschule Zürich
Prof. dr. S. He,	University of Sheffield
Prof. dr. H.J.H. Clercx,	Technische Universiteit Eindhoven
Prof. dr. F. Scarano,	Technische Universiteit Delft
Prof. dr. ir. C. Poelma	Technische Universiteit Delft, reservelid

This work is part of the research project number 12261, financed by the Dutch Technology Foundation (STW), which is part of the Netherlands Organisation for Scientific Research (NWO).

The printing of this thesis was partially founded by the Faculty of Applied Sciences of TU Delft, Radiation Science and Technology department, Reactor Physics and Nuclear Materials group, and partially by STW.

Keywords: supercritical fluids, Rayleigh-Bénard convection, particle image velocimetry, heat transfer, optical distortions.

Printed by: Gildeprint, https://www.gildeprint.nl/

Front: Experimentally obtained, time-average velocity field of Rayleigh-Bénard convection of a supercritical fluid, on a vertical cross-section of a cubical cell, at half depth.

Back: Black dots that symbolically represent the location of experimental data points, while their background symbolically represents a color coding of the values of a fluid property in the supercritical region.

Copyright © 2018 by V. Valori

ISBN 978-94-6233-856-2

An electronic version of this dissertation is available at
http://repository.tudelft.nl/.

Contents

Summary vii

Samenvatting ix

1 Introduction 1
- 1.1 Background and motivation . . . 1
  - 1.1.1 Experiments in fluids with strongly variable fluid properties . . . 5
- 1.2 Aim of this research . . . 6
  - 1.2.1 Experimental campaign . . . 7
- 1.3 Thesis outline . . . 7

References . . . 8

2 Non-Oberbeck-Boussinesq effects in Rayleigh-Bénard convection 11
- 2.1 Introduction . . . 11
- 2.2 Experimental set-up . . . 13
  - 2.2.1 PIV equipment and measurement uncertainty . . . 14
- 2.3 Experimental procedure and velocity scaling . . . 16
- 2.4 Results . . . 19
  - 2.4.1 Mean Velocities . . . 19
  - 2.4.2 Turbulent kinetic energy . . . 25
- 2.5 Conclusions . . . 30

References . . . 31

3 Thermally driven heat transfer in the supercritical fluid region 33
- 3.1 Introduction . . . 33
- 3.2 Experimental set-up . . . 35
  - 3.2.1 Rayleigh-Bénard cell . . . 36
- 3.3 Experimental programme . . . 42
- 3.4 Results . . . 44
  - 3.4.1 General findings . . . 44
  - 3.4.2 Nusselt dependency on fluid properties-NOB effects . . . 46
  - 3.4.3 Nusselt dependency on the mean fluid properties . . . 47
- 3.5 Conclusions . . . 54

References . . . 55

4 Design of a high-pressure facility with optical access 59
- 4.1 Introduction . . . 59
- 4.2 Facility description, design criteria and working instructions . . . 60
  - 4.2.1 Pressure and temperature sensors and LabView control 61

4.3 Rayleigh-Bénard cell . . . 64
4.4 Summary . . . 68
References . . . 71

5 PIV measurements of a Rayleigh-Bénard flow in a supercritical fluid 73
5.1 Introduction . . . 73
5.2 Basic information on particle image velocimetry . . . 74
5.3 Optical distortions in supercritical fluids and applicability of PIV . . . 75
5.4 Instrumentation for PIV measurements . . . 76
5.4.1 Particles . . . 76
5.4.2 Laser . . . 79
5.4.3 Camera . . . 79
5.5 Background oriented schlieren . . . 79
5.6 Data process settings and spatial resolution of the measurements . . . 82
5.7 Experimental programme . . . 83
5.8 Results . . . 86
5.8.1 Preliminary investigation with BOS images . . . 86
5.8.2 BOS time averages and magnification factor of the recordings . . . 90
5.8.3 BOS instantaneous measurements . . . 95
5.8.4 PIV uncertainty from correlation statistics . . . 99
5.8.5 Statistical uncertainty . . . 101
5.8.6 PIV measurements . . . 109
5.9 Conclusions . . . 117
References . . . 119

6 Summary and perspectives 123
6.1 Summary . . . 123
6.1.1 Velocity field with strongly temperature-dependent variable properties . . . 123
6.1.2 Heat transfer measurements at supercritical conditions 124
6.1.3 PIV measurements at supercritical conditions . . . 124
6.2 Perspectives . . . 125
References . . . 126

Curriculum Vitæ 127

List of Publications 129

Acknowledgements 131

Summary

Fluids above the critical point are widely used in industry. Chemical, pharmaceutical, food industry and energy production are some examples. In the energy production sector they are mainly used as cooling fluids, because they allow to increase the thermal efficiency of the power plants. However, the fundamentals of their heat transfer behavior are still unknown and current heat transfer models fail to predict it. Supercritical (SC) fluids are characterized by strongly varying fluid properties, which are responsible for their particular heat transfer behavior and make them very difficult to model, simulate and experimentally investigate. In past studies, buoyancy was identified as a key cause for the heat transfer deterioration observed in SC fluids.

The aim of the research described in this thesis is to investigate the possibility of performing non-intrusive local velocity measurements with the optical technique PIV and to acquire global heat transfer measurements, with strongly changing fluid properties at SC conditions. The experiments were performed in a pure buoyancy-driven flow: a Rayleigh-Bénard (RB) flow.

The velocity fields of RB convection with strongly varying properties, beyond the so-called Oberbeck-Boussinesq (OB) approximation, were experimentally studied at atmospheric pressure first. An increase of the time-averaged velocity close to the bottom wall of the cell with respect to the top wall of about 13% was found. This finding confirmed experimentally a top-bottom ”broken symmetry” in the velocity field, which was observed in previous numerical and theoretical studies, but it was never experimentally demonstrated before.

The heat transfer with strongly variable properties at SC conditions for constant Prandtl and Rayleigh numbers, specifically defined outside the validity range of the OB approximation, was experimentally studied. The measurements were performed at the Max Planck Institute of Dynamics and Self-Organization in Göttingen (Germany), with a European EuHIT project. It was observed that the measured Nusselt number defined for non-OB conditions was different from point to point, showing that merely the Rayleigh and Prandtl numbers are not sufficient to determine the heat transfer through the cell. It was also seen that the measured Nusselt number was 16% larger with respect to the one predicted by the Grossmann-Lohse theory (2000) for the same Rayleigh and Prandtl numbers at OB conditions.

A feasibility study of particle image velocimetry (PIV) at SC conditions was done by using the background oriented schlieren technique (BOS). An estimation of the PIV experimental uncertainty at SC conditions was done with the statistical correlation method proposed by Wieneke *et al.*, (2015). PIV was successfully performed at SC conditions. Main difficulties about its applicability were due to blurring and optical distortions in the boundary layer and thermal plumes regions. PIV measurements were performed at three different magnitudes of density difference between

top and bottom of the cell. Two of the three experiments were done at similar Rayleigh and Prandtl numbers, defined for non-OB conditions: one towards the liquid phase and the other one towards the gas phase. The former showed a lower large scale circulation (LSC) velocity than the latter. All cases showed the presence of one asymmetric LSC roll, which is different from a typical RB convection flow at OB conditions.

Improvements in the accuracy of PIV measurements and the acquisition of more heat transfer data at SC conditions, would help the study of the thermal and viscous boundary layer thicknesses and turbulence modifications that are responsible for different heat transfer regimes in SC fluids.

Samenvatting

Vloeistoffen boven het kritische punt worden veel gebruikt in de industrie. De chemische, farmaceutische en levensmiddelenindustrie en de energieproducenten zijn enkele voorbeelden hiervan. In de energiesector worden deze vloeistoffen voornamelijk gebruikt als koelvloeistoffen, omdat ze de thermische efficiëntie van energiecentrales kunnen verhogen. Fundamentele kennis over warmteoverdracht onder superkritische condities is schaars. Bovendien kunnen huidige modellen deze warmteoverdracht nog niet goed voorspellen. Superkritische (SC) vloeistoffen worden namelijk gekenmerkt door sterke variaties in de stofeigenschappen die een atypisch gedrag in warmteoverdracht veroorzaken. Dit gedrag is daarom ook moeilijk te modelleren, te simuleren en te meten. In recente studies is de opwaartse kracht ('buoyancy') geïdentificeerd als één van de belangrijke mechanismes voor warmteoverdracht in SC vloeistoffen.

Het doel van dit proefschrift is om te onderzoeken in welke mate de niet-intrusieve, optische PIV techniek gebruikt kan worden om lokale snelheden te meten onder SC condities. Ook wordt, bij dezelfde condities, de warmteoverdracht bestudeerd. Het gehele onderzoek betreft de zogenaamde Rayleigh-Bénard (RB) convectie in een Rayleigh-Bénard-cel, een stroming die alleen gedreven wordt door natuurlijke convectie.

Allereerst werd het snelheidsveld bij atmosferische druk bestudeerd. De stofeigenschappen van de vloeistof waren hierbij sterk variabel, d.w.z. voorbij de zogenaamde Oberbeck-Boussinesq (OB) benadering. Er werd een toename van de tijdgemiddelde snelheid (+13%) dicht bij de bodemwand van de cel gevonden ten opzichte van de snelheid nabij de bovenwand. Deze bevinding bevestigt een asymmetrie in het snelheidsveld, die eerder werd waargenomen in numerieke en theoretische studies, maar nog nooit experimenteel werd vastgesteld.

Ook werd de warmteoverdracht onder SC condities, en buiten het bereik van de OB-benadering, experimenteel bestudeerd. De metingen werden in het kader van een Europees EuHIT-project uitgevoerd bij het Max Planck Institute of Dynamics and Self-Organization in Göttingen (Duitsland). Waargenomen werd dat het experimenteel bepaalde Nusselt-getal, gedefinieerd voor niet-OB omstandigheden, verschilde van punt tot punt. Deze bevinding toont aan dat de warmteoverdracht onder SC condities niet uitsluitend bepaald wordt door het Rayleigh- en Prandtl-getal. Bovendien werd gevonden dat het gemeten Nusselt-getal 16% groter is dan voorspeld door de theorie van Großmann-Lohse (2000) bij hetzelfde Rayleigh- en Prandtl-getal onder OB condities.

Een haalbaarheidsstudie van de Particle Image Velocimetry techniek (PIV) onder SC condities werd uitgevoerd met behulp van Background Oriented Schlieren (BOS) metingen. De experimentele onzekerheid werd geschat met behulp van de statistische correlatiemethode zoals voorgesteld door Wieneke *et al.*, (2015). Ge-

concludeerd kan worden dat PIV succesvol is uitgevoerd onder SC omstandigheden. De grootste uitdagingen betroffen de optische vervormingen door sterk variërende dichtheden en de aanwezigheid van thermische pluimgebieden. De PIV metingen werden uitgevoerd bij drie verschillende dichtheidsintervallen (bepaald door de temperaturen van boven- en onderkant van de cel). Twee van de drie experimenten werden uitgevoerd bij vergelijkbare Rayleigh- en Prandtl-getallen, gedefinieerd voor niet-OB-condities: één nabij de vloeistoffase en de ander dichtbij de gasfase. De meting nabij de vloeistoffase liet een lagere rotatiesnelheid zien dan die dichtbij de gasfase. Alle metingen lieten een asymmetrische, circulaire stroming in de cel zien, iets wat niet optreedt bij OB condities.

Om de invloed van de verschijnselen in en nabij de thermische en viskeuze grenslaag op de warmteoverdracht nog beter te kunnen begrijpen is het van belang om in de toekomst de nauwkeurigheid van de PIV techniek bij SC condities verder te vergroten en een groter bereik aan gegevens te verwerven met betrekking tot warmteoverdacht.

1 Introduction

1.1. Background and motivation

Supercritical fluids are widely used in industry. Energy production, refrigeration, chemical and pharmaceutical industry and waste disposal are some examples of their main applications [1–5]. Figure 1.1 shows where the supercritical fluid region is located in an example of phase diagram.

In the energy production sector they can be used as cooling fluids for power plants (PPs). They are already in use in coal-fueled power plants, while research is going on to design a new kind of nuclear reactor cooled by supercritical (SC) water [2]. The SC water-cooled reactor (SCWR) is one of the six innovative nuclear energy systems, proposed by the International Forum for the IV generation of nuclear reactors [6]. The International Forum is an international organization set-up in 2001 with the aim of studying the feasibility and performances of a new generation of nuclear reactors. The SCWR reactor design was selected among other reactor designs, mainly because of its higher thermal efficiency (up to 44%, considerably higher than 34-36% of current reactors), its simpler plant system, compact size and lower capital costs [7, 8]. A scheme of the SCWR is represented in Figure 1.2. The coolant is fed directly to the turbines, no recirculation system, steam separators, or dryers are needed. The high temperature of the coolant reached at SC conditions allows both to increase the thermal efficiency of the power plant and to reduce the size of the turbine. Both aspects contribute to lower the capital costs of the reactor with respect to current light water cooled reactors [1–3, 8].

Current open challenges for the development of SCWRs are related to the validation of heat transfer models at SC conditions (to ensure design limits to the fuel temperature), qualification of materials and demonstration of passive safety systems [6].

A particular application of SC fluids to nuclear PPs, which is currently under research, is as heat exchangers for heat recovery systems (sCO2 He-Ro project) [9]. Here supercritical CO_2 is used in a heat removal system as a cooling system, for

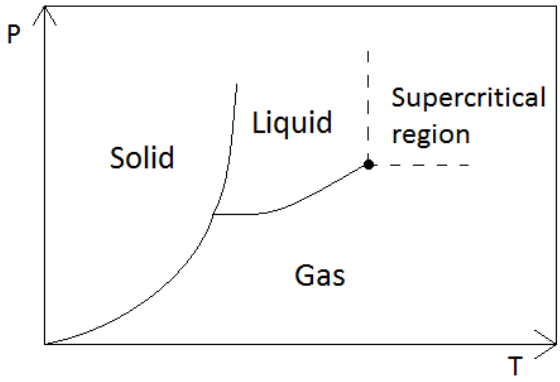


Figure 1.1: Example of pressure-temperature phase diagram that shows where the supercritical fluid region is located.

accident conditions, removing the decay heat of the nuclear fuel. Such a cooling backup system can be applied both in current and in future boiling water reactors and pressurized water reactors.

In the energy production sector, SC fluids can be used also in organic Rankine cycles (ORC), since the critical point of organic fluids can be reached at much lower temperatures and pressures than those of water (e.g. 373-423 K, 3-4 MPa critical temperature and pressure of organic fluids versus 674 K and 22 MPa of water). ORC allows to use low temperature heat sources like the ones from geothermal energy, solar desalination and waste heat recovery. An increase of thermal efficiency of about 8% can be obtained with SC ORC with respect to conventional ORC, due to the higher temperatures reached in the coolant, when the cycle is extended to SC conditions [10–12].

Research is going on also on the use of SC fluids for drilling deep (up to 10 km) geothermal wells. In this case the use of hydrothermal flames (flames ignited in a supercritical water environment [13]) may allow to reduce drilling costs with respect to conventional drilling methods [14].

Applications of SC fluids in chemical and pharmaceutical industry regard the extraction of substances. These processes are based on the strong properties changes of SC fluids within a narrow range of temperatures (see e.g. Figure 1.3). As cited above, SC fluids are used also for waste disposal. For example for the conversion of liquid, mineral-rich organic waste (e.g. wet manure or sewage sludge) into a medium calorific gas as well as valuable minerals, that can be reused in the agricultural sector [5]. SC fluids are used also in food industry for the extraction of chemical compounds, e.g. for decaffeination. They can be used also for extraction of bioactive compounds with good quality and purity of the final product and without toxic residues for the food, pharmaceutical and cosmetic industry [4].

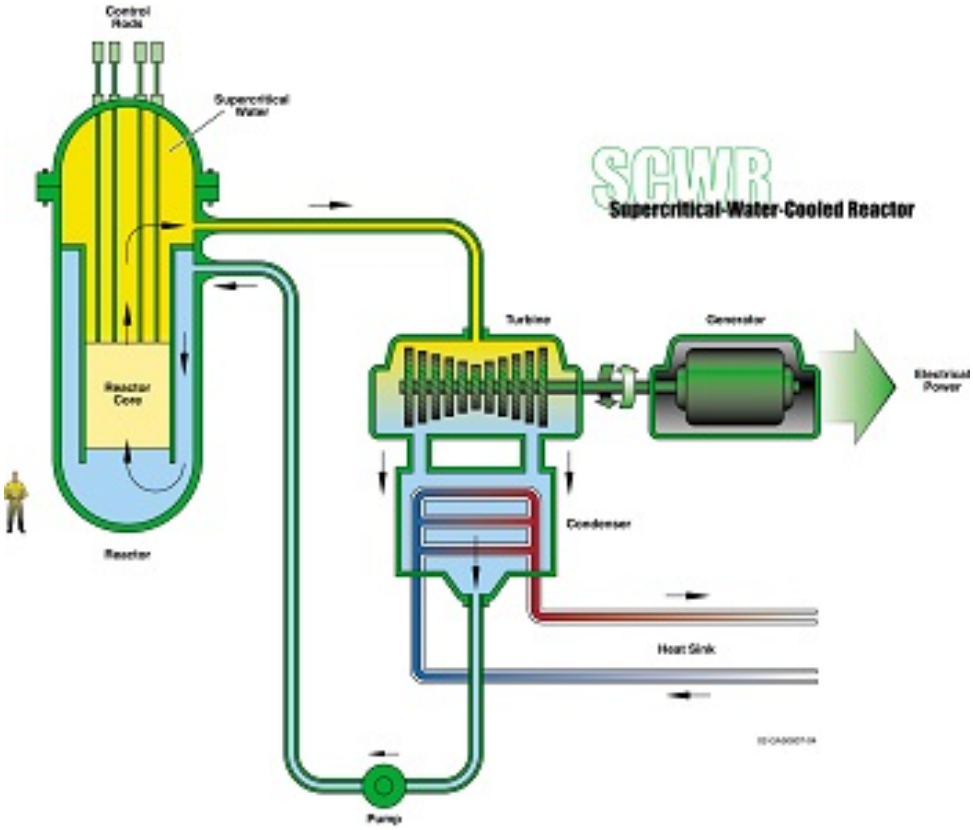


Figure 1.2: Scheme of the supercritical water reactor. Figure taken from the Generation IV International forum website [6]

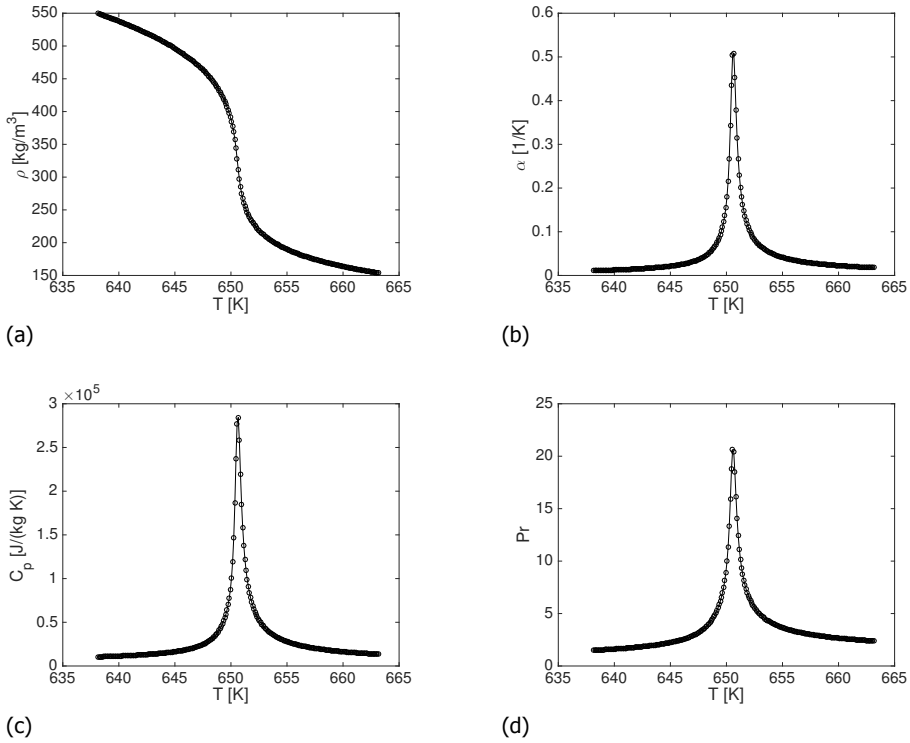


Figure 1.3: Material properties of water as a function of temperature and constant pressure (p= 23 MPa), at supercritical conditions. (a) density (ρ); (b) isobaric thermal expansion coefficient (α); (c) specific heat capacity (c_p); (d) Prandtl number (Pr). Critical point of water: (674 K, 22 MPa). Fluid properties taken from the CoolProp database [15].

One of the main problems with the use of SC fluids for energy production is the validation of current heat transfer models. At SC conditions fluids experience a sharp change of material properties, for example their density changes abruptly within a narrow range of temperatures and their heat capacity shows a peak at the so-called pseudo-critical temperature for a given pressure, as shown in Figure 1.3 for water. As a result, the heat transfer behavior of SC fluids is very different with respect to the one at sub-critical pressure.

Experimental studies in pipe and annular geometries show that both a significant heat transfer enhancement and deterioration may occur at supercritical conditions [16–21]. Several heat transfer correlations have been proposed in the past for SC fluids mainly in pipe flows [17, 19, 22, 23]. However, most of them are based on empirical data, which cannot be generalized to different experimental conditions (e.g. heat or mass flux, geometry or fluid) or are based on strong theoretical assumptions, which are far from reality (e.g. isotropic turbulence and a constant turbulent Prandtl number). A correlation able to describe heat transfer

enhancement and deterioration to SC fluids has not been found yet [20].

Buoyancy, flow acceleration due to thermal expansion and the effect of variable properties were identified as significant contributors to the quality of the heat transfer at SC conditions [20]. In general, flow acceleration due to thermal expansion is caused by axial density gradients, while the buoyancy effect is mainly caused by radial density gradients. Figure 1.3 (b) shows the temperature dependency of the isobaric thermal expansion coefficient of water at SC pressure. Kurganov *et al.* [16] showed how velocity profiles and shear stresses are drastically modified in case of heat transfer deterioration, which happens for upwards flows. At these conditions, the velocity profile on a cross-section of the pipe assumes a typical "M" shape and the shear stress becomes locally negative. Jackson *et al.* [18] found that the effect of buoyancy plays a positive role in case of downward flows and a negative role in upward flows, where it may cause heat transfer deterioration. This is particularly important for mixed convection, which can be found for example in nuclear reactor cores. Jackson proposed in his review paper [19] a model where both acceleration due to thermal expansion and buoyancy are taken into account as responsible for heat transfer deterioration. They both cause a sharp shear stress reduction and, thus a reduction in the turbulent production near the wall. Jackson called this phenomenon re-laminarization and explained it on the base of a balance between buoyancy and shear stress forces.

While the qualitative effect of buoyancy in heat transfer effectiveness at SC conditions seems clear, the heat transfer has remained unpredictable. The mechanism of buoyancy driven flows with strongly variable properties at supercritical conditions is still unknown. Past literature studies considered the effect of buoyancy in mixed and forced convection systems [17, 18, 20, 24]. The work presented in this thesis separately analyses the effect of buoyancy, in a natural convection system.

1.1.1. Experiments in fluids with strongly variable fluid properties

Experiments in SC fluids are challenging and very expensive, mainly because of the high pressures and temperatures that characterize the critical point (CP) of many fluids of practical use, e.g. water (CP: 674 K, 22 MPa) and CO_2 (CP: 304 K, 7,38 MPa). A vast amount of published experimental studies has been performed in SC fluids in pipe and annular geometries. The measured quantities in these studies were wall and bulk temperatures, heat fluxes and mass flow rates [17, 19, 25]. Local velocity measurements at SC conditions were done in the above commented study by Kurganov *et al.* [16]. This study showed velocity profiles in a pipe measured by Pitot tubes inserted in the flow. Whole velocity fields, both in time and locality, at SC conditions have never been reported in literature.

The PIV technique is a non-intrusive optical technique that allows the visualization of a whole velocity field at each instant of time [26]. Another common non-intrusive technique to measure velocities is laser-Doppler velocimetry (LDV). The latter technique allows to measure the velocity of one point at each instant of

time with high time and spatial accuracy [27]. Both techniques need tracer particles in the flow and both are challenged by density gradients within the fluid, rousing refraction of the laser beams for LDV or of the laser light sheet and refracted light from the particles for PIV.

PIV measurements have never been done at supercritical conditions and only two previous studies with the optical technique LDV near or above the critical point have been reported in literature. In one study, performed by Ashkenazi and Steinberg [28], the temperature difference between the two horizontal plates of their thermal convection system was mantained of the order of 10 mK, to keep the fluid within Oberbeck-Boussinesq conditions [29, 30]. With this temperature difference the density changes that may disturb the optical measurements can be neglected. In the other study, performed by Licht *et al.* [21], the measurements were done in a square annulus, with forced and mixed convection. In the latter case a correction in the experimental results was made with a beam tracing program (made with the CFD software FLUENT) to take into account radial changes in the fluid properties and in particular the index of refraction. They verified experimentally that for mixed convection the heat transfer cannot be predicted by existing theories [18, 19]. They identified the buoyancy effect as the responsible for turbulence reduction close to the wall in conditions of heat transfer deterioration. Their measured mean and turbulent velocities provide a database for the development of theoretical models of heat transfer to supercritical water and for the validation of CFD models, besides being the first experience of LDV measurements in SC fluids with strong optical distortions. The combination of experiments with a numerical study to predict laser beams deviations can be used as a reference for future LDV measurements in SC fluids.

Optical measurements in fluids with refractive index fields were done in the past to study a different physical problem, being the one of compressible flows. Blur and errors in the velocity measurements caused by strong refractive index variations, were studied by Elsinga *et al.* [31]. In their study, a method was developed to quantify and correct for PIV errors due to refractive index changes in two-dimensional compressible flows with stationary and smoothly varying density distribution. They showed, with the help of PIV recordings, BOS (background-oriented schlieren) measurements and numerical simulations that the second derivative of the refractive index is the mayor source of velocity errors in PIV. PIV studies in fluids with strong localized refractive index changes were performed in compressible flows by Murphy *et al.* [32] and by Elsinga et al. [33]. Murphy et al. [32] developed a high speed PIV system to study blast waves. Elsinga *et al.* [33] performed PTV (particle tracking velocimetry) and PIV measurements together with light-ray tracing predictions and found that optical errors in the velocity measurements of shock waves depend strongly on the angle between the viewing direction and the plane of the shock.

1.2. Aim of this research

The aim of the research described in this thesis is to investigate the possibility of performing non-intrusive local velocity measurements on a whole cross-

section of the domain, with the optical technique PIV and independent heat transfer measurements. The experiments are performed in a pure buoyancy-driven flow at SC conditions, with the goal of providing instantaneous and time-averaged velocity fields with strongly changing fluid properties and acquiring heat transfer data. These measurements are meant to improve the understanding of how strongly variable fluid properties influence the flow field and heat transfer in thermal convection driven SC fluids.

1.2.1. Experimental campaign

To this purpose a Rayleigh-Bénard system is studied, because of its experimental accessibility. In this case the fluid motion is driven by thermal convection and, thus, no complex loop system is needed. The RB set-up chosen is cubical, with optical access from the lateral walls.

Measurements of velocity fields at SC conditions are acquired at different mean temperatures and pressures. The experimental conditions are chosen such that the effect of properties variations between top and bottom of the RB-cell can be studied. Heat transfer measurements at several mean pressures and temperatures, closer or farther away from the critical point, are also performed to study how the fluid property variability influences the global heat transfer. The data points are chosen at constant non dimensional numbers and for different top-bottom temperature dependencies of the fluid properties. It is important to check the sensitivity of the heat transfer rate through the cell to the magnitude and sign of the top-bottom properties changes.

1.3. Thesis outline

In Chapter 2 the mean velocity field of RB-convection with strongly temperature-dependent fluid properties is compared with a case with weak temperature dependent properties, both at atmospheric pressure. The velocity fields in the two cases are experimentally obtained with PIV measurements.

Chapter 3 presents a heat transfer study at SC conditions. This study was done at the Max Planck Institute of Dynamics and Self Organization in Göttingen, with an EuHIT European project. The heat transfer through the cell is shown at several mean pressures and temperatures, closer or farther from the critical point. The data are acquired while keeping constant the values of the non dimensional numbers that govern the flow under Oberbeck-Boussinesq conditions [29, 30].

Chapter 4 is a description of the experimental facility that was designed, built and used for the PIV measurements at SC conditions.

Chapter 5 shows both a feasibility study of PIV at SC conditions and PIV velocity fields at SC conditions with estimation of their uncertainties. Mean velocity fields are presented at three different mean pressures and temperatures in the SC region.

Chapter 6 contains the conclusion of this experimental investigation on heat transfer and flow structures in Rayleigh-Bénard convection at SC conditions.

1

References

[1] I. Pioro and P. Kirillov, *Current status of electricity generation in the world*, edited by A. Méndez-Vilas, Vol. Materials and processes for energy: communicating current research and technological developments (A. Méndez-Vilas, 2013).

[2] I. L. Pioro and B. Romney, *Handbook of Generation IV Nuclear Reactors*, edited by I. L. Pioro, Woodhead Publishing Series in Energy (Woodhead Publishing, 2016).

[3] I. Pioro, *Nuclear Power as a Basis for Future Electricity Production in the World: Generation III and IV Reactors* (2012).

[4] C. G. Pereira and M. A. A. Meireles, *Supercritical Fluid Extraction of Bioactive Compounds: Fundamentals, Applications and Economic Perspectives,* Food and Bioprocess Technology **3** (2010).

[5] O. Yakaboylu, *Supercritical water gasification of wet biomass: modeling and experimenys*, Ph.D. thesis, Delft University of Technology (2016).

[6] *Generation IV Internationa Forum,* (2017).

[7] J. Buongiorno and P. E. MacDonald, *Supercritical Water Reactor (SCWR) Progress Report for the FY-03 Generation-IV R&D Activities for the Development of the SCWR in the U.S.*, Tech. Rep. (INEEL, 2003).

[8] Y. Oka and S.-I. Koshizuka, *Concept and design of a supercritical-pressure, direct-cycle light water reactor,* Nuclear Technology **103** (1993).

[9] sCO2-HeRo Project, (2017).

[10] E. G. Feher, *The supercritical thermodynamic power cycle,* (1968).

[11] A. Schuster, S. Karellas, and R. Aumann, *Efficiency optimization potential in supercritical Organic Rankine Cycles,* Energy **35**, 1033 (2010).

[12] S. Karellas and A. Schuster, *Supercritical Fluid Parameters in Organic Rankine Cycle Applications,* International Journal of Thermodynamics **11**, 101 (2008).

[13] v. P. R. Rohr, K. Príkopský, and T. Rothenfluh, *Flames in supercritical water and their applications,* STROJNÍCKY ČASOPIS **59** (2008).

[14] M. J. Schuler, *Fundamental Investigations of Supercritical Water Flows for Hydrothermal Spallation Drilling*, Ph.D. thesis, ETH Zürich (2014).

[15] I. H. Bell, J. Wronski, S. Quoilin, and V. Lemort, *Pure and pseudo-pure fluid thermophysical property evaluation and the open-source thermophysical property library coolprop,* Industrial & Engineering Chemistry Research **53**, 2498 (2014).

[16] V. A. Kurganov and A. G. Kaptil'ny, *Velocity and enthalpy fields and eddy diffusivities in a heated supercritical fluid flow,* Experimental Thermal and Fluid Science **5**, 465 (1992).

[17] D. Huang, Z. Wub, B. Sunden, and W. Li, *A brief review on convection heat transfer of fluids at supercritical pressures in tubes and the recent progress,* Applied Energy **162**, 494 (2016).

[18] J. Jackson, *Studies of buoyancy-influenced turbulent flow and heat transfer in in vertical passages,* in *Heat Transfer Conference Sydney* (2006).

[19] J. Jackson, *Fluid flow and convective heat transfer to fluids at supercritical pressure,* Nuclear Engineering and Design **264**, 24 (2013).

[20] J. Y. Yoo, *The turbulent flows of supercritical fluids with heat transfer,* Annual Review of Fluid Mechanics **45**, 495 (2013).

[21] J. Licht, M. Anderson, and M. Corradini, *Characteristics in supercritical pressure water,* Journal of Heat Transfer **131**, 072502(1 (2009).

[22] S. Gupta, E. Saltanov, S. J. Mokry, I. Pioro, L. Trevanib, and D. McGillivray, *Developing empirical heat-transfer correlations for supercritical co2 flowing in vertical bare tubes,* Nuclear Engineering and Design **261**, 116 (2013).

[23] M. M. Rahman, J. Dongxu, M. S. Beni, H. C. Hei, W. He, and J. Zhao, *Supercritical water heat transfer for nuclear reactor applications: A review,* Annals of Nuclear Energy **97**, 53 (2016).

[24] S. He, W. Kim, and J. Bae, *Assessment of performance of turbulence models in predicting supercritical pressure heat transfer in a vertical tube,* International Journal of Heat and Mass Transfer **51**, 4659 (2008).

[25] R. B. D. Igor L. Pioro, Hussam F. Khartabil, *Heat transfer to supercritical fluids flowing in channels - empirical correlations (survey)channels-empirical correlations (survey),* Nuclear Engineering and Design **230**, 69 (2004).

[26] J. Westerweel, G. E. Elsinga, and R. J. Adrian, *Particle image velocimetry for complex and turbulent flows,* Annual Review of Fluid Mechanics **45**, 409 (2013).

[27] C. Tropea, A. Yarin, and J. F. Foss, *Springer Handbook of Experimental Fluid Mechanics*, edited by C. Tropea, A. Yarin, and J. F. Foss (Springer-Verlag Berlin Heidelberg, 2007).

[28] S. Ashkenazi and V. Steinberg, *High Rayleigh Number Turbulent Convection in a Gas near the Gas-Liquid Critical Point,* Physical Review Letters **83** (1999).

[29] A. Oberbeck, *Ueber die Wärmeleitung der Flüssigkeiten bei Berücksichtigung der Strömungen infolge von Temperaturdifferenzen,* Annalen der Physiks **243**, 271 (1879).

[30] J. Boussinesq, *Théorie analytique de la chaleur*, Vol. 2 (Gauthier-Villars (Paris), 1903).

[31] G. E. Elsinga, B. W. van Oudheusden, and F. Scarano, *Evaluation of aero-optical distortion effects in PIV,* Experiments in Fluids **39**, 246 (2005).

[32] M. J. Murphy and R. J. Adrian, *PIV space-time resolution of flow behind blast waves,* Experiments in Fluids **49** (2010).

[33] G. E. Elsinga and G. C. Orlicz, *Particle imaging through planar shock waves and associated velocimetry errors,* Experiments in Fluids **56** (2015).

2

Non-Oberbeck-Boussinesq effects in Rayleigh-Bénard convection at atmospheric pressure

2.1. Introduction

In the Oberbeck-Boussinesq approximation [2, 3] (OB), the fluid properties are assumed to be constant in all the terms of the Navier-Stokes equations, except in the buoyancy term. The OB approximation can be used in many cases to simplify complex problems without a significant loss of accuracy, but there are also many physical phenomena that cannot be understood without considering the temperature dependency of the fluid properties (see e.g. [4]). In the present study Rayleigh-Bénard (RB) convection was studied at conditions beyond the OB approximation, in which the volumetric thermal expansion coefficient, the kinematic viscosity and the Prandtl number vary significantly with temperature over the flow domain.

There are several earlier studies in literature that focus on RB convection at non-Oberbeck-Boussinesq (NOB) conditions. In Ahlers *et al.* 2006 [5] an experimental and theoretical study on the effects of NOB conditions on the Nusselt and Reynolds number is presented, with heat flux and temperature data. Their Reynolds number measurements are based on thermal plumes transient times calculated from temperature auto- and cross-correlation functions [5]. The working fluid in their study is water at atmospheric pressure, which shows significant changes of the kinematic viscosity and the volumetric thermal expansion coefficient in the range of temperatures considered. They observed significant deviations from the OB approximation

Parts of this chapter have been published in Physical Review E **95**, 053113 (2017) [1].

in the ratio between bottom and top thermal boundary layer thicknesses, up to 20% for the studied conditions. However, despite this reduction in the thickness of the bottom boundary layer with respect to the top one, they did not find significant changes of Nusselt and Reynolds numbers due to the temperature dependency of the fluid properties, up to 2%. For similar conditions, Sugiyama *et al.*, 2009 [6] performed a 2D direct numerical simulation (DNS) study with the purpose of analyzing the flow organization of Rayleigh-Bénard convection with variable properties. In this study, no significant differences between the flow structure at non-Oberbeck-Boussinesq (NOB) and at OB conditions were observed, except for the secondary flow, where an apparent asymmetry emerges between the two small rolls at two opposite corners of the cell. NOB effects in the velocity fields of RB convection were also studied in 3D numerical simulations in glycerol and water by Horn *et al.* [7, 8]. In these studies differences due to NOB effects were observed in the mean velocity profiles as bottom-top asymmetries of the horizontal velocity component and in the thickness of the bottom kinetic boundary layer. More specifically, they found an increase of the horizontal component of the velocity and a decrease of the kinetic boundary layer close to the bottom wall of the cell. Both aspects were attributed to non-Boussinesq effects due to the temperature dependency of the kinematic viscosity. NOB conditions in glycerol were experimentally studied with velocity measurements in the thermal sublayers through temperature fluctuation signals by Zhang *et al.* 1998 [9]. They observed that the second spatial derivative of the measured velocity profile has a different sign in the thermal sublayer close to the bottom wall of the cell (positive sign) with respect to the top thermal sublayer (negative sign). The change in the second spatial derivative of the velocity in the thermal sublayers was explained as a response of the velocity to the kinematic viscosity changes (due to a strong temperature dependency of the kinematic viscosity) and the maintenance of a constant viscous stress in a steady thermal layer. There are no experimental studies in the literature of the whole velocity field of RB convection under NOB conditions.

The objective of the research described in this chapter is to experimentally determine the effects of NOB conditions on the whole velocity field in a vertical cross section of RB convection at atmospheric pressure. This is an experimental verification on a 3D domain and with accurate direct velocity measurements of the several numerical and theoretical [5–8] studies on NOB effects in the velocity fields of RB convection. This study is preliminary to the one presented in Chapter 5, where PIV velocity fields of RB convection at supercritical conditions are shown.

In this study at atmospheric pressure, the characteristics of measured velocity fields under NOB conditions in a 77 mm high cubical RB convection cell were compared with the velocity fields of a control experiment done in the same set-up at OB conditions. NOB conditions were created with a temperature difference of 40 K imposed on the cell while it was filled with water. The Rayleigh and Prandtl numbers are the two non-dimensional parameters that govern the flow for a given geometry of the domain. They are obtained after non-dimensionalization of the Navier-Stokes

equations, under OB conditions. The Rayleigh number (Ra) is defined as:

$$Ra \equiv \frac{\alpha g \Delta T H^3}{\nu \kappa}, \tag{2.1}$$

where α is the isobaric thermal expansion coefficient of the fluid, g the gravitational acceleration, ΔT the difference of temperature between the hot bottom plate and the cold top plate of the cell, H the distance between the two horizontal plates, ν the kinematic viscosity of the fluid, and κ the thermal diffusivity of the fluid. The Prandtl number (Pr) is defined as the ratio between kinematic viscosity and thermal diffusivity:

$$Pr \equiv \frac{\nu}{\kappa}. \tag{2.2}$$

Since under NOB conditions the fluid properties vary throughout the flow domain, the Ra and Pr numbers in this case were defined as:

$$Ra_{NOB} \equiv \frac{\alpha_m g \Delta T H^3}{\nu_m \kappa_m},, \tag{2.3}$$

$$Pr_{NOB} \equiv \frac{\nu_m}{\kappa_m}. \tag{2.4}$$

where all the fluid properties are taken at the average temperature between the bottom and the top wall temperature of the cell, T_m, reported in Table 2.2. This is indicated with a subscript m in the symbol of the fluid property.

The imposed ΔT of 40 K for the NOB case, resulted in $Ra_{NOB} = 6.9 \times 10^8$ and $Pr_{NOB} = 4.3$. The reference case for OB conditions considered a 9.6 K temperature difference between the bottom and top plate of the cell, resulting in $Ra = 6.7 \times 10^8$ and a $Pr = 7.2$, with methanol as working fluid. Methanol was chosen to maintain similar Rayleigh and Prandtl numbers in the OB case with respect to the NOB one, while using the same set-up for both experiments. Particle image velocimetry was then applied to determine the mean velocities and the RMS values of the velocity fluctuations in a vertical cross-section of the RB convection cell for both the OB and the NOB case. From the experimental velocity fields a NOB effect emerges as top-bottom asymmetries in the mean velocity of the flow.

2.2. Experimental set-up

The Rayleigh-Bénard cell used for the experiments is a cube of 77 mm inner length (H), see Figure 2.1. It has four 1.2 mm thick vertical glass walls that allow for optical access and two horizontal copper plates. The bottom copper wall is electrically heated by an heating strip with adjustable power. The top copper wall is water cooled. The temperature of the cooling water can be regulated to maintain the temperature of the top plate at the desired value. Four thermistors are located in each one of the horizontal walls to monitor the uniformity of the temperature in the plates. The thermistors are made of epoxy coated NTC of type C100. The cell is slightly tilted, less than 3 degrees on the horizontal plane (XZ plane) in diagonal direction, in order to fix the orientation of the large-scale circulation of the flow. Further details about the apparatus can be found in [10].

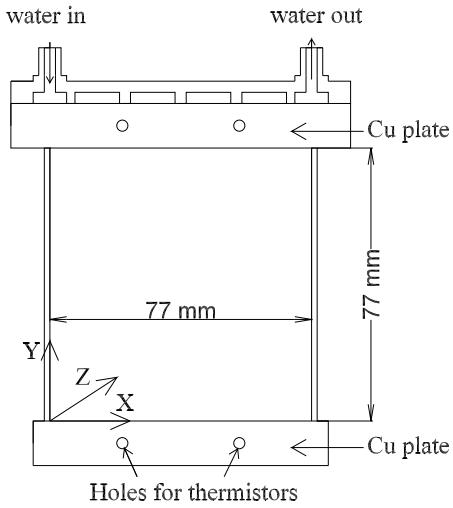


Figure 2.1: Sketch of a vertical section of the Rayleigh-Bénard cell.

2.2.1. PIV equipment and measurement uncertainty

Planar PIV measurements were performed in a vertical cross section of the convection cell, at half the depth of the domain ($Z/H = 0.5$). A diode laser (Pegasus) with a power of 400 mW and a wave length of 520 nm was used to create a light sheet for the illumination of seeding particles in the measurement section. Two kinds of particles were chosen for the experiments with water and methanol. In water, fluorescent particles were used with the purpose of avoiding the effect of reflections off the glass walls of the laser light in the images and improving the quality of the measurements close to the wall. The fluorescent particles (Fluostar) have an average diameter of 13 μm and a density of 1.1 g/cm^3. The fluorescent dye is Rhodamine B, which is excited by a wave length of 550 nm and emits at 580 nm. A long pass optical filter was placed in front of the camera to block the laser light and visualize only the fluorescent emission of the particles. For the experiments with methanol it was not possible to use fluorescent seeding for reasons of chemical incompatibility of the particles with alcohols. Silver coated particles (Dantec) were used in methanol instead. These particles have an average diameter of 10 μm and a density of 1.4 g/cm^3. A PIV camera (LaVision Imager Intense) with a resolution of 1088×1040 pixels was used for the recordings. In the experiments done with silver coated particles a background image subtraction was applied to the camera recordings, with the aim of reducing the effect of reflections of the laser light in the images off the glass walls.

The camera was equipped with an objective with a focal length of 60 mm and an aperture stop $f_\# = 8$. The magnification factor of the recordings is M = 0.055. Velocities are measured with a second pass interrogation window of 16×16 pixels and an overlap of 50%, which corresponds to a resolution in space of 0.65 mm (8 pixels or 0.008 times the height of the cell). The interrogation window is

the region where the PIV cross-correlation is computed. In this case the PIV algorithm operated in two consecutive passes, one with interrogation window size of 32×32 pixels and a second one of 16×16. The latter determines the spatial resolution of the measurements. The laser was triggered with a pulse separation time of 0.030 s, corresponding to a particle image displacement between frames of about 6 pixels in the highest velocity regions of the NOB experiment. For each experiment 10800 frames were acquired during one hour long measurements, which corresponds to more than 100 turnover times of the LSC motion. To ensure steady state of the flow, the measurements were done after running the set-up at constant conditions for about four hours. To double check the steady state of the flow, the experiments were repeated twice on different days with results that confirm the previous ones. They are shown in Figures 2.4, 2.5, 2.7, 2.8, and 2.9. In Figures 2.4, 2.5, 2.8, and 2.9, two versions of each case are plotted as one-line profiles. The repeated experiments are called Non-Oberbeck-Boussinesq 2^{nd} and Oberbeck-Boussinesq 2^{nd}. Figure 2.7 shows the contour plots of only the second experiment of each case (Non-Oberbeck-Boussinesq 2^{nd} and Oberbeck-Boussinesq 2^{nd}), while results of the first experiments are in Figure 2.6. Small differences between the first experiments and the repeated ones can be attributed to statistical uncertainty of the velocity measurements.

For each component of the velocity field, the mean velocity magnitude and the RMS of the fluctuating velocity component, defined by the Reynolds decomposition $u_i = \overline{u_i} + u_i'$, were computed from PIV measurements as described in formulas (2.5),(2.6) and(2.7):

$$\overline{u_i} = \frac{\sum_{j=1}^{N} u_{i,j}}{N}, \tag{2.5}$$

$$\overline{u_i' u_i'} = \overline{u_i^2} - \overline{u_i}^2, \tag{2.6}$$

$$\mathrm{RMS}(u_i') = \sqrt{\overline{u_i' u_i'}}, \tag{2.7}$$

where $i = \mathrm{X,Y}$ and N is the number of frames. The turbulent kinetic energy (k) is defined on the base of the RMS of the velocity fluctuations as:

$$k = \frac{1}{2} \sum_{i=\mathrm{X,Y}} \overline{u_i' u_i'}. \tag{2.8}$$

The statistical uncertainty of the mean velocity values of the NOB and the OB case was respectively estimated as 3% and 7% of their measured values and the statistical uncertainty of the RMS of the fluctuating velocity values was estimated as 11% and 13 % of their measured values, respectively. They were computed from (2.9) and (2.10), where n is the number of independent samples, estimated as in (2.11). Since equations (2.9) and (2.10) refer to a single measurement point, the values of the relative uncertainties of the mean and RMS velocity values are taken in the

Table 2.1: Upper bounds for the statistical relative uncertainties of the measured quantities.

Quantity	T	U_X, U_Y	RMS (u)
Relative uncertainty	1 %	2 %	7 %

point where they exhibit their highest value and rounded to the highest integer.

$$\text{Rel.Unc.}(u_i) = \frac{\sqrt{\overline{u_i' u_i'}}}{\overline{u_i}\sqrt{n}}, \tag{2.9}$$

$$\text{Rel.Unc.}\left(\sqrt{\overline{u_i' u_i'}}\right) = \sqrt{\frac{2}{n}}, \tag{2.10}$$

$$n = \frac{N}{\frac{4\times H}{0.9\times \overline{u}_{max}} f}, \tag{2.11}$$

where the frequency f is 3 frames/s. In table 2.1 values for the upper bounds of the relative uncertainties of the measured quantities are reported.

2.3. Experimental procedure and velocity scaling

At NOB conditions the temperature difference between the bottom and the top plate of the cell leads to fluid property differences that are beyond the OB approximation, while in the OB case the temperature difference applied to the two horizontal plates of the cell results in smaller changes of fluid properties. The OB experiment was done in the same experimental set-up of the NOB experiment to show that the NOB effects seen in the NOB case are due to the strong temperature dependency of the fluid properties and not to the experimental apparatus used for the measurements.

The two experiments were done at similar Rayleigh and Prandtl numbers. In Tables 2.2 and 2.3 respectively, the experimental conditions of the two cases are given, together with an example of the changes of the values of two fluid properties and of the Prandtl number between the bottom and the top plate of the cell. The two properties considered are the isobaric thermal expansion coefficient (α) and the kinematic viscosity (ν), because these are the properties of water that show the largest change at atmospheric pressure. In the last column also the change on Prandtl number throughout the cell due to its temperature dependency is given for both fluids. To maintain the same Rayleigh number in the same set-up, both for the OB and the NOB case, the experiment at OB conditions was done with methanol, while the working fluid in the NOB case was water.

To make the flow fields dimensionless, taking into account the influence of the variation in Pr number between the two experiments ($Pr_{NOB} = 4.33$ in the NOB case and $Pr_{NOB} = 7.24$ in the OB one), the velocity values were scaled by a characteristic large-scale circulation (LSC) velocity of the flow. Currently in literature there are two

Table 2.2: Experimental conditions with non-dimensional numbers. All the properties in the non-dimensional numbers are taken at the average temperature between the bottom and top wall temperatures of the cell (indicated as T_m). The values of the properties of both water and methanol were taken from REFPROP version 9.1 [11].

Exp. conditions	Fluid	Ra_{NOB}	Pr_{NOB}	$T_m[°C]$	ΔT [°C]
NOB	Water	6.9×10^8	4.33	40	40
OB	Methanol	6.7×10^8	7.24	20	9.6

Table 2.3: Relative changes of α, ν and Pr from the bottom to the top of the cell. The values of the properties of both water and methanol were taken from REFPROP version 9.1 [11].

Exp. conditions	$\frac{\Delta\alpha}{\alpha_{top}}$	$\frac{\Delta\nu}{\nu_{top}}$	$\frac{\Delta Pr}{Pr_{top}}$
NOB	153%	−52%	−57%
OB	1.5%	−13%	−11%

possible ways to determine the LSC velocity of the flow as a function of the Rayleigh and Prandtl number with the OB approximation: the Grossmann-Lohse (GL) theory [12–14] and the scaling method proposed by Pandey *et al.* 2016 [15, 16].

The GL theory, summarized by Ahlers *et al.* [17] allows for the prediction of a typical Reynolds number and Nusselt number as a function of the Rayleigh number and Prandtl number, for cells of aspect-ratio-one at Oberbeck-Boussinesq conditions. The LSC velocity used for the scaling is calculated from the Reynolds number predicted by the GL theory as:

$$U_{LSC\ (GL)} = Re\frac{\nu_m}{H}. \tag{2.12}$$

The equations of the GL theory that were used for the velocity scaling are:

$$(Nu-1)\,RaPr^{-2} = c_{1(GL)}\frac{Re^2}{g\left(\sqrt{Re_L/Re}\right)} + c_{2(GL)}Re^3, \tag{2.13}$$

$$Nu-1 = c_{3(GL)}Re^{1/2}Pr^{1/2}\left\{f\left[\frac{2aNu}{\sqrt{Re_L}}g\left(\sqrt{\frac{Re_L}{Re}}\right)\right]\right\}+c_{4(GL)}PrRef\left[\frac{2aNu}{\sqrt{Re_c}}g\left(\sqrt{\frac{Re_L}{Re}}\right)\right]. \tag{2.14}$$

Table 2.4: Measured large-scale circulation velocity (LSC) ($U_{LSCexp.}$) and LSC estimated with the GL theory ($U_{LSC(GL)}$) and the model from Pandey *et al.* 2016 ($U_{LSC(P)}$). The measured LSC velocity represents the maximum of the time-average vertical velocity.

Exp. conditions	$U_{LSCexp.}[m/s]$	$U_{LSC(GL)}[m/s]$	$U_{LSC(P)}[m/s]$
NOB	16.4×10^{-3}	9.5×10^{-3}	15.3×10^{-3}
OB	12×10^{-3}	7.5×10^{-3}	12.9×10^{-3}

The following constants and formulas were applied [18]:

$$c_{1(GL)} = 8.05,\ c_{2(GL)} = 1.38,\ c_{3(GL)} = 0.487,\ c_{4(GL)} = 0.0252,\ a = 0.922,\ Re_L = (2a)^2, \tag{2.15}$$

$$f(x_\theta) = (1 + x_\theta^4)^{-1/4},\ x_\theta = 2a\frac{Nu}{\sqrt{Re}}, \tag{2.16}$$

$$g(x_L) = x_L(1 + x_L^4)^{-1/4},\ x_L = \sqrt{\frac{Re_L}{Re}}. \tag{2.17}$$

Both Ra and Pr are known (from the experiments). Hence by solving equations (2.13) and (2.14) the Re number can be computed and from equation (2.12) the velocity scale $U_{LSC\ (GL)}$ can be determined.

The method proposed by Pandey *et al.*, 2016 [15, 16] is a different way with respect to the GL theory to calculate the LSC velocity of the flow on the base of the Rayleigh and Prandtl numbers, under OB conditions. It is valid for arbitrary Rayleigh and Prandtl numbers. It is based on the comparison among the relative strength of the non-linear pressure, buoyancy and viscous terms of the momentum equation of RB convection. In the turbulent regime, which is characterized by $Ra \gg 10^6 Pr$, the LSC velocity can be computed with the formulas (2.18),(2.19),(2.20),(2.21) and (2.22) [16]:

$$U_{LSC(P)} = Pe\frac{H}{\kappa_m} \tag{2.18}$$

where κ is the thermal diffusivity of the fluid, taken at the average temperature between the bottom and top wall temperatures of the cell, T_m, and Pe is the Peclet number computed from (2.19):

$$Pe = \sqrt{\frac{c_{3(P)}}{|c_{1(P)} - c_{2(P)}|}} \tag{2.19}$$

$$c_{1(P)} = 1.5\ Ra^{0.10} Pr^{-0.06} \tag{2.20}$$

$$c_{2(P)} = 1.6\ Ra^{0.09} Pr^{-0.08} \tag{2.21}$$

$$c_{3(P)} = 0.75\ Ra^{-0.15} Pr^{-0.05} \tag{2.22}$$

As summarized in the paper about scaling of large-scale quantities in RB convection by Pandey *et al.*, 2016 [15], there are several possible ways to calculate the U_{LSC} of the flow. U_{LSC} can be quantified for example as the maximum absolute value of the horizontal or of the vertical mean velocity component, or on the base of their RMSs. In the present study U_{LSC} was computed from the experimental data as the absolute value of the maximum of the mean vertical velocity component, because it is less affected by NOB effects with respect to the horizontal velocity component or to the velocity RMS values. The LSC velocity computed from the

experimental data as the peak of the time average vertical velocity profile together with the LSC velocities estimated from the GL theory and from the model of Pandey *et al.*, 2016 are all reported in Table 2.4.

From the comparison among the experimental U_{LSC} and the two LSC scaling velocities that were theoretically predicted on the basis of the Rayleigh and Prandtl numbers of the experiments (see Table 2.4), several interesting observations can be made.

One is that the model proposed by Pandey *et al.*[15, 16] matches the experimental values very well for both the OB and the NOB case. The relative difference between the predicted velocity and the experimental one is indeed within 7.5% for both cases. The relative difference of the U_{LSC} predicted with the GL theory with respect to the experimental values is instead quite large for both the NOB and the OB case, 73% and 60% respectively. From Table 2.4 it can also be seen that while the GL theory underestimates both the NOB and the OB case, the Pandey model underestimated the NB case and overestimates the OB case. Another interesting observation that can be made from Table 2.4 is that the ratio between the measured U_{LSC} for the NOB case and the OB case ($16.4/12 = 1.37$) is matched better by the predictions of the GL theory ($9.5/7.5 = 1.27$) than by the Pandey model ($15.3/12.9 = 1.19$). The data presented in this chapter were scaled both by $U_{LSC(GL)}$ and by $U_{LSC(P)}$, in order to show that the choice of one scaling velocity with respect to the other one does not make any difference with regard to the NOB effects found. The NOB effects indeed were presented as top-bottom asymmetries within one experiment. The Boussinesq experiment was used as a reference case, done in the same set-up, to show that the NOB effects seen in the NOB case are independent of the experimental apparatus.

2.4. Results

2.4.1. Mean Velocities

The mean velocity field in a vertical cross section at half-depth of the cell ($Z/H = 0.5$) is shown in Figure 2.2. The NOB case is presented in panel (a), while the OB case is presented in panel (b). It can be seen that the velocity fields show a similar shape in both cases: a large roll in the center (the large-scale circulation of the flow) and two small counter-rotating rolls in the upper-left corner and in the bottom-right corner. This agrees with what was reported by Xia *et al.* 2003 [19] at a similar Rayleigh number under OB conditions. In particular the presence of the two corner rolls in the velocity field was found in previous literature as an expression of a characteristic velocity mode of the studied Rayleigh and Prandtl numbers. This mode was identified as responsible for flow reversals [20–22]. It is also interesting to observe that corner rolls were found also in 2D numerical simulations done at similar Rayleigh and Prandtl numbers of our NOB experiment, at NOB conditions in water by Sugiyama *et al.*, JFM 2009. By looking at the corner rolls of Sugiyama *et al.*, 2009, it can be seen that they are characterized by a spatial extension of about 0.4 X/H, while the spatial extension of the rolls in our 3D experiment is about 0.15

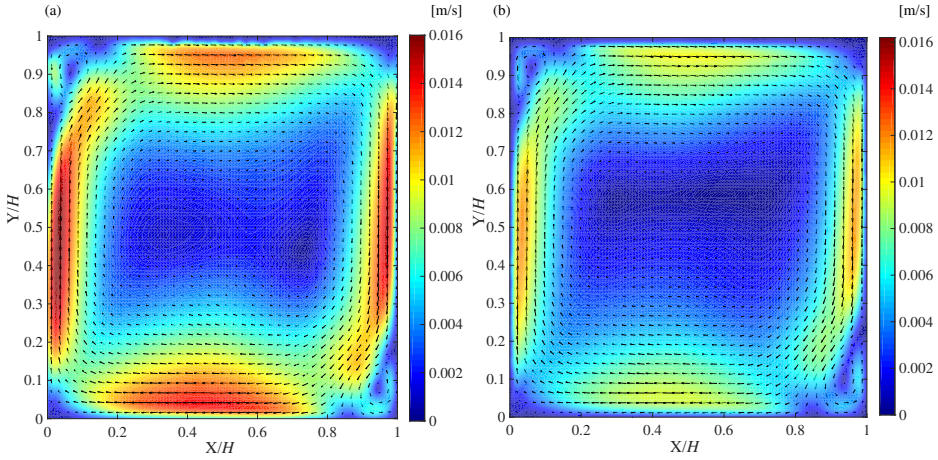


Figure 2.2: Mean velocities ($|\overline{u}|$) contour plots in a vertical cross section at half-depth of the cell ($Z/H = 0.5$). (a) Non-Oberbeck-Boussinesq: $Ra_{NOB} = 6.91 \times 10^8$, $Pr_{NOB} = 4.33$, (b) Oberbeck-Boussinesq: $Ra_{NOB} = 6.74 \times 10^8$, $Pr_{NOB} = 7.24$.

X/H. This consideration, however, cannot be considered as a direct comparison between Sugiyama's *et al.* simulations and our study, because of the difference between 2D simulations and experiments in a 3D geometry and because of similar but not perfectly matching Rayleigh numbers in the two studies ($Ra = 10^8$ in the simulations, $Ra_{NOB} = 6.91 \times 10^8$ in the experiment).

By comparing the NOB and the OB case shown in Figure 2.2, one can observe that the magnitude of the velocity values is larger for the NOB case than for the OB case. The same plots, scaled by $U_{\mathrm{LSC}(GL)}$ and $U_{\mathrm{LSC}(P)}$ are shown in Figure 2.3, panels (a), (c), and (b), (d), respectively. After scaling, the magnitude of the velocity fields is similar in the two cases as can be seen by comparing panels (a) and (c) of Figure 2.3, and panels (b) and (d) of the same figure. The differences before scaling are mainly due to the different Prandtl numbers. In particular the NOB case is the one with the smaller Prandtl number, and consequently the larger magnitude of the velocity field. The velocity scaling allowed us to normalize the velocities by taking into account the influence of the Prandtl number on the LSC velocity. The two small rolls cannot be scaled by the same scaling velocity that was used for the center roll, indicating that more than one characteristic velocity scale is present in the flow. Hence, the relative importance of a characteristic velocity scale of the secondary flow with respect to the LSC velocity scale may change, depending on how large the temperature dependency deviates from Oberbeck-Boussinesq conditions.

For a more quantitative comparison of the two cases, the values of the horizontal and vertical velocity components along the lines $\mathrm{X}/H = 0.5$ and at $\mathrm{Y}/H = 0.5$ are shown in Figures 2.4 and 2.5, scaled by $U_{\mathrm{LSC}\ (GL)}$ and $U_{\mathrm{LSC}\ (P)}$, respectively.

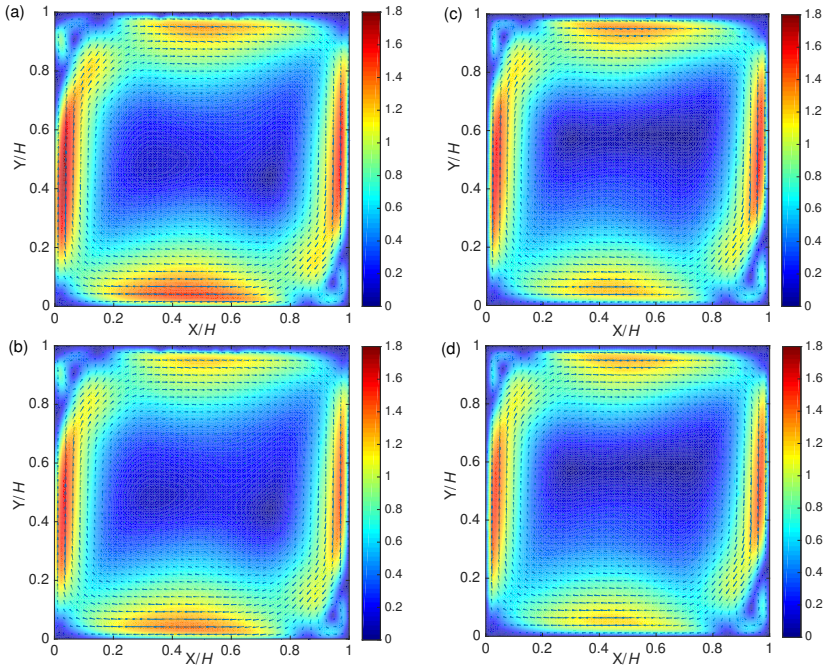


Figure 2.3: Velocities ($|\overline{u}|$) contour plots in a vertical cross section at half-depth of the cell ($Z/H = 0.5$). Velocity values normalized by $U_{LSC\ (GL)}$ in panels (a) and (c) and by by $U_{LSC\ (P)}$ in panels (b) and (d). Panels (a) and (b), Non-Oberbeck-Boussinesq: $Ra_{NOB} = 6.91 \times 10^8$, $Pr_{NOB} = 4.33$; panels (c) and (d) Oberbeck-Boussinesq: $Ra_{NOB} = 6.74 \times 10^8$, $Pr_{NOB} = 7.24$.

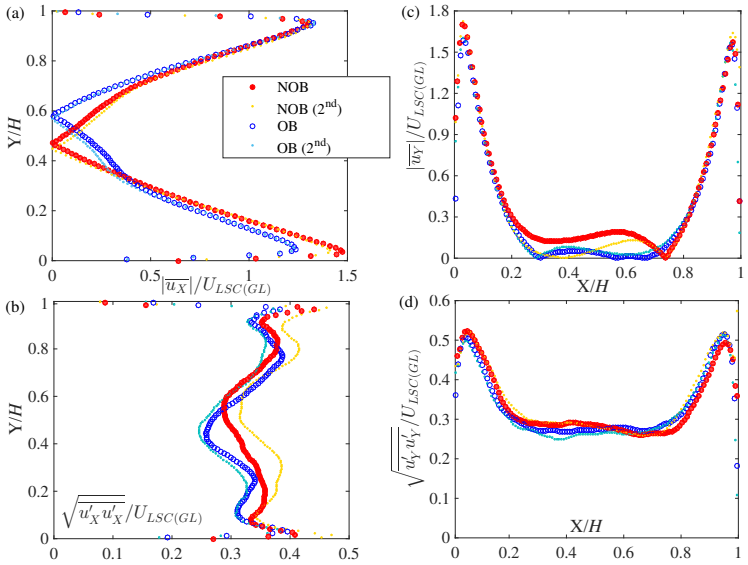


Figure 2.4: Comparison between Non-Oberbeck-Boussinesq and Oberbeck-Boussinesq mean velocity (panels (a) and (c)) and velocity fluctuations RMS (panels (b) and (d)) at half-depth of the cell ($Z/H = 0.5$). Velocity values normalized by $U_{LSC\ (GL)}$. Panels (a) and (b): horizontal component along the line $X/H = 0.5$ and panels (c) and (d): vertical component along the line $Y/H = 0.5$. Non-Oberbeck-Boussinesq : $Ra_{NOB} = 6.91{\times}10^8$, $Pr_{NOB} = 4.33$, Non-Oberbeck-Boussinesq 2^{nd}: $Ra_{NOB} = 6.84{\times}10^8$, $Pr_{NOB} = 4.33$ Oberbeck-Boussinesq: $Ra_{NOB} = 6.74 \times 10^8$, $Pr_{NOB} = 7.24$, Oberbeck-Boussinesq 2^{nd}: $Ra_{NOB} = 6.77 \times 10^8$, $Pr_{NOB} = 7.24$.

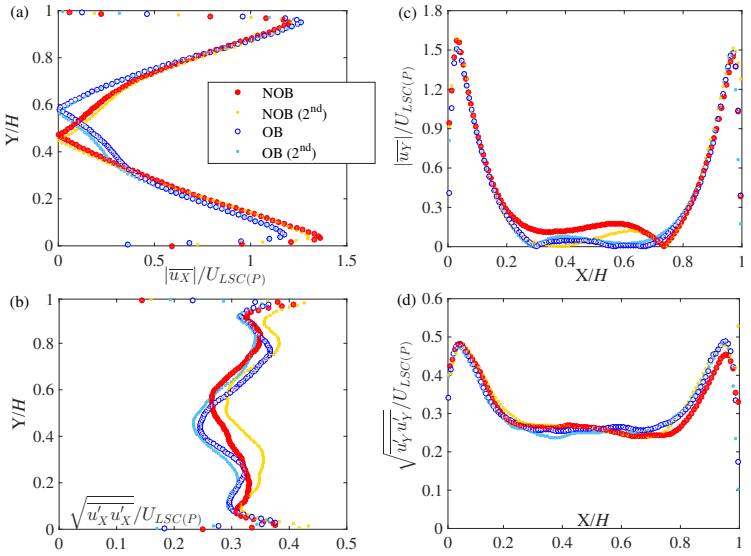


Figure 2.5: Comparison between Non-Oberbeck-Boussinesq and Oberbeck-Boussinesq mean velocity (panels (a) and (c)) and velocity fluctuations RMS (panels (b) and (d)) at half-depth of the cell ($Z/H = 0.5$). Velocity values normalized by $U_{LSC\ (P)}$. Panels (a) and (b): horizontal component along the line $X/H = 0.5$ and panels (c) and (d): vertical component along the line $Y/H = 0.5$. Non-Oberbeck-Boussinesq : $Ra_{NOB} = 6.91{\times}10^8$, $Pr_{NOB} = 4.33$, Non-Oberbeck-Boussinesq 2^{nd}: $Ra_{NOB} = 6.84{\times}10^8$, $Pr_{NOB} = 4.33$ Oberbecl-Boussinesq: $Ra_{NOB} = 6.74 \times 10^8$, $Pr_{NOB} = 7.24$, Oberbeck-Boussinesq 2^{nd}: $Ra_{NOB} = 6.77 \times 10^8$, $Pr_{NOB} = 7.24$.

From Figure 2.4 (and Figure 2.5), panel (a), it can be seen that in the NOB case the peak of the horizontal velocity component close to the bottom wall is significantly larger than close to the top wall. The difference is about 13.4%, which is larger than the statistical uncertainty of 3% and 7% of the NOB case and the OB case, respectively. Also, the slope of the boundary layer at the bottom wall is steeper than at the top for the NOB case. The increase of the velocity close to the bottom wall of the cell with respect to the region close to the top wall can be explained by the the lower values of the kinematic viscosity close to the hot bottom wall of the cell. These findings are consistent with the NOB effects observed in 3D numerical simulations by Horn *et al.* [7, 8]. Indeed they also note an increase of the horizontal velocity magnitude and a reduction of the kinetic boundary layer thickness near the bottom wall of the cell, with respect to the top wall, due to the temperature dependency of the kinematic viscosity. To show that the NOB effects seen in the experiment are due to the temperature dependency of the fluid properties and that they do not depend on the particular apparatus used for the measurements, an Oberbeck-Boussinesq case (see Table 2.2) was done in the same set-up and used for comparison in the plots. This case, being more Oberbeck-Boussinesq than the NOB case studied, is characterized by more symmetric top-bottom profiles, with a slight asymmetry of the top-bottom velocity peaks just above the uncertainty limit of 7% (see Figure 2.4 and Figure 2.5).

From Figure 2.4 (and Figure 2.5), panel (a) one can also observe that the horizontal velocity component plotted along the line $X/H = 0.5$ shows two linear parts in the central region of the cell, at $0.1 \lesssim Y/H \lesssim 0.3$ and $0.7 \lesssim Y/H \lesssim 0.9$, for both the NOB and the OB case. This was also observed by Xia *et al.* [19] under OB conditions at similar Rayleigh number. While the slopes of the horizontal velocity component in Figure 2.4 (and 2.5), panel (a) for NOB and OB conditions are similar in the top part $(0.7 \lesssim Y/H \lesssim 0.9)$, they are different near the bottom $(0.1 \lesssim Y/H \lesssim 0.3)$. This is related to the large difference between the horizontal velocity peaks close to the bottom wall compared to the top in the NOB case. It is also interesting to observe a further difference between the two cases in the central region of the cell for $0.3 \lesssim Y/H \lesssim 0.7$, where both the NOB and the OB profiles show an inflection point, albeit at different locations. In particular from figure 2.4 (and 2.5), it can be seen that both the mean horizontal (panel (a)) and vertical (panel (c)) velocity components values are different from zero at the center of the cell (Y/H = 0.5 or X/H = 0.5, respectively) for the NOB case of quantities that are larger than the statistical uncertainty. This effect is also present in the OB values of the mean horizontal velocity component (Figures 2.4 and 2.5, panel (a)). Since for a perfect OB case, one would expect a zero mean velocity value at the center of the cell, deviations from zero show that also the nominal OB case is affected by NOB effects. This top-bottom asymmetry NOB effect agrees with previous numerical studies [7, 8] (Figure 9) and confirms them experimentally for the first time.

Also the values of the RMS's of the horizontal velocity component along the line $Y/H = 0.5$, presented in Figure 2.4 and 2.5, panel (b), show a top-bottom asymmetry, but it is within the statistical uncertainty. The vertical component of the velocity RMS along the line $Y/H = 0.5$ does not show evident asymmetries in the

two cases (Fig. 2.4 panel (d)).

2.4.2. Turbulent kinetic energy

The turbulent kinetic energy (k) at $Z/H = 0.5$ for the NOB case and the OB case are shown in Figure 2.6, after scaling by $U_{LSC\ (GL)}$ (panels (a) and (c)) and by $U_{LSC\ (P)}$ (panels (b) and (d)). The NOB case is presented in panels (a) and (b) and the OB case in panels (c) and (d). The contour plots of both cases show similar shape and magnitude after scaling. For both cases, the regions with the largest values of k are in the vicinity of the corners. These peaks are related to the two counter-rotating rolls at the top-left and at the bottom-right corner of the cell shown in Figure 2.3. The fluctuations of the velocity are indeed higher immediately before the impingement of the two vertical jet regions onto the two horizontal plates. From instantaneous flow visualizations one can see that the two vertical jets close to the left and right walls are unstable and oscillate before the impingement onto the horizontal walls. This leads to the high values of the turbulent kinetic energy at the top-left corner and at the bottom-right corner of the cell.

From Figure 2.6, panel (a) and (b), NB effects are visible as an increase of the turbulent kinetic energy in the bottom-left quadrant of the cell with respect to the top-right quadrant. The OB reference case, plotted in panels (c) and (d) of Figure 2.6 is instead more symmetric. To quantify this NB effect better, in Figures 2.8 and 2.9 the values of the turbulent kinetic energy along the horizontal axis X/H at three different heights in the bottom-left quadrant ($Y/H = 0.1, 0.2, 0.3$) and in the top quadrant ($Y/H = 0.7, 0.8, 0.9$) are plotted for both the NOB and the OB case, with both scaling models. By comparing panels (a) and (b) of Figure 2.8 (or Figure 2.9), it can be seen that the values of k are slightly larger in the bottom-left quadrant of the cell shown in panel (b), with respect to the top-right quadrant shown in panel (a) for the NOB case (relative increase of about 20%). In the repeated NOB experiment shown in Figure 2.7 and in panels (a) and (b) of Fig.2.8 (and Fig.2.8) as 2^{nd} exp., however this NOB asymmetry was not detected. The reference OB case (see panels (c) and (d) of Figures 2.8 and 2.9) shows a good symmetry within experimental uncertainty, that was confirmed by a repeated experiment shown as contour plot in panels (c) and (d) of Figure 2.7 and as one-line profiles at several heights Y/H in panels (c) and (d) of Figures 2.8 and 2.9. The different values of k between the NOB experiments can be attributed to statistical uncertainty of the velocity measurements as quantified in equations (2.10) and (5.14).

In conclusion, from this experimental turbulent kinetic energy study it was seen that while there is symmetry at OB conditions, (verified by two independent experiments), at NOB conditions there is an tendency towards an asymmetric distribution of the values of k. In particular, a relative increase of the values of k was observed at the bottom-right quadrant of the cell, with respect to the top-left quadrant of about 20%. This asymmetry, however, was difficult to detect experimentally and it was not confirmed in a second experiment done at similar experimental conditions. Differences between the first and the second NOB experiments were due to statistical uncertainty in the velocity measurements.

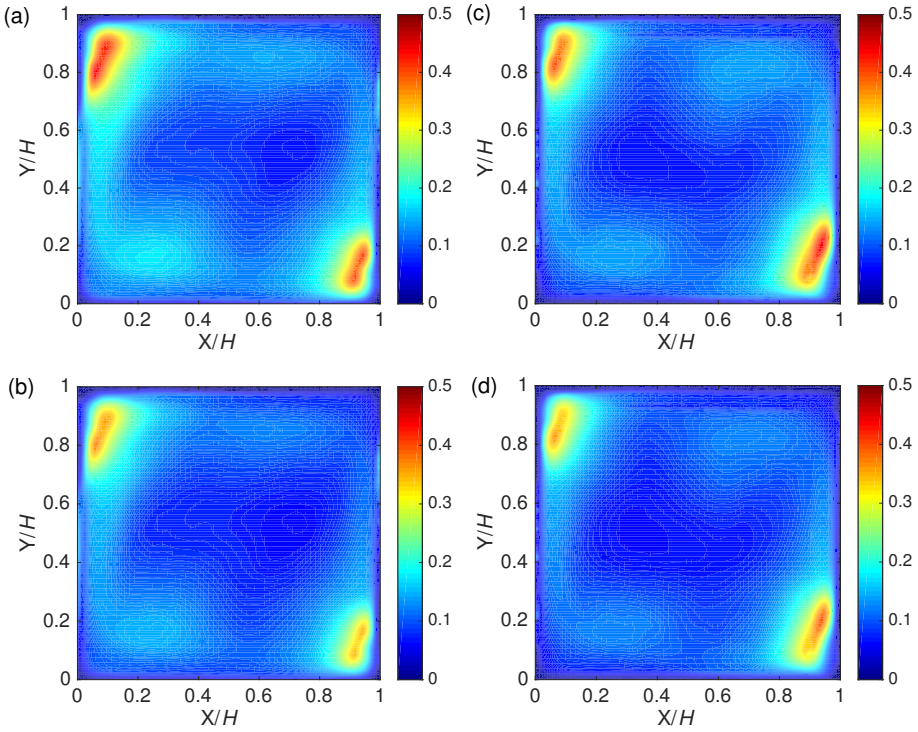


Figure 2.6: Turbulent kinetic energy in a vertical cross section at half-depth of the cell ($Z/H = 0.5$). Values normalized by $U_{LSC\ (GL)}$ in panels (a) and (c) and by $U_{LSC\ (P)}$ in panels (b) and (d). Panels (a) and (b), Non-Oberbeck-Boussinesq: $Ra_{NOB} = 6.91 \times 10^8$, $Pr_{NOB} = 4.33$; panels (c) and (d), Oberbeck-Boussinesq: $Ra_{NOB} = 6.74 \times 10^8$, $Pr_{NOB} = 7.24$.

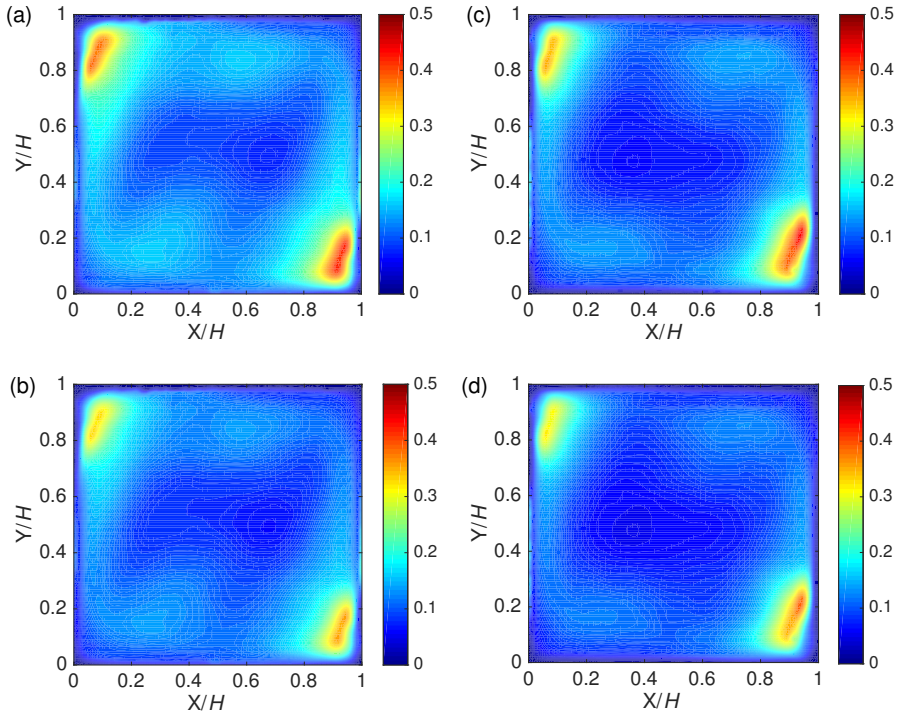


Figure 2.7: Turbulent kinetic energy in a vertical cross section at half-depth of the cell ($Z/H = 0.5$) (repeated experiments). Values normalized by $U_{LSC\ (GL)}$ in panels (a) and (c) and by $U_{LSC\ (P)}$ in panels (b) and (d). Panels (a) and (b), Non-Oberbeck-Boussinesq 2^{nd}: $Ra_{NOB} = 6.84 \times 10^8$, $Pr_{NOB} = 4.33$; panels (c) and (d), Oberbeck-Boussinesq 2^{nd}: $Ra_{NOB} = 6.77 \times 10^8$, $Pr_{NOB} = 7.24$.

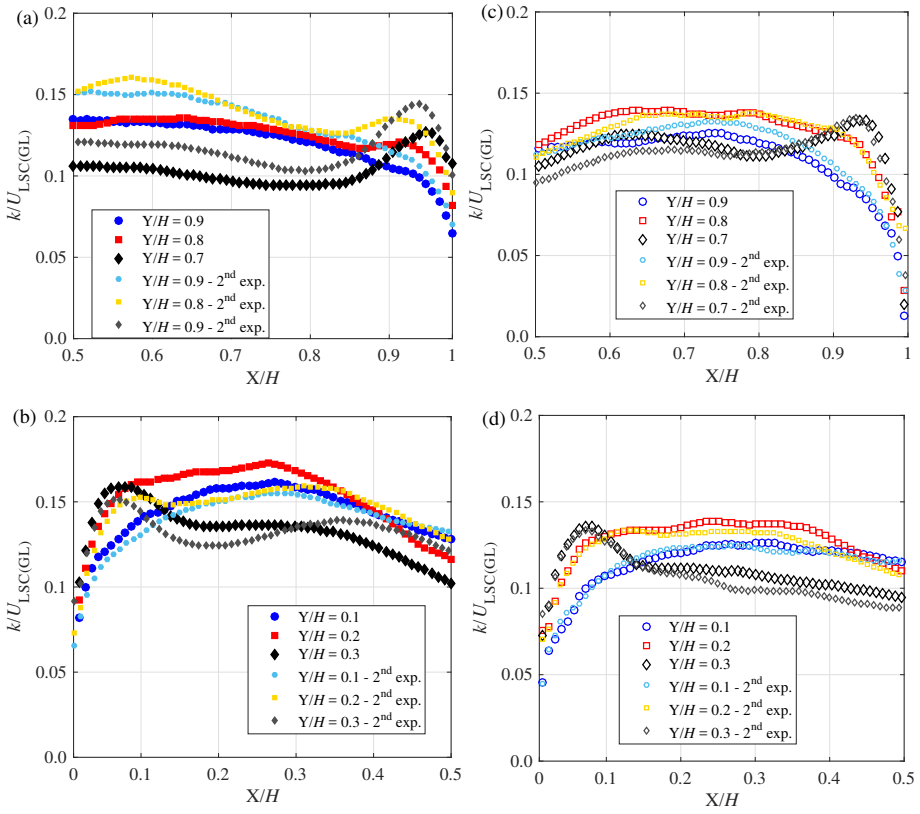


Figure 2.8: One-line plots of the turbulent kinetic energy values at several heights Y/H (Y/H = 0.1, 0.2, 0.3, 0, 7, 0.8, 0.9) along the axis X/H at Z/H = 0.5. Values normalized by $U_{LSC\ (GL)}$. a), b), Non-Oberbeck-Boussinesq: $Ra_{NOB} = 6.9 \times 10^8$, $Pr_{NOB} = 4.33$, Non-Oberbeck-Boussinesq 2^{nd}: $Ra_{NOB} = 6.84 \times 10^8$, $Pr_{NOB} = 4.33$. c), d), Oberbeck-Boussinesq: $Ra_{NOB} = 6.7 \times 10^8$, $Pr_{NOB} = 7.24$, Oberbeck-Boussinesq 2^{nd}: $Ra_{NOB} = 6.77 \times 10^8$, $Pr_{NOB} = 7.24$.

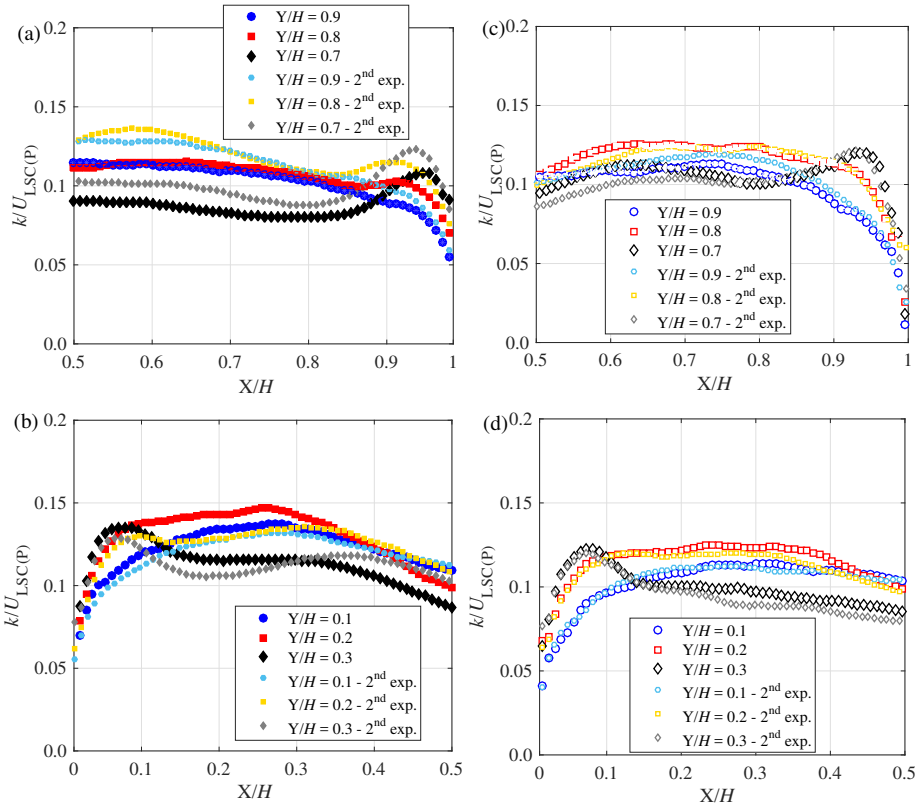


Figure 2.9: One-line plots of the turbulent kinetic energy values at several heights Y/H (Y/H = 0.1, 0.2, 0.3, 0, 7, 0.8, 0.9) along the axis X/H at Z/H = 0.5. Values normalized by $U_{LSC\ (P)}$. a), b), Non-Oberbeck-Boussinesq: $Ra_{NOB} = 6.9 \times 10^8$, $Pr_{NOB} = 4.33$, Non-Oberbeck-Boussinesq 2^{nd}: $Ra_{NOB} = 6.84 \times 10^8$, $Pr_{NOB} = 4.33$. c), d), Oberbeck-Boussinesq: $Ra_{NOB} = 6.7 \times 10^8$, $Pr_{NOB} = 7.24$, Oberbeck-Boussinesq 2^{nd}: $Ra_{NOB} = 6.77 \times 10^8$, $Pr_{NOB} = 7.24$.

2.5. Conclusions

The PIV velocity fields of two RB experiments, one at NOB conditions and the other one at OB conditions, were compared after making them non-dimensional with their LSC velocities. Two LSC velocities were considered, one calculated from the Grossmann-Lohse theory [12–14] and another one calculated from the model of Pandey *et al.*[15, 16]. The latter matched the experimental values of both the NOB case and the OB one very well, with a relative difference of 7.5% for both cases. The U_{LSC} predicted with the GL theory instead matched the experimental values of the NOB and of the OB case with a relative difference of 73% and 60%, respectively. It was also observed that the ratio between the measured U_{LSC} for the NOB case and the OB case is matched slightly better by the predictions of the GL theory, than by the Pandey model. The presented data were scaled with both LSC velocities, in order to show that the choice of one scaling velocity with respect to the other one does not make any difference with regard to the NOB effect found.

A NOB effect was found in the mean horizontal velocity component of the NOB case, where a top-bottom asymmetry with the bottom velocity peak larger than the top one of about 13% was found. This top-bottom asymmetry of the mean velocity was seen to be very weak, just above the uncertainty limit of 7%, in the nominal OB case, where the material properties only weakly depend on temperature.

It was also seen that the value of the mean horizontal velocity component at half height of the cell is not zero for both cases, of a value that is larger than the experimental uncertainty. This shows that also the nominal OB case was influenced by the same NOB effect. In the NOB case, also the mean vertical velocity value at half depth of the cell is different from zero. Since the velocity fields of the two cases were acquired in the same set-up, differences among them can be attributed to different temperature dependency of the material properties of the two fluids used and not to the experimental set-up.

This asymmetric velocity profile is a NOB effect well know in the literature [5] from theoretical and numerical studies that was never experimentally proven before. It agrees well with previous numerical studies [7, 8] and confirms them experimentally.

This was a preliminary study about NOB effects on the velocity field of RB convection, before moving to the more complex case of supercritical conditions, where all the fluid properties can be outside the OB approximation. In the next chapter (Chapter 3) the heat transfer in RB convection at supercritical conditions is studied experimentally, while in Chapter 5 the feasibility of PIV measurements and PIV velocity fields at supercritical conditions are discussed.

References

[1] V. Valori, G. Elsinga, M. Rohde, M. Tummers, J. Westerweel, and T. van der Hagen, *Experimental velocity study of non-Boussinesq Rayleigh-Bénard convection,* Physical Review E **95**, 053113 (2017).

[2] A. Oberbeck, *Ueber die Wärmeleitung der Flüssigkeiten bei Berücksichtigung der Strömungen infolge von Temperaturdifferenzen,* Annalen der Physiks **243**, 271 (1879).

[3] J. Boussinesq, *Théorie analytique de la chaleur*, Vol. 2 (Gauthier-Villars (Paris), 1903).

[4] J. Y. Yoo, *The turbulent flows of supercritical fluids with heat transfer,* Annual Review of Fluid Mechanics **45**, 495 (2013).

[5] G. Ahlers, E. Brown, F. F. Araujo, D. Funfschilling, S. Grossmann, and D. Lohse, *Non-Oberbeck–Boussinesq effects in strongly turbulent Rayleigh–Bénard convection,* Journal of Fluid Mechanics **569**, 409 (2006).

[6] K. Sugiyama, E. Calzavarini, S. Grossmann, and D. Lohse, *Flow organization in two-dimensional non-Oberbeck–Boussinesq Rayleigh–Bénard convection in water,* Journal of Fluid Mechanics **637**, 105 (2009).

[7] S. Horn, O. Shishkina, and C. Wagner, *On non-Oberbeck–Boussinesq effects in three-dimensional Rayleigh–Bénard convection in glycerol,* Journal of Fluid Mechanics **724**, 175 (2013).

[8] S. Horn and O. Shishkina, *Rotating non-Oberbeck–Boussinesq Rayleigh–Bénard convection in water,* Physics of Fluids **26**, 055111 (2014).

[9] J. Zhang, S. Childress, and A. Libchaber, *Non-Boussinesq effect: Asymmetric velocity profiles in thermal convection,* Physics of Fluids **10**, 1534 (1998).

[10] M. Steunebrink, *Effect of surface roughness on flow and heat transfer in Rayleigh-Bénard convection*, Master's thesis, Delft University of Technology, The Netherlands (2013).

[11] E. Lemmon, M. Huber, and M. McLinden, *NIST reference database 23: reference fluid thermodynamic and transport properties-REFPROP, version 9.1,* Standard Reference Data Program (2013).

[12] S. Grossmann and D. Lohse, *Scaling in thermal convection: a unifying theory,* Journal of Fluid Mechanics **407**, 27 (2000).

[13] S. Grossmann and D. Lohse, *Thermal convection for large Prandtl numbers,* Physical Review Letters **86**, 3316 (2001).

[14] S. Grossmann and D. Lohse, *Prandtl and Rayleigh number dependence of the Reynolds number in turbulent thermal convection,* Physical Review E **66**, 016305 (2002).

[15] A. Pandey and M. K. Verma, *Scaling of large-scale quantities in Rayleigh-Bénard convection,* Physics of Fluids **28**, 095105 (2016).

[16] A. Pandey, A. Kumar, A. G. Chatterjee, and M. K. Verma, *Dynamics of large-scale quantities in Rayleigh-Bénard convection,* Physical Review E **94**, 053106 (2016).

[17] G. Ahlers, S. Grossmann, and D. Lohse, *Heat transfer and large scale dynamics in turbulent Rayleigh-Bénard convection,* Reviews of Modern Physics **81**, 503 (2009).

[18] R. J. Stevens, E. P. van der Poel, S. Grossmann, and D. Lohse, *The unifying theory of scaling in thermal convection: the updated prefactors,* Journal of Fluid Mechanics **730**, 295 (2013).

[19] K.-Q. Xia, C. Sun, and S.-Q. Zhou, *Particle image velocimetry measurement of the velocity field in turbulent thermal convection,* Physical Review E **68**, 066303 (2003).

[20] K. Sugiyama, R. Ni, R. J. A. M. Stevens, T. S. Chan, S.-Q. Zhou, H.-D. Xi, C. Sun, S. Grossmann, K.-Q. Xia, and D. Lohse, *Flow reversals in thermally driven turbulence,* Physical Review Letters **105**, 034503 (2010).

[21] M. Chandra and M. K. Verma, *Dynamics and symmetries of flow reversals in turbulent convection,* Physical Review E **83**, 067303 (2011).

[22] M. Chandra and M. K. Verma, *Flow reversals in turbulent convection via vortex reconnections,* Physical Review Letters **110**, 114503 (2013).

3

Thermally driven heat transfer in the supercritical fluid region

3.1. Introduction

Heat transfer in Rayleigh-Bénard (RB) convection under the constrains of Oberbeck-Boussinesq (OB) conditions [1, 2] has been extensively studied in the past (see recent reviews [3–5]). At these conditions the dependency of the fluid properties on temperature is very weak, and the fluid properties can be considered uniform throughout the flow domain. With this hypothesis, the Oberbeck-Boussinesq (OB) approximation [1, 2] allows to simplify the equation for continuity, the Navier-Stokes (NS) equations, and the energy conservation equation. The approximation consists of neglecting the temperature dependency of the fluid properties in all the terms of the fluid governing equations, except for the density in the buoyancy term, where it is supposed to depend linearly on temperature. A method to explicitly quantify its validity range in natural convection for Newtonian fluids was proposed by Gray and Giorgini [6]. This method assumes that all fluid properties vary linearly with temperature and pressure, and allows to compute limits on the fluid layer depth and the temperature difference applied over the layer, for liquids and gases, in order to satisfy the requirements of the Boussinesq approximation.

The unifying theory of thermal convection proposed by Grossmann and Lohse (GL theory) [7–9] allows the prediction of the non-dimensional heat transfer through the cell, expressed by the Nusselt number, as a function of the Rayleigh and the Prandtl numbers. It was developed under the OB approximation for aspect-ratio one cells. The aspect ratio of a RB-cell is the ratio between its horizontal and vertical dimensions. The GL theory can be applied also for aspect ratios larger than unity, since it was seen from experiments that the heat transfer depends only very weakly on it, for aspect ratios equal or larger than unity [10–15].

When the temperature and/or pressure dependency of the fluid properties cannot be neglected, as it is often the case in experiments, engineering applications and nature, non Oberberck-Boussinesq (NOB) effects are present. NOB effects were studied experimentally, theoretically, and numerically [16–22]. Ahlers *et al.* [18] presented an experimental and theoretical study on the effects of NOB conditions on the Nusselt and Reynolds number. The working fluid in their study is water at atmospheric pressure, which exhibits significant changes of the kinematic viscosity and the volumetric thermal expansion coefficient, in the range of temperatures considered. They showed that NOB effects in the Nusselt number are mainly due to the second and higher order temperature dependencies of the material properties. They also extended the Prandtl-Blasius boundary layer theory [23, 24] to temperature dependent kinematic viscosity and thermal conductivity. In Chapter 2 of this thesis, an experimental study on NOB effects on the velocity fields of RB convection was shown. A top-bottom asymmetry in the time-average velocity profile was found, that confirmed results from previous numerical studies done by Horn *et al.* [20, 21].

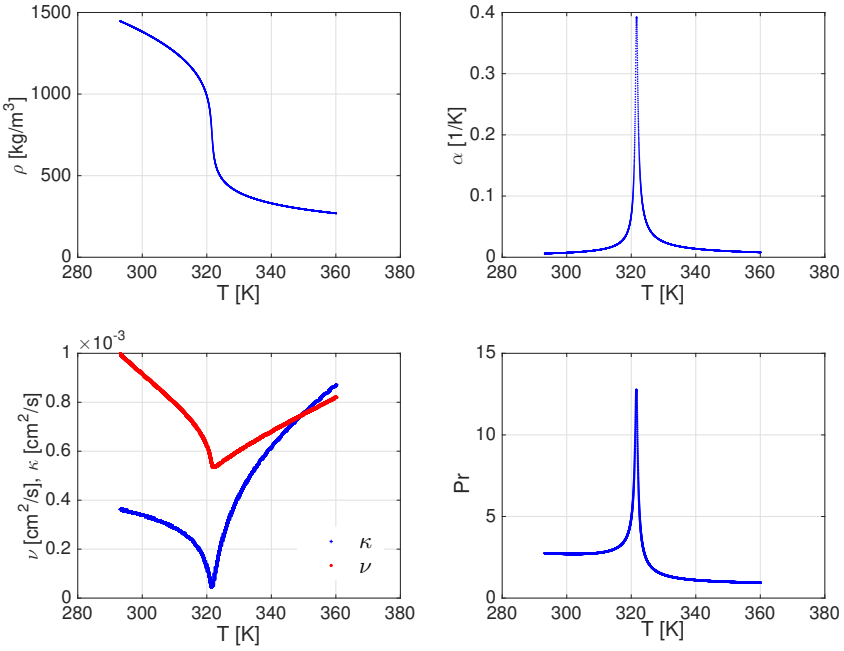


Figure 3.1: Fluid properties of SF_6 as a function of temperature at 4 MPa. ρ: density, ν: kinematic viscosity, κ: thermal diffusivity, Pr: Prandtl number. (Critical point of SF_6: 318.72 K, 3.755 MPa). Properties taken from NIST RefProp version 9.1 [25]

In the gas-liquid supercritical region the temperature dependency of the fluid

properties is very strong, (e.g. see Figure 3.1), and it represents an extreme case of NOB conditions. In this region all material properties significantly vary with temperature and pressure. These variations are expected to play a role in the heat transfer mechanism through the cell. No singular NOB condition (e.g. strong temperature dependency of one fluid property) can easily be disconnected from the others in its effects on the global heat transfer and fluid flow structure throughout the cell. The OB approximation is not valid, and the current heat transfer theories and turbulence models fail to describe the physics of the flow [26–29].

The present study aims at quantifying NOB effects in the global heat transfer through a RB-cell in the gas-liquid supercritical region, under strong NOB conditions. Heat transfer measurements were performed in order to check whether the Rayleigh and Prandtl numbers, calculated with the fluid properties at the average top-bottom temperature of the cell, can predict the heat transfer through the cell also at supercritical conditions. The data were acquired at constant Rayleigh and Prandtl numbers at different values of the mean temperature and pressure in the cell. A relative increase of at least 16% in the Nusselt number with respect to predictions for Oberbeck-Boussinesq conditions was found at supercritical conditions, which was ascribed to a NOB effect.

3.2. Experimental set-up

The experimental facility used for the heat transfer measurements at supercritical conditions is schematically represented in Figure 3.2. It is located at the Max Planck Institute for Dynamics and Self-Organization in Göttingen (Germany), and it has been used within the European project EuHIT [30]. The working fluid used for this study is sulfur hexafluoride (SF_6). A description of the whole facility is presented to show how the experimental conditions were reached and maintained. The main component of the facility is a Rayleigh-Bénard cell that is filled with SF_6 at supercritical conditions. The cell is filled through a high pressure circuit that starts with an SF_6 high pressure bottle. From the bottle the fluid flows into a reservoir, which acts as a pressure regulator. Here the pressure in a fixed volume of fluid, 0.4 liters, is set by adjusting its temperature. The pressure control operates through a proportional-derivative (PD) feedback algorithm, whose inputs are the measured pressure and the set pressure. The set pressure, which corresponds to the pressure inside the cell, is measured by a pressure transducer (Paroscientific series 9000-1K, made of Digiquartz®) with full temperature compensation and linearized outputs, with a precision of 50 mbar. The reservoir is equipped with both an electrical power strip and a water cooling circuit, as schematically drawn in Figure 3.2. They respectively provide and subtract thermal power to the accumulator cylinder and are controlled by the feedback algorithm with PD control, in order to reach the set pressure in the fluid. The temperature of the water in the cooling circuit is in turn set by a thermal circulator (ThermoScientific, model: AC 150-A25). The water cooling circuit of the reservoir is also schematically represented in Figure 3.2. Both the electrical power strip and the cooling circuit of the reservoir allow to set the desired value of the pressure in the reservoir, and hence in the fluid inside the cell, up to 5.5 MPa.

The Rayleigh-Bénard cell is cooled by water pumped on its top plate, and it is elec-

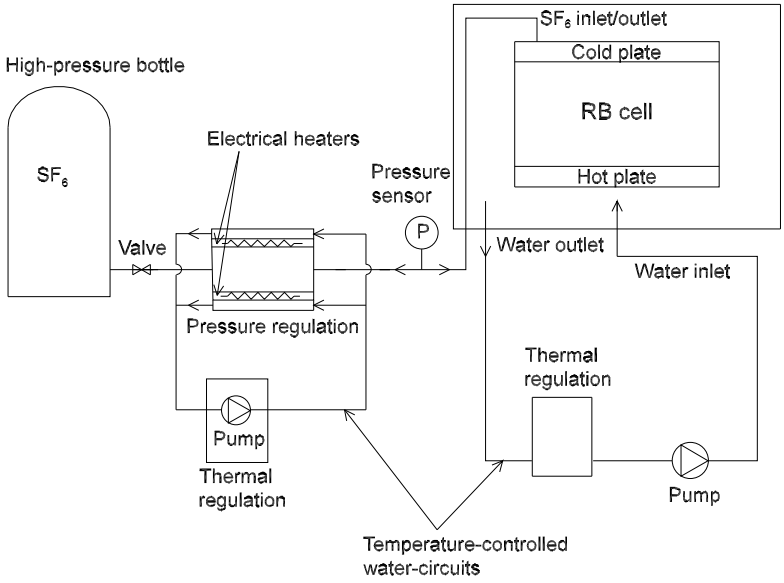


Figure 3.2: Sketch of the experimental facility.

trically heated at the bottom plate, via an electric film heater (90 Ω). A feedback control algorithm PD (an independent control with respect to the one of the pressure reservoir) allows to set the temperatures of the plates. The input parameters of the feedback control are the temperatures of the plates and of the side wall of the cell, measured by thermistors. The output parameters are signals provided to the thermal bath of the cooling circuit and to the electrical heater of the cell.

3.2.1. Rayleigh-Bénard cell

The Rayleigh-Bénard cell is a cylinder with stainless steel lateral walls and top and bottom copper plates. The lateral walls are 4.4 mm thick to sustain pressures up to 100 bars. The internal diameter of the cylinder is 101.6 mm and the vertical distance between them (internal height of the cylinder) is 50.8 mm. Hence the aspect ratio of the cell is 2.

The cell is cooled by water from its top plate as schematically represented in Figure 3.3. The cooling system of the cell is a cylinder within which the cylindrical cell is inserted coaxially. The cell is insulated with foam rubber on all its faces, except for the top plate. Cooling water enters from the bottom of the containing cylinder and rises through an annular section. Then it spreads and circulates on the top plate of the cell. From this position the cooling water descends through another annular section, which is coaxial and external to the previous one with the rising flow.

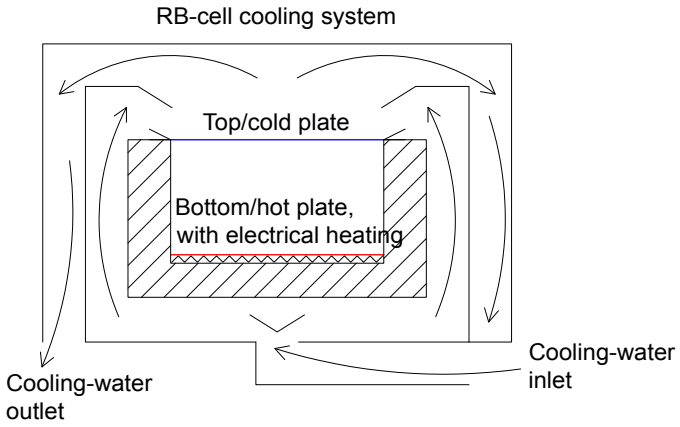


Figure 3.3: Sketch of a vertical cross-section of the cooling system of the Rayleigh-Bénard cell. The insulation with foam rubber around the lateral wall of the cell and below its bottom plate is indicated with hatches. The two conducting walls of the cell are indicated by a red line (bottom plate surface) and a blue line (top plate surface). The arrows indicate the direction of the cooling water that enters the cylinder from the bottom and is pumped on the top plate to cool it. Note that the cooling water goes out from the cylinder only from one side.

The cylinder containing the cell is a part of a circuit that comprises also of a thermal regulation bath (ThermoScientific Accel model 500 LC) and a pump (see sketch in Fig. 3.2). The temperature of the water in the thermal bath is controlled by a feedback PD algorithm (a third one) on the basis of temperature measurements with two thermistors inside the top plate of the cell.

The bottom plate of the cell is electrically heated by means of the Joule effect with a Kapton film heater (90 Ohm, Vincent Industrietechnik Luedenschaid) glued on its bottom surface. Also this electrical heating strip is controlled by a PD feedback control on the basis of the temperature measured with two thermistors inside the bottom plate.

Temperature measurements

Negative Temperature Coefficient (NTC) thermistors (Honeywell) are built inside the top and bottom plates of the cell, two for each plate, as shown in Figure 3.4. They are calibrated against a PT-100 thermocouple (PT-103-70 H, LakeShore). The uncertainty in the calibration for the range of temperatures of the experiments is about 30 mK. This temperature uncertainty is sufficiently small to allow to neglect the uncertainty it leads in the fluid properties, as verified by taking the fluid properties from the NIST and the CoolProp databases [25, 31]. The temperature of each plate is calculated as the mean value between the temperatures of the two thermistors in the plate.

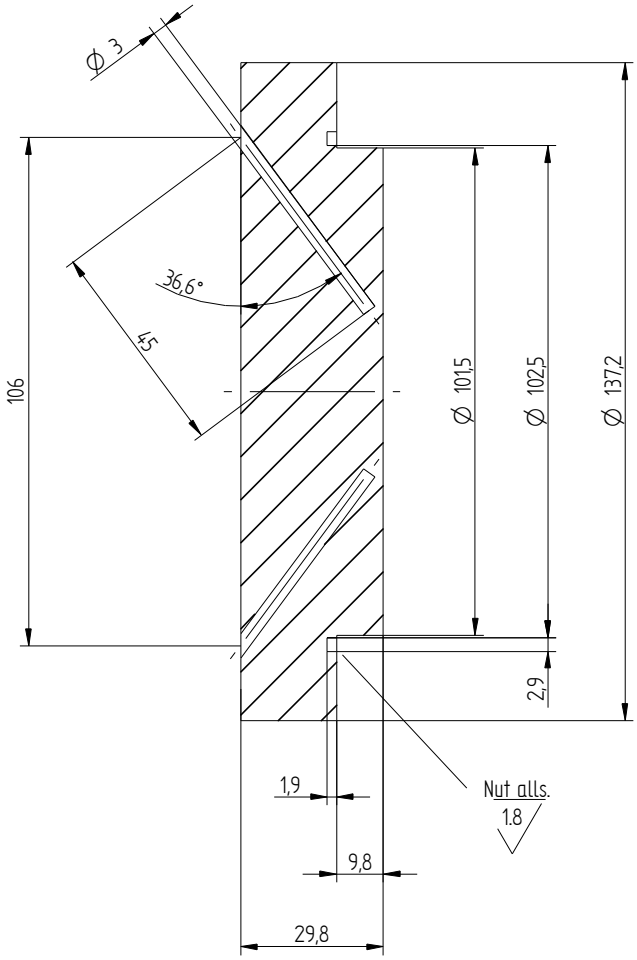


Figure 3.4: Vertical cross-section (90° rotated in clockwise direction) of the bottom copper plate of the cell. From the section the two holes for the thermocouples are visible.

Pressure measurements

As already specified in the general description of the experimental facility, the pressure of the apparatus is measured by a pressure transducer. The uncertainty in the absolute value of the pressure is 50 mbar. This value represents the difference between the simultaneous measurements of two different pressure transducers in the same point of the set-up. This pressure uncertainty is sufficiently small to allow to neglect the uncertainty it leads in the fluid property, as verified by taking the fluid properties from the NIST and the CoolProp databases [25, 31].

Heat transfer measurements

Heat transfer through the cell was determined from the measured power provided to the bottom plate in order to maintain the set temperature difference (ΔT) between the plates. Since the cell was insulated both at the bottom and lateral walls, the heat received from the heating strip on the bottom plate was almost entirely transmitted to the top plate. In order to quantify the heat transmitted by the lateral walls, dissipated through the external insulation material and transmitted via radiation, experiments were made in a cell with vacuum inside at several temperature differences between the plates. This heat transfer is called parasitic heat loss (Q_p). It was measured by the power supplied to the heating strip to maintain a desired temperature difference between the top and bottom plates of the cell with vacuum. Measurements of Q_p for several ΔT are shown in Figure 3.5. These data are fitted by a quadratic curve specified in equation (3.1), whose coefficients are given in equations (3.2), (3.3) and (3.4) with 95% confidence bounds within parenthesis.

$$Q_p = a + b \times \Delta T + c \times \Delta T^2, \tag{3.1}$$

$$a = 0.02432 \ (-0.3881, 0.4367) \tag{3.2}$$

$$b = 0.4434 \ (0.3647, 0.522) \tag{3.3}$$

$$c = 0.0002336 \ (-0.002817, 0.003284) \tag{3.4}$$

The value of Q_p extrapolated with formula (3.1) was subtracted from the global heat transfer measured when the cell was filled with SF_6 for each specific ΔT. The values of Q_p were always within 10% of the measured value for Q through the cell.

Time-convergence of the experiments For each measurement, data were acquired for 12 hours. After the first 6 hours, all the measured experimental parameters appeared to be stable within the measurement accuracy, as shown in the plots of Figure 3.6 for the heat transfer through the cell Q, the pressure of the cell, p, the temperature of one thermistor in the bottom plate, T_{b1}, the difference of temperature between the two thermistors in the bottom plate, T_{b1} and T_{b2}, the temperature of one thermistor in the top plate, T_{t1} and the difference of temperature between the two thermistors in the top plate, T_{t1}, and T_{t2}. The values taken as experimental results were time averages from hour 6 to hour 12. The standard deviation (std) of the heat transfer measurements time series is about 2.5%.

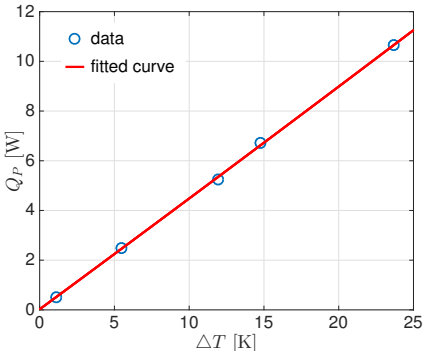


Figure 3.5: Parasite heat losses (Q_p) through the lateral walls of the cell and the external insulation material, as a function of the difference of temperature between the plates ($\triangle T$), when the cell is under vacuum. Empty circles represent the measured data and the red line is their fitting curve.

This value is sufficiently small to distinguish differences in heat transfer among the experimental results.

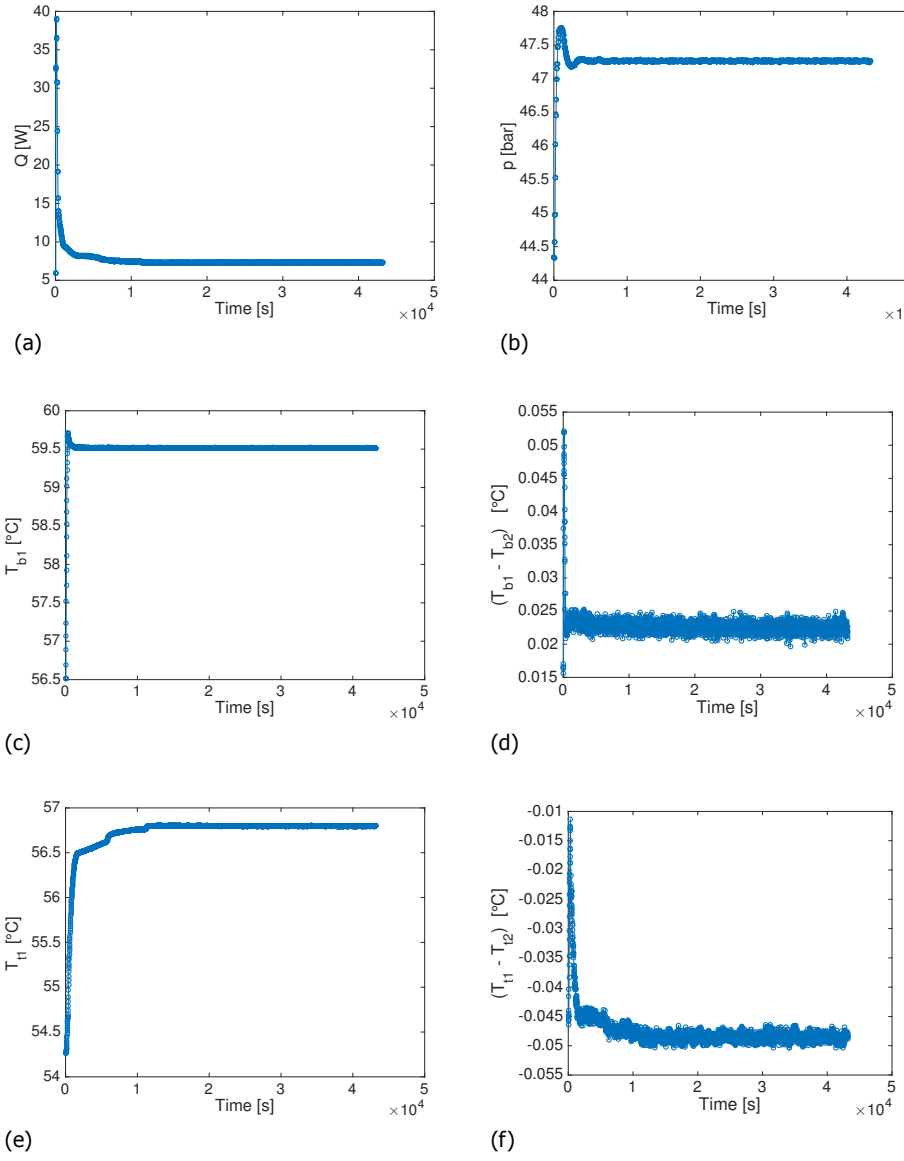


Figure 3.6: Time convergence of the experimental parameters: (a) Power given to the bottom plate, corrected for the dissipated heat, Q; (b) Pressure of the cell, p; (c)Temperature of one thermistor in the bottom plate, T_{b1} ;(d)Temperature difference between the two thermistors in the bottom plate T_{b1} and T_{b2}; (d) Temperature of one thermistor in the top plate, T_{t1} (e) Temperature difference between the two thermistors in the top plate T_{t1} and T_{t2}.

3.3. Experimental programme

At supercritical conditions the fluid properties strongly depend on temperature and pressure (see e.g. Figure 3.1 and the Prandtl number values plotted in Figure 3.7) and the Oberbeck-Boussinesq approximation cannot be applied [6]. Under OB conditions, the non-dimensional heat transfer through the cell, Nusselt number (Nu), can be predicted as a function of the Rayleigh and Prandtl numbers with the Grossmann-Lohse theory [7–9]. The Nusselt number is defined as:

$$Nu \equiv \frac{q}{q_{cond}}, \tag{3.5}$$

where q is the heat flux through the fluid from the bottom to the top, defined as the ratio between the electrical power given to the bottom plate (Q) and the surface of the plate (A):

$$q \equiv \frac{Q}{A}. \tag{3.6}$$

and q_{cond} is the heat transferred through the cell by conduction only. For OB conditions, it is defined as:

$$q_{cond} \equiv \frac{\lambda \Delta T}{H}, \tag{3.7}$$

where λ is the thermal conductivity of the fluid and it is a linear function of temperature. ΔT is the difference between the temperature of the bottom plate, T_b, and of the top plate, T_t, of the cell.

The non-dimensional Rayleigh and Prandtl numbers, defined from the non-dimensionalization of the Navier-Stokes equations and the energy conservation equations under OB conditions, are not sufficient to predict the non-dimensional heat transfer through the cell, at supercritical conditions. The Rayleigh and Prandtl numbers under NOB conditions due to strong temperature dependency of the fluid properties were defined in Chapter 2. They are defined again in this chapter to take into account also the strong pressure dependency that characterizes fluids at SC conditions. They are calculated at the mean temperature (T_m) and pressure (p_m) of the cell. T_m is defined as:

$$T_m \equiv \frac{T_t + T_b}{2}, , \tag{3.8}$$

while p_m is assumed to be uniform throughout the cell. The non-dimensional Rayleigh and Prandtl numbers at NOB conditions are defined as:

$$Ra_{NB} \equiv \frac{\alpha(T_m, p_m) g \Delta T H^3}{\nu(T_m, p_m) \kappa(T_m, p_m)}, \tag{3.9}$$

$$Pr_{NB} \equiv \frac{\nu(T_m, p_m)}{\kappa(T_m, p_m)}, \tag{3.10}$$

$$Nu_{NB} \equiv \frac{qH}{\lambda(T_m, p_m) \Delta T}., \tag{3.11}$$

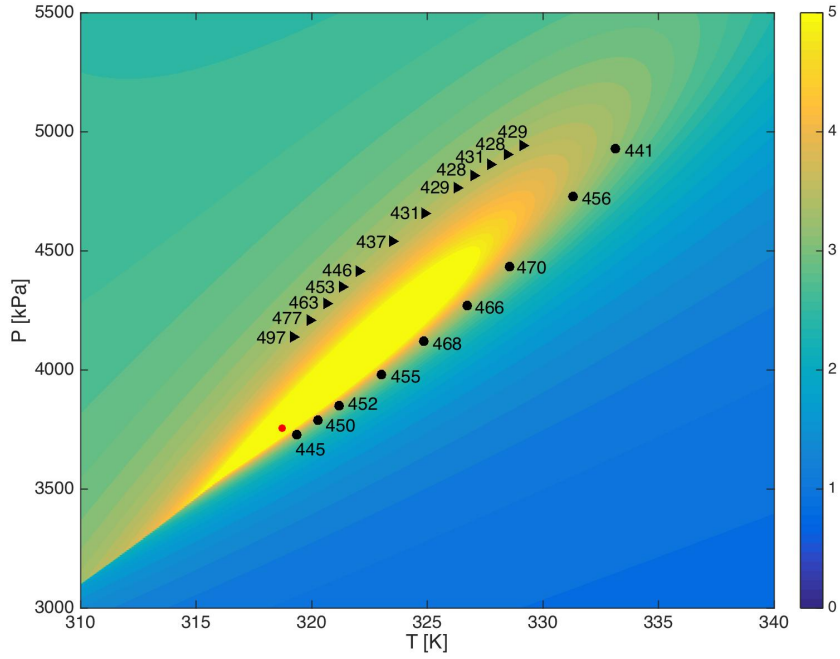


Figure 3.7: Prandtl number values (color coding) of SF_6 as a function of temperature and pressure at supercritical conditions. Red dot: Supercritical point of SF_6, black triangles: mean temperature and pressure of the experimental data of the upper branch of the iso-Prandtl curve, black circles: mean temperature and pressure of the experimental data of the lower branch of the iso-Prandtl curve. Each data point is labeled with the value of its Nusselt number. The data points are chosen on a $Pr_{NOB} = 3.5$ isoline. The fluid properties were taken from the NIST database, version 9.1 [25].

where α is the isobaric thermal expansion coefficient of the fluid, ν is the kinematic viscosity, and κ is the thermal diffusivity. The fluid properties were taken either from RefProp version 9.1 of NIST [25] or from the CoolProp database [31]. No difference between them was found for the present study.

In order to check whether also at NOB conditions the non-dimensional numbers Ra_{NOB} and Pr_{NOB} can be used to control the heat transfer expressed by Nu_{NOB}, we performed experiments at different mean temperatures and pressures, while keeping Ra_{NOB} and Pr_{NOB} constant. The points where the heat transfer was measured are represented in the temperature versus pressure plot of Figure 3.7 with black triangles and circles. The experimental conditions are also reported in the first four columns of Table 3.1, where starting from left, the values of the pressure of the cell (p_m), of the mean temperature of the cell (T_m), of the top plate temperature (T_t) and of the bottom plate temperature (T_b) are shown. The values of the mean temperature and pressure of the cell in the experiments were chosen such that the resulting Prandtl number (3.10) was $Pr_{NOB} = 3.5$. For each data point, given the mean temperature and pressure of the cell, the temperature difference (ΔT) was chosen to keep the Rayleigh number (3.9) constant in all the experiments. Its value was set at $Ra_{NOB} = 2.8 \times 10^{11}$, because it allowed to keep ΔT of the order of 1 K. For smaller ΔT the relative uncertainty on the experimental results is larger, while for larger ΔT is difficult to keep both the bottom and the top temperatures of all measurement points within the SC region.

3.4. Results

The values of the measured heat transfer through the cell (Q), together with its non-dimensionalization in the form of Nusselt number (Nu), computed with formula (3.11), are reported in Table 3.1 (columns six and seven from left).

3.4.1. General findings

By comparing the data, it can be seen that the value of the Nusselt number is not constant for all data points, but it is different from point to point. More specifically, a relative difference between the maximum and the minimum measured Nusselt number of 16% was found. This means that even though all the experiments were done at the same values of Prandtl and Rayleigh numbers, that is $Pr_{NOB} = 3.5$ and $Ra_{NOB} = 2.8 \times 10^{11}$, the Nusselt number ($Nu_{NOB}$) is not completely determined by them, as would be the case at OB conditions.

It is also interesting to note that by using the Grossmann-Lohse theory [7–9] with updated prefactors from Stevens *et al.* [32], for $Pr = 3.5$ and $Ra = 2.8 \times 10^{11}$, the Nusselt number value predicted for Oberbeck-Boussinesq conditions is $Nu = 372$. This value is 16% lower than the smallest Nusselt number measured at supercritical conditions. Therefore at supercritical conditions the heat transfer is larger than what is expected for the same Rayleigh and Prandtl numbers at Oberbeck-Boussinesq conditions.

The Nusselt numbers are also provided as labels in Figure 3.7, to allow their

Table 3.1: Text matrix of the experiments. p_m: pressure of the cell, T_m: average between top and bottom temperature of the cell, T_t: temperature of the top plate of the cell, T_b: temperature of the bottom plate of the cell, T_{PC}: pseudo-critical temperature of SF_6 at the pressure p_m; Q: measured heat transfer through the cell, Nu_{NOB}: Nusselt number corresponding to the measured heat transfer Q, Pr_{NOB} and Ra_{NOB}: Prandtl and Rayleigh numbers defined for NOB conditions as in Formulas (3.10) and (3.9), respectively, with fluid properties taken from the Coolprop Database [31].

p_m [kPa]	T_b [K]	T_t [K]	T_m [K]	T_{PC} [K]	Q [W]	Nu_{NOB}	Pr_{NOB}	Ra_{NOB}
3725.7	320.26	318.40	319.33	306.19	4.39	449	3.51	2.82E+11
3725.9	320.26	318.40	319.33	306.20	4.32	441	3.51	2.83E+11
3786	321.19	319.32	320.25	306.43	4.47	450	3.51	2.82E+11
3849	322.12	320.23	321.17	306.67	4.57	452	3.51	2.82E+11
3979	323.98	322.05	323.02	307.20	4.78	455	3.51	2.82E+11
4117	325.86	323.86	324.86	307.76	5.17	468	3.50	2.82E+11
4267.4	327.75	325.66	326.71	308.42	5.52	469	3.51	2.82E+11
4267.5	327.75	325.66	326.71	308.42	5.44	462	3.51	2.83E+11
4434	329.66	327.44	328.55	309.20	6.00	470	3.51	2.82E+11
4434	329.66	327.44	328.55	309.21	6.00	469	3.51	2.83E+11
4726	332.65	329.97	331.31	310.57	7.30	456	3.44	2.83E+11
4926	334.85	331.47	333.16	311.06	9.00	441	3.24	2.84E+11
4137	323.47	314.95	319.21	319.22	31.15	497	3.53	2.85E+11
4208	324.03	315.81	319.92	319.04	28.75	477	3.53	2.85E+11
4278	324.59	316.66	320.63	318.86	26.80	463	3.53	2.85E+11
4346	325.16	317.51	321.34	318.67	25.20	453	3.53	2.84E+11
4412	325.74	318.36	322.05	318.47	23.82	446	3.53	2.85E+11
4539	326.89	320.05	323.47	318.06	21.43	437	3.53	2.85E+11
4657	328.05	321.73	324.89	317.61	19.34	431	3.53	2.85E+11
4765	329.22	323.41	326.31	317.11	17.46	429	3.53	2.85E+11
4815	329.80	324.25	327.02	316.84	16.55	428	3.53	2.85E+11
4862	330.38	325.09	327.73	316.55	15.78	431	3.53	2.85E+11
4905	330.96	325.93	328.44	316.23	14.79	428	3.53	2.85E+11
4943	331.53	326.78	329.16	315.88	13.91	429	3.53	2.85E+11

visualization in the pressure-temperature space with respect to the critical point. All data points lay on the isoline $Pr = 3.5$, and they can be separated into two groups depending on their location. They can be located indeed either to the north (triangles) or to the south (circles) of the region with the largest Prandtl values, which to some extent is also the region where other fluid properties (e.g. specific heat capacity, kinematic viscosity and thermal conductivity) show their extremes. This makes a difference in the top-bottom symmetry of the fluid properties within the cell and in the top and bottom boundary layers. Different values of the fluid properties and of of their temperature gradients in the boundary layers will affect the global heat transfer through the cell.

3.4.2. Nusselt dependency on fluid properties-NOB effects

Since the NOB Rayleigh and Prandtl numbers are not sufficient to predict the Nusselt number of the experiments, the influence of the temperature dependency of the fluid properties within the cell should also be analyzed.

In a previous study at supercritical conditions in forced and mixed convection [33], it was seen that local thermophysical property variations can be responsible for decreased or increased turbulent motions in heated or cooled fluids at supercritical pressure. The different turbulent motion due to fluid property variations is useful to understand different heat transfer behaviors at supercritical conditions.

Figure 3.8 shows the Nusselt number plotted as a function of the relative variation of the local Rayleigh, Prandtl and Nusselt numbers between top and bottom of the cell (panels (a), (b), and (c), respectively). From Figure 3.8, panel (a), it can be seen that the relative Rayleigh number variation between top ad bottom of the cell is negative for the triangular data points (upper branch of Figure 3.7) and positive for the circular data points (lower branch of Figure 3.7). It can also be seen that for the triangular data points the Nusselt number increases when the Rayleigh number variation increases. The data points are colored accordingly to their mean temperature value. This shows that, for the triangular data points, the values of the Nusselt number increase while moving towards lower mean temperatures (and pressures as shown in fig 3.7), i.e. towards the critical point.

Such a trend is not visible for the circular data points. In this case at least two regimes can be distinguished. A first regime is for values of $0 < \frac{\Delta Ra}{Ra} < 2$, where the Nusselt number increases with the magnitude of the top-bottom Rayleigh number variation. A second regime is for values of $\frac{\Delta Ra}{Ra} > 2$, where the Nusselt number slightly decreases with the magnitude of the top-bottom Rayleigh number variation.

Similar considerations can be made by looking at the values of Nusselt number plotted as a function of the relative Prandtl number variation between the top and the bottom of the cell, plotted in panel (b). In panel (c), the Nusselt number is plotted as a function of its relative variation between its local value at the top and at the bottom of the cell. In this case, the triangular points are all condensed onto a vertical line, corresponding approximately to $\frac{\Delta Nu}{Nu} = -0.1$. The circular points are characterized by negative values of the Nusselt number top-bottom variation. They show a similar trend with respect to the ones of panels (a) and (b), but symmetric

with respect to the vertical axis. In this case the minimum of the Nusselt number is for $\frac{\Delta Nu}{Nu} = -0.1$. These trends are similar to the ones of the thermal conductivity λ plotted in panel (a) of Figure 3.9, but with opposite sign. Indeed $Nu \sim 1/\lambda$.

In Figure 3.9 the Nusselt data are plotted as a function of the relative top-bottom variation for several fluid properties. The Nusselt number dependency on the top-bottom variation of λ is plotted in panel (a), of α in panel (b), of ν in panel (c), of κ in panel (d), and of the specific heat capacity C_P in panel (g). They all show similar trends with respect to panels (a) and (b) of Figure 3.8. The Nusselt dependency on the top-bottom variation of the dynamic viscosity μ of panel (f), shows a minimum at a value slightly less than 0.4. In the Nusselt dependency on the top-bottom variation of density ρ shown in panel (e), the values of the lower branch of the data curve overlap with some of the values of the upper branch. This means that the same value of $\frac{\Delta\rho}{\rho_m}$ may correspond to two Nusselt values. It is interesting to note that the point with the minimum $\frac{\Delta\rho}{\rho_m}$ value (green circle) corresponds to the inflection point of the circular data-points as a function of all the analyzed properties (except for μ, because it is a direct function of $1/\rho$).

From the plots of Figure 3.9 it can be concluded the the upper branch of the data curve (triangles in Figure 3.7) shows a monotonic trend where the Nusselt number increases with magnitude of the top-bottom fluid property variation, for all the properties considered. The lower branch (circles in Figure 3.7) instead can be subdivided into two regimes, one where the Nusselt number increases with the top-bottom variation of the fluid properties and another one where it slightly deceases. This trend is visible for all properties, except for the density and the dynamic viscosity; the latter because it is a function of density.

3.4.3. Nusselt dependency on the mean fluid properties

Plots of the Nusselt number as a function of the fluid properties at the average top-bottom temperature of the cell, are shown in Figure 3.10. The data points indicated with triangles show an approximately monotonic trend for all properties.

Panel (f) shows the Nusselt number dependency on $C_P(T_m)$, which is non monothonic for the data points indicated with circles. In a previous study at supercritical conditions [34] it was found that that local variations of C_P cause different enthalpy and temperature profiles, in forced and mixed convection, which may influence the global heat transfer of the fluid. The fifth column of Table 3.1, reports the values of the pseudocritical temperature, T_{PC}, at the pressure of the cell for all data. T_{PC} represents the temperature where the specific heat capacity exhibits its maximum value at a given pressure, in the supercritical fluid region. From Table 3.1 it can be observed that similar values of the Nusselt number can be obtained both when T_{PC} lays within ($T_t < T_{PC} < T_b$) and outside ($T_{PC} < T_t$) the flow domain, see e.g. $Nu = 462$ and $Nu = 463$ of rows eight and fifteen. This means that it is not possible to identify C_P alone as responsible for the different trends in the Nusselt number.

From Figures 3.8, 3.9 and 3.10, it can be observed that for the data of the lower branch of the $Pr = 3.5$ isoline (circles), the slope of the Nusselt number trends changes at a temperature of approximately 327 K (indicated by the green

circle in Figures 3.8, 3.9 and 3.10).

To further investigate this change of behavior in the Nusselt number, in Figure 3.10, panels (a), (b), (c), and (d), also the values of C_P, α, ν and λ, respectively, were plotted. Figure 3.10 allows to visualize the position of the data with respect to the extremes of the considered fluid properties. Also by looking at the position of the data with respect to the maximum values of C_P, shown in panel (a), it could not be found a direct relation between them. While in a previous study a clear connection between the Nusselt number behavior and the isobaric thermal expansion coefficient, α, for ethane close to the critical point in RB-convection [35] was found, it seems not possible in this particular case to attribute changes in the Nusselt number to α only. From Figure 3.10 (c) it can be seen that the values of the kinematic viscosity, ν, are smaller for the data points of the bottom branch (circles). In particular the region with the minimum values of ν crosses the points of the lower branch at a temperature of about 330 K. This is also in the same range of temperatures where the change of the trend in the Nusselt number values was observed in Figures 3.8, 3.9 and 3.10. The thermal conductivity λ, plotted in Figure 3.10 (d), shows its maximum values towards the liquid phase (top-left corner of the figure) and also in a narrow diagonal region around and above the critical point. The latter may contribute to explain the change of the trend in Nusselt number of the data of the bottom branch of the $Pr = 3.5$ isoline.

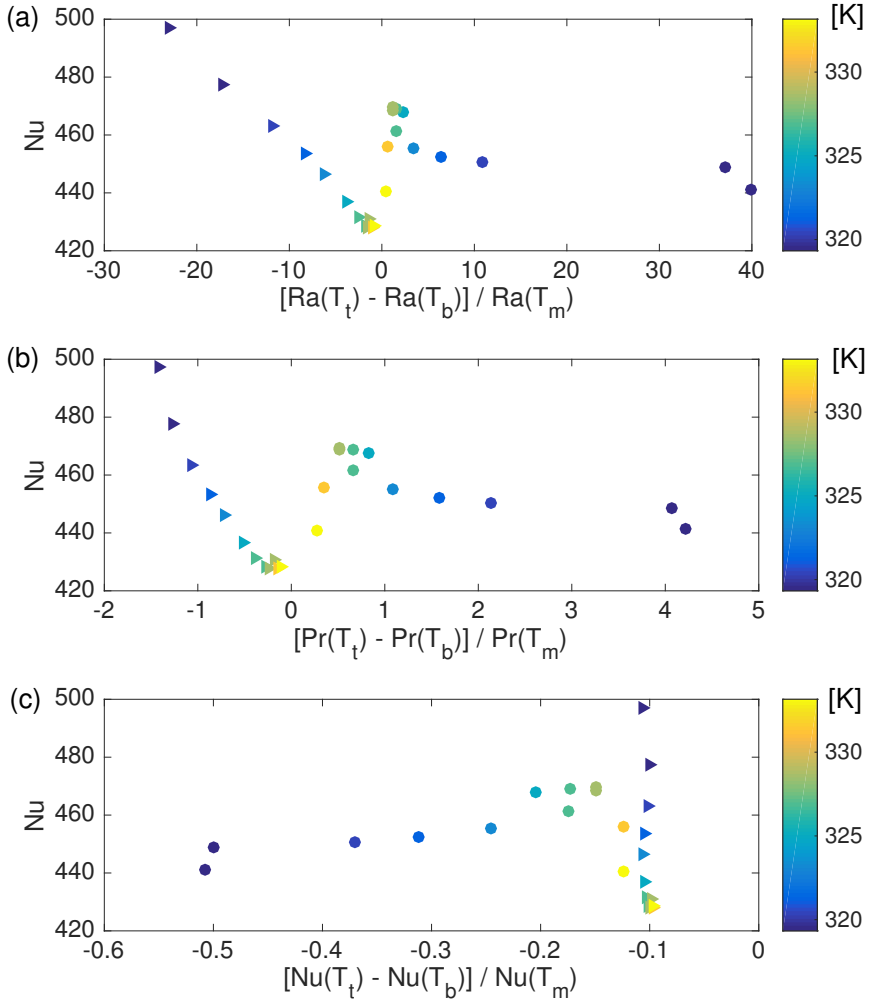


Figure 3.8: (a): Nusselt number as a function of the difference between the Rayleigh numbers calculated at the top and the bottom plate temperatures, respectively, over the Rayleigh number calculated at the mean top-bottom plate temperature (T_m). (b): Nusselt number as a function of the difference between the Prandtl numbers calculated at the top and the bottom plate temperatures over the Prandtl number calculated at (T_m). (c): Nusselt number as a function of the difference between the Nusselt numbers calculated at the top and the bottom plate temperatures over the Nusselt number calculated at (T_m). In all the panels the data are represented by triangles or circles as introduced in Figure 3.7, with color representing their temperature. All data points are at $Pr_{NOB} = 3.5$ and $Ra_{NOB} = 2.8 \times 10^{11}$. The fluid properties of SF_6 were taken from the Coolprop database [31].

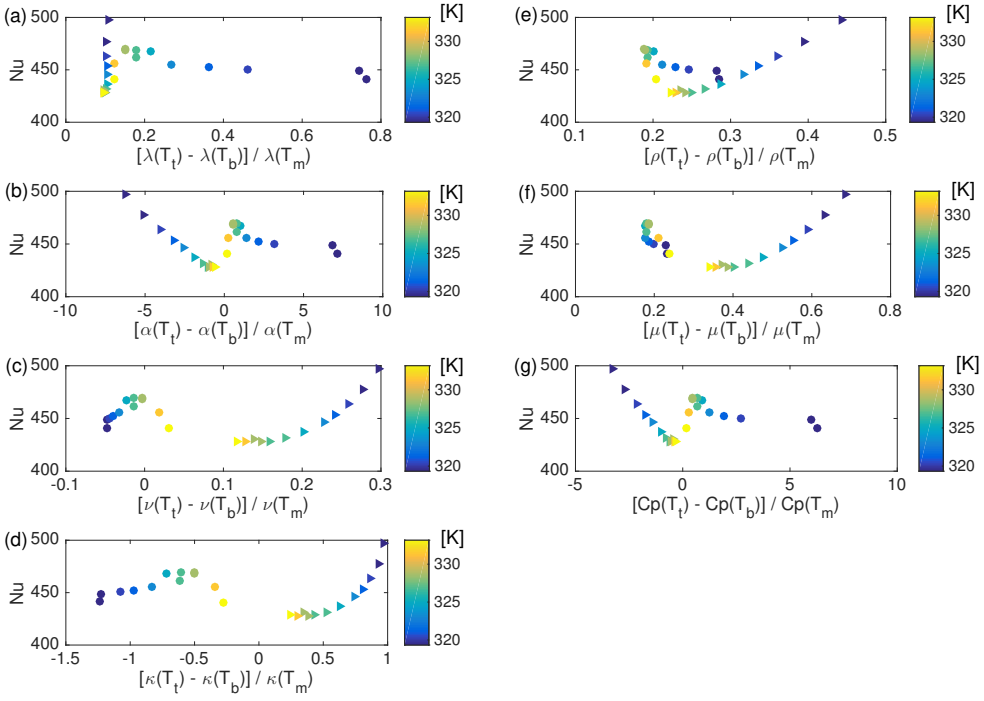


Figure 3.9: Nusselt number as a function of the temperature dependency of the fluid properties of SF_6, expressed as the difference between the top and the bottom value of the property over the property value at the average bottom-top temperature (T_m). (a), λ: thermal conductivity; (b), α: volumetric thermal expansion coefficient; (c), ν: kinematic viscosity; (d), κ: thermal diffusivity; (e), ρ: density; (f), μ: dynamic viscosity; (g), C_P: specific heat capacity. In all the panels the data are represented by triangles or circles as introduced in Figure 3.7, with color representing their temperature. All the data points are at $Pr = 3.5$ and $Ra_{NOB} = 2.8 \times 10^{11}$. The fluid properties were taken from the Coolprop database [31].

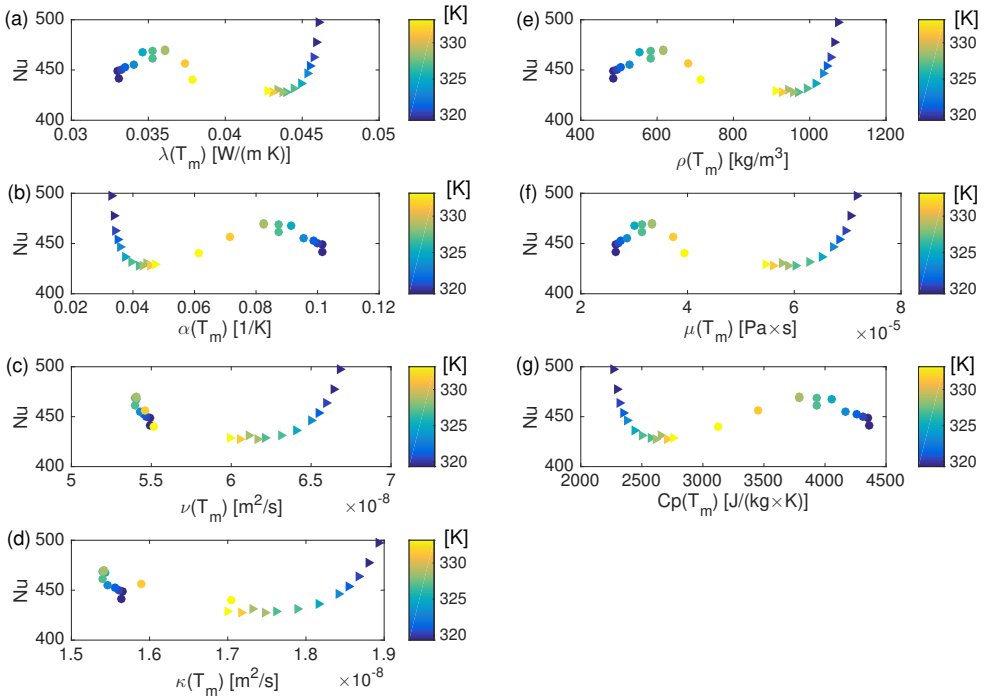
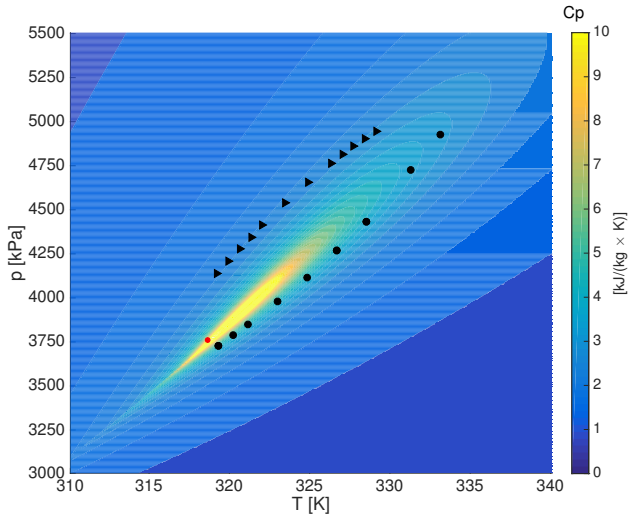
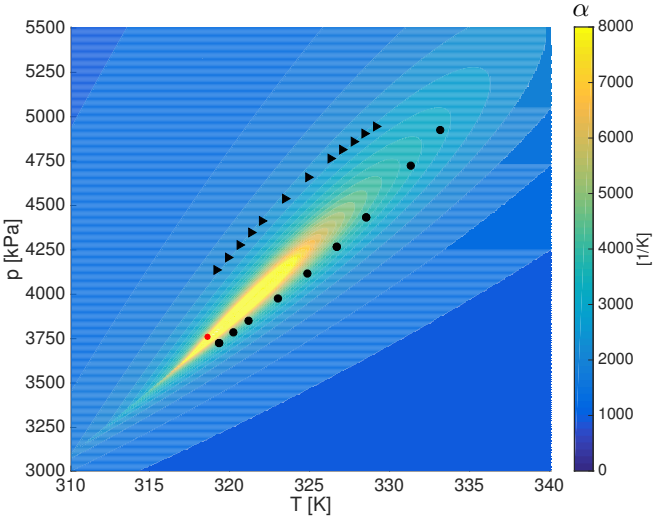


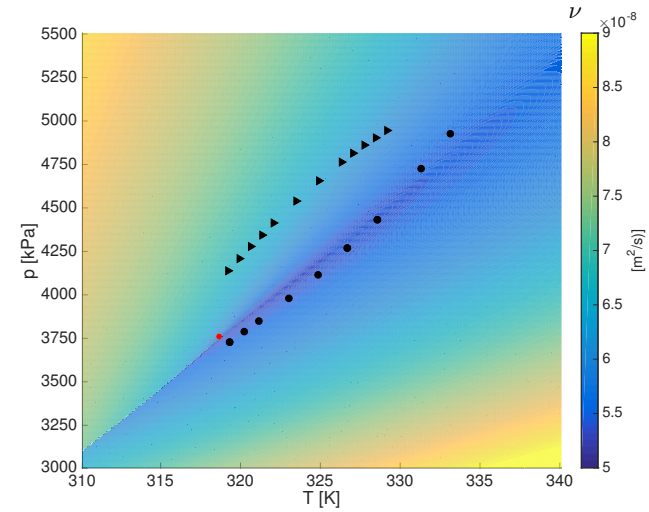
Figure 3.10: Nusselt number as a function of the fluid properties of SF_6 calculated at the top-bottom average temperature (T_m). (a), λ: thermal conductivity; (b), α: volumetric thermal expansion coefficient; (c), ν: kinematic viscosity; (d), κ: thermal diffusivity; (e), ρ: density; (f), μ: dynamic viscosity; (g), C_P: specific heat capacity. In all the panels the data are represented triangles or circles as introduced in Figure 3.7, with color representing their temperature. All the data points are at $Pr_{NOB} = 3.5$ and $Ra_{NOB} = 2.8 \times 10^{11}$. The fluid properties were taken from the Coolprop database [31].


Cp
p [kPa]
T [K]
[kJ/(kg × K)]
5500
5250
5000
4750
4500
4250
4000
3750
3500
3250
3000
310
315
320
325
330
335
340
10
9
8
7
6
5
4
3
2
1
0

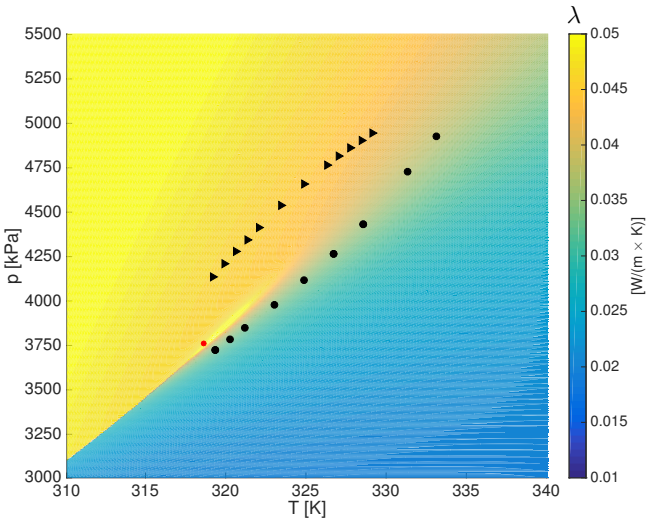
(a)


α
p [kPa]
T [K]
[1/K]
5500
5250
5000
4750
4500
4250
4000
3750
3500
3250
3000
310
315
320
325
330
335
340
8000
7000
6000
5000
4000
3000
2000
1000
0

(b)



(c)



(d)

Figure 3.10: (a) Specific heat capacity of SF_6, C_p as a function of temperature and pressure; (b) Isobaric thermal expansion coefficient, α, as a function of temperature and pressure; (c) Kinematic viscosity of SF_6, ν, as a function of temperature and pressure; (d) Thermal conductivity of SF_6, λ, as a function of temperature and pressure. Black triangles and circles: experimental data-points. Small red circle: supercritical point of SF_6. Fluid property values taken from the CoolProp database [31].

3.5. Conclusions

In this chapter the heat transfer through a Rayleigh-Bénard cell, in the supercritical fluid region was studied experimentally. The data points were chosen on the NOB-Prandtl number isoline $Pr_{NOB} = 3.5$, and the difference of temperature between the plates was set in order maintain a constant value for the NOB-Rayleigh number ($Ra_{NOB} = 2.8 \times 10^{11}$). The electrical heat input given to the bottom plate of the cell to mantain the set temperature-difference between the plates was measured, together with the temperatures of the top and bottom plates.

Results show that the heat transfer through the cell, expressed in its non-dimensional form by the Nusselt number, changes from point to point, even if all data were acquired at constant Rayleigh and Prandtl numbers. This means that, at supercritical conditions, the non-dimensional numbers, Ra_{NOB} and Pr_{NOB} are not sufficient to predict the heat transfer through the cell, as would be the case under Oberbeck-Boussinesq (OB) conditions. It was also seen that the Nusselt number at supercritical conditions is at least 16% larger than what is predicted from the Grossmann-Lohse theory at the the same non-dimensional numbers under OB conditions.

By analyzing the Nusselt number dependency on the relative top-bottom variation of the fluid properties, a common trend for almost all the fluid properties considered was found. This trend can be seen as composed of two regimes: One where the Nusselt number increases with the magnitude of the relative top-bottom variation of the fluid properties, which is the case along the upper branch of the $Pr_{NOB=3.5}$ curve (triangles in Fig. 3.7). The other regime where the Nusselt number increases with the relative top-bottom variation of the fluid properties until a specific threshold, after which it decreases. The latter regime is characteristic of the points of the lower branch of the $Pr_{NOB} = 3.5$ curve (circles in Fig. 3.7). It is not yet clear what determines this threshold value. It was not possible to identify the reason of the change of slope sign in the Nusselt number dependency on the relative top-bottom variation of the fluid properties, by looking at the Nusselt number dependency on the singular fluid properties or at groups of them that compose the non-dimensional numbers.

Further research is recommended to understand the Nusselt number dependency on the relative top-bottom difference of the fluid properties or groups of them. Velocity fields measurements can shed light into this open issue. In Chapter 5 of this Thesis, PIV velocity fields at supercritical conditions are shown to further investigate the different Nusselt number behavior between the upper and lower branch of a NOB-Prandtl isoline. Furthermore, It can be useful to perform the same kind of heat transfer experiments on a closed iso-Prandtl line, farther from the critical point. This would allow to check the Nusselt number trends in regions with smaller uncertainty of the fluid properties.

References

[1] A. Oberbeck, *Ueber die Wärmeleitung der Flüssigkeiten bei Berücksichtigung der Strömungen infolge von Temperaturdifferenzen,* Annalen der Physiks **243**, 271 (1879).

[2] J. Boussinesq, *Théorie analytique de la chaleur*, Vol. 2 (Gauthier-Villars (Paris), 1903).

[3] F. Chillà and J. Schumacher, *New perspectives in turbulent Rayleigh-Bénard convection,* The European Physical Journal E **35**, 58 (2012).

[4] G. Ahlers, S. Grossmann, and D. Lohse, *Heat transfer and large scale dynamics in turbulent Rayleigh-Bénard convection,* Reviews of Modern Physics **81**, 503 (2009).

[5] E. Bodenschatz, W. Pesch, and G. Ahlers, *Recent developments in Rayleigh-Bénard convection,* Annual Review of Fluid Mechanics **32**, 709 (2000).

[6] D. D. Gray and A. Giorgini, *The validity of the Boussinesq approximation for liquids and gases,* International Journal of Heat and Mass Transfer **19**, 545 (1976).

[7] S. Grossmann and D. Lohse, *Scaling in thermal convection: a unifying theory,* Journal of Fluid Mechanics **407**, 27 (2000).

[8] S. Grossmann and D. Lohse, *Thermal convection for large Prandtl numbers,* Physical Review Letters **86**, 3316 (2001).

[9] S. Grossmann and D. Lohse, *Prandtl and Rayleigh number dependence of the Reynolds number in turbulent thermal convection,* Physical Review E **66**, 016305 (2002).

[10] X.-Z. Wu and A. Libchaber, *Scaling relations in thermal turbulence: The aspect-ratio dependence,* Physical Review A **45** (1992).

[11] X. Xu, K. M. S. Bajaj, and G. Ahlers, *Heat Transport in Turbulent Rayleigh-Bénard Convection,* Physical Review Letters **84** (2000).

[12] G. Ahlers and X. Xu, *Prandtl-Number Dependence of Heat Transport in Turbulent Rayleigh-Bénard Convection,* Physical Review Letters **86** (2001).

[13] A. S. Fleischer and R. J. Goldstein, *High-Rayleigh-number convection of pressurized gases in a horizontal enclosure,* Journal of Fluid Mechanics **469**, 1 (2002).

[14] D. Funfschilling, E. Brown, N. Alexei, and G. Ahlers, *Heat transport by turbulent Rayleigh-Bénard convection in cylindrical samples with aspect ratio one and larger,* Journal of Fluid Mechanics **536**, 145 (2005).

[15] J. J. Niemela and K. R. Sreenivasan, *Turbulent convection at high Rayleigh numbers and aspect ratio 4,* Journal of Fluid Mechanics **557**, 411 (2006).

[16] X.-Z. Wu and A. Libchaber, *Non-Boussinesq effects in free thermal convection,* Physical Review A **43** (1991).

[17] J. Zhang, S. Childress, and A. Libchaber, *Non-Boussinesq effect: Asymmetric velocity profiles in thermal convection,* Physics of Fluids **10**, 1534 (1998).

[18] G. Ahlers, E. Brown, F. F. Araujo, D. Funfschilling, S. Grossmann, and D. Lohse, *Non-Oberbeck–Boussinesq effects in strongly turbulent Rayleigh–Bénard convection,* Journal of Fluid Mechanics **569**, 409 (2006).

[19] G. Ahlers, E. Calzavarini, F. F. Araujo, D. Funfschilling, and S. Grossmann, *Non-Oberbeck-Boussinesq effects in turbulent thermal convectionn in ethane close to the critical point,* Physical Review E **77**, 046302 (2008).

[20] S. Horn, O. Shishkina, and C. Wagner, *On non-Oberbeck–Boussinesq effects in three-dimensional Rayleigh–Bénard convection in glycerol,* Journal of Fluid Mechanics **724**, 175 (2013).

[21] S. Horn and O. Shishkina, *Rotating non-Oberbeck–Boussinesq Rayleigh–Bénard convection in water,* Physics of Fluids **26**, 055111 (2014).

[22] V. Valori, G. Elsinga, M. Rohde, M. Tummers, J. Westerweel, and T. van der Hagen, *Experimental velocity study of non-Boussinesq Rayleigh-Bénard convection,* Physical Review E **95**, 053113 (2017).

[23] L. Prandtl, *Über Flüssigkeitsbewegung bei sehr kleiner Reibung* (Leipzig: Teubner, 1905) pp. 484–491.

[24] H. Blasius, *Grenzschichten in Flüssigkeiten mit kleiner Reibung,* Z. Math. Phys. **56**, 1 (1908).

[25] E. Lemmon, M. Huber, and M. McLinden, *NIST reference database 23: reference fluid thermodynamic and transport properties-REFPROP, version 9.1,* Standard Reference Data Program (2013).

[26] J. Jackson, *Fluid flow and convective heat transfer to fluids at supercritical pressure,* Nuclear Engineering and Design **264**, 24 (2013).

[27] J. Y. Yoo, *The turbulent flows of supercritical fluids with heat transfer,* Annual Review of Fluid Mechanics **45**, 495 (2013).

[28] S. Gupta, E. Saltanov, S. J. Mokry, I. Pioro, L. Trevanib, and D. McGillivray, *Developing empirical heat-transfer correlations for supercritical co2 flowing in vertical bare tubes,* Nuclear Engineering and Design **261**, 116 (2013).

[29] D. Huang, Z. Wub, B. Sunden, and W. Li, *A brief review on convection heat transfer of fluids at supercritical pressures in tubes and the recent progress,* Applied Energy **162**, 494 (2016).

[30] *EuHIT,* (2017).

[31] I. H. Bell, J. Wronski, S. Quoilin, and V. Lemort, *Pure and pseudo-pure fluid thermophysical property evaluation and the open-source thermophysical property library coolprop,* Industrial & Engineering Chemistry Research **53**, 2498 (2014).

[32] R. J. Stevens, E. P. van der Poel, S. Grossmann, and D. Lohse, *The unifying theory of scaling in thermal convection: the updated prefactors,* Journal of Fluid Mechanics **730**, 295 (2013).

[33] J. W. R. Peeters, R. Pecnik, M. Rohde, T. H. J. J. van der Hagen, and B. J. Boersma, *Turbulence attenuation in simultaneously heated and cooled annular fows at supercritical pressure,* Journal of Fluid Mechanics **799**, 505 (2016).

[34] J. W. R. Peeters, R. Pecnik, M. Rohde, T. H. J. J. van der Hagen, and B. J. Boersma, *Characteristics of turbulent heat transfer in an annulus at supercritical pressure,* Physical Review Fluids **2**, 024602(24) (2017).

[35] G. Ahlers, F. F. Araujo, D. Funfschilling, S. Grossmann, and D. Lohse, *Non-Oberbeck-Boussinesq Effects in Gaseous Rayleigh-Bénard Convection,* Physical Review Letters **98**, 054501 (2007).

4

Design and commissioning tests of a high-pressure facility with optical access

4.1. Introduction

High-pressure set-ups with good optical-access are very rare, even though visualizing high-pressure fluids is quite relevant. High-pressure fluids can be used for example to enlarge and bring to an extreme the parametric conditions of an experiment while keeping its geometry compact, by operating with different thermophysical fluid-properties. For example, in natural convection, the density of many fluids and their Rayleigh number can be increased by operating at high pressure, without need to make the height of the convection cell larger [1–3]. High-pressure set-ups also allow the study of phenomena that happen at high pressure for many fluids, like the effect of a strong temperature-dependency of the fluid properties around and above their critical point [2, 4–8]. This is interesting both from a fundamental and from an industrial point of view, as explained in the introduction of this thesis (Chapter 1). High-pressure fluids can be used as cooling fluids in power plants (coal-fueled and nuclear power-plants) for a more efficient energy-production. As already described in Chapter 1, the Supercritical Water Reactor is a new concept of nuclear reactor cooled by water above its gas-liquid critical point [9–12]. A particular application of SC fluids to nuclear PPs, which is currently under research, is as heat exchangers for heat-recovery systems (sCO2 He-Ro project) [13]. Here supercritical CO_2 is used in a heat-removal system as a cooling system, for accident conditions, removing the decay heat of the nuclear fuel. Such a cooling backup-system can be applied both in current and in future boiling-water reactors and pressurized-water reactors.

Depending on the kind of visualization technique that is used to study the flow, such as laser-Doppler velocimetry (LDV), particle-image velocimetry (PIV) or

background-oriented schlieren (BOS), one or more optical-windows may be necessary in the set-up. For the present study, planar PIV and BOS were used and, therefore, three optical-windows were needed.

This chapter concerns with the design and the commissioning tests of a high-pressure facility working with Trifluoromethane (R-23) above its gas-liquid critical point. This facility was built with the aim to perform a feasibility study to demonstrate the applicability of PIV to thermally-convective supercritical-fluids. At the Reactor Institute of Delft University of Technology, where this facility was developed, previous experimental works with supercritical R-23 were already performed. They include studies on the stability of a supercritical-water circuit [14, 15]. To make them, a facility operating with supercritical R-23 was built, initially without optical access. It was subsequently modified to allow optical access through one window for LDV measurements. The technical expertise acquired from these previous studies, for example in terms of materials, instrumentation and control of a high-pressure facility, was used in the present work.

The biggest challenge of the present study was not just to design and perform the commissioning tests of a high-pressure facility (Rayleigh-Bénard cell) with good optical-accesses, but mainly to test whether the PIV technique works at supercritical conditions. The feasibility of PIV measurements at supercritical conditions is presented in the next chapter (Chapter 5), while this chapter is fully dedicated to a description of the design criteria and the commissioning tests of the high-pressure facility where the PIV measurements were performed.

4.2. Facility description, design criteria and working instructions

The experimental facility used for the high-pressure experiments is composed of a Rayleigh-Bénard (RB) cell, inserted in a high-pressure circuit and two water loops at lower pressure, which provide and subtract heat to/from the RB cell. A schematic of the set-up is shown in Figure 4.1. The fluid in the high-pressure circuit is Trifluoromethane (molecular formula: CHF_3, ASHRAE Number: R-23 [16]). It was chosen because of its experimentally accessible critical point (i.e. 48 bars or 4.8 MPa, at about 26°C or about 299 K [17]). This circuit is kept under pressure mechanically by a piston (Parker Series 5000 piston accumulator). The cylinder that contains the piston for the pressure regulation is filled on one side with trifluoromethane and on the other side with compressed air. The position of the piston inside the cylinder is electromagnetically measured. The pressure of the set-up can be regulated from 1 bar up to 70 bars. When it is needed to increase the pressure in the set-up, compressed air from a 200 bars (20 MPa) air bottle is led into the cylinder, and the piston moves down compressing the freon in the other side of the cylinder. When instead a lower pressure is needed in the circuit, air is released from the top of the piston. This decreases the pressure on the air side of the cylinder and allows the piston to move to increase the system volume on the freon side in order to reduce the pressure of the freon. The Rayleigh-Bénard (RB) cell is connected to the high-pressure circuit through a single pipe. This connecting pipe allows the

fluid to go in and out of the cell. Fluid flows into the cell during the filling of the facility or when it contracts due to temperature changes, while fluid flows out of the cell when emptying the facility or when the fluid expands. The RB cell is heated and cooled by two water circuits, one at the bottom of the cell and the other one at the top. More details about the heat exchangers and the cell are given in Section 4.3. Before filling the cell with freon, the air inside the circuit is drawn out by a vacuum pump, which is connected to the cell instead of the pressure regulator piston. More details about this procedure are given in the Appendix.

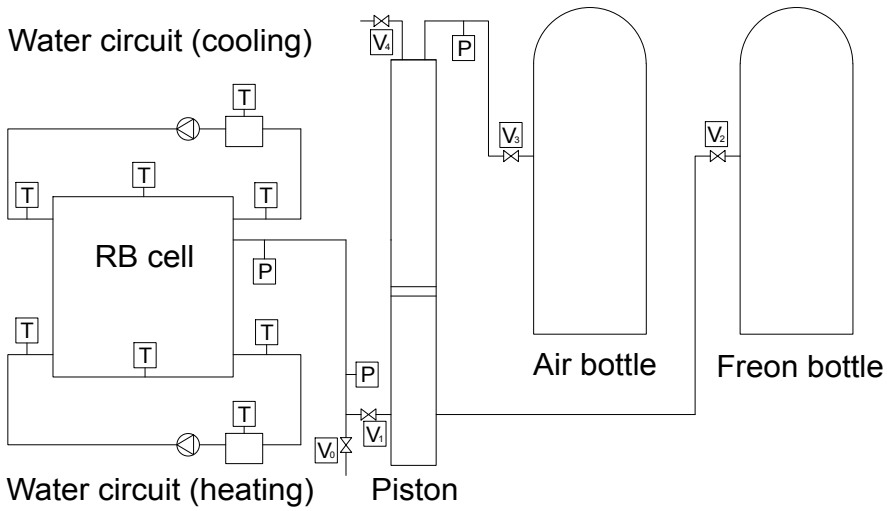


Figure 4.1: Sketch of the experimental facility. The Rayleigh-Bénard cell with the two water heating and cooling circuits is represented, together with the freon circuit. The latter comprises of the freon bottle, one side of the piston for pressure regulation, and the cell. The air circuit comprises of the air bottle and the other side of the piston regulator. Boxes with T indicate the locations of thermistors, boxes with P the locations of pressure sensors, and boxes with V the locations of valves.

4.2.1. Pressure and temperature sensors and LabView control

Pressure measurements

In the high-pressure circuit there are three pressure-transducers: one close to the inlet of the RB cell, one at the outlet of the piston on the freon side, and another one at the inlet of the piston on the pressurized-air side, as shown in Figure 4.1, where they are indicated with a ”P”. The pressure sensor close to the cell is a

PTX 510 Industrial Pressure Transmitter, with a range from 1.5 through 10,000 psi (0.1 through 68.9 MPa) and with an accuracy of ±0.15% in the full scale. At the pressure of the experiments, about 60 bar, the maximum uncertainty in the pressure value is 0.09 bar. The two pressure-sensors at the air and at the freon side of the pressure-regulator piston are HPS-A Series 4-20 mA Output Pressure Transmitter with a range from 0 to 100 bar (0 to 10 MPa).

Temperature measurements

In each one of the two low-pressure water-circuits there are four thermocouples. For each water circuit: one thermocouple is in the copper plate of the RB cell, as shown in Figures 4.1 and 4.4, another two are at the inlet an the outlet of the copper plates of the RB cell respectively, immersed in the cooling/heating water, and one is in a reservoir tank from which the water is pumped (see Figure 4.1). The thermocouples are LABFACILITY type k, class 2, mineral insulated sensors. They were calibrated against two temperatures (triple point, 0 °C and boiling water, 100 °C at standard atmospheric-pressure) and have a maximum tolerance of ±0.3 K.

The thermocouple in each copper plate is the reference thermocouple used in the experiments to indicate the temperature of the plate. They can be extracted from their position independently from other components of the set-up, with special Swagelok connections for high-pressure applications (see Figure 4.2 for the top plate thermocouple), i.e. without opening the flanges of the cell or the connections with the water cooling/heating circuits. For this reason, the hole for the location of the thermocouple tip had to be quite large (about 2 mm in diameter), which is larger than the thermocouple tip. Therefore, to guarantee a good contact between the thermocouple tip and the hole in the copper plate, copper was added to the thermocouple tip, and a ceramic paste was put on its surface every time the thermocouple was inserted in its working position. The paste was chosen to be both highly thermally-conductive and inert to supercritical freon R-23. This paste is called ”Céramic Premium High-Density Thermal Compound”, and it is produced by ”Arctic Silver”.

LabVIEW control

The measured values of the pressure and the temperature sensors of the facility and the position of the pressure-regulator piston are read and recorded through a LabVIEW program (National Instruments, version 2012) with two cards, one for the pressure sensors (NI PCI-6036E) and another one for the thermocouples and the pressure-regulator piston (NI cDAQ-9171). This program and cards are used to set the temperatures of the water in the two reservoirs for the cooling and heating of the copper plates of the cell. In each reservoir tank there is an electrical heater and also a cooling circuit to regulate the temperature of the water to the desired value. The mass flow-rate of the cooling circuit in the water tank is regulated manually by a valve, while its temperature remains fixed. The electrical heater in each tank is controlled by the LabVIEW program on the base of the desired temperature. A PID (Proportional Integrative Derivative) control minimizes the error between the desired temperature and the measured temperature in the reservoir by adjusting the electric power given to the heater in the reservoir. The parameters used by the

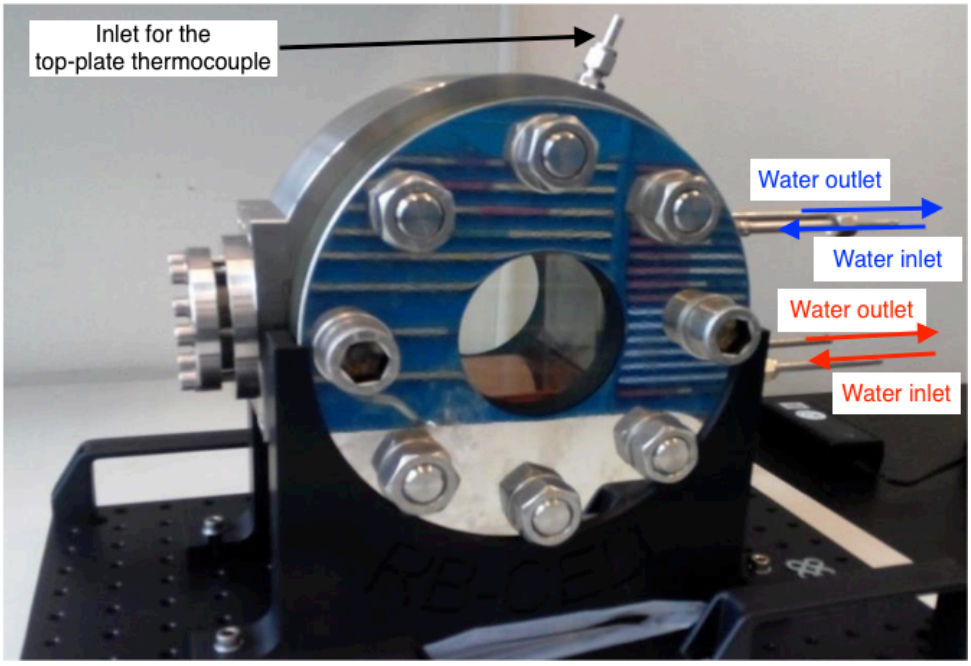


Figure 4.2: Picture of the high-pressure RB cell. The connection for the inlet of the top-plate thermocouple is shown. The inlet and outlet pipes for the cooling/heating water of the top/bottom plates are also shown.

program are reported in Table 4.1. The same parameters are applied to both water circuits.

Table 4.1: Parameters of the PID temperature control in the LabVIEW program. K_c: proportional control coefficient, τ_i: integral time constant, τ_d: derivative time constant.

K_c	τ_i [s]	τ_d [s]
1	3	0.003

4.3. Rayleigh-Bénard cell

The high-pressure Rayleigh-Bénard (RB) cell is composed of a cube with two horizontal copper-plates and four glass lateral-walls. This cube is inserted inside a stainless-steel cylinder with three sight-glass flanges made of borosilicate to allow optical access to the flow. A drawing of the RB cubical cell is shown in Figure 4.3, while the high-pressure facility is shown in Figures 4.2 and 4.4. The

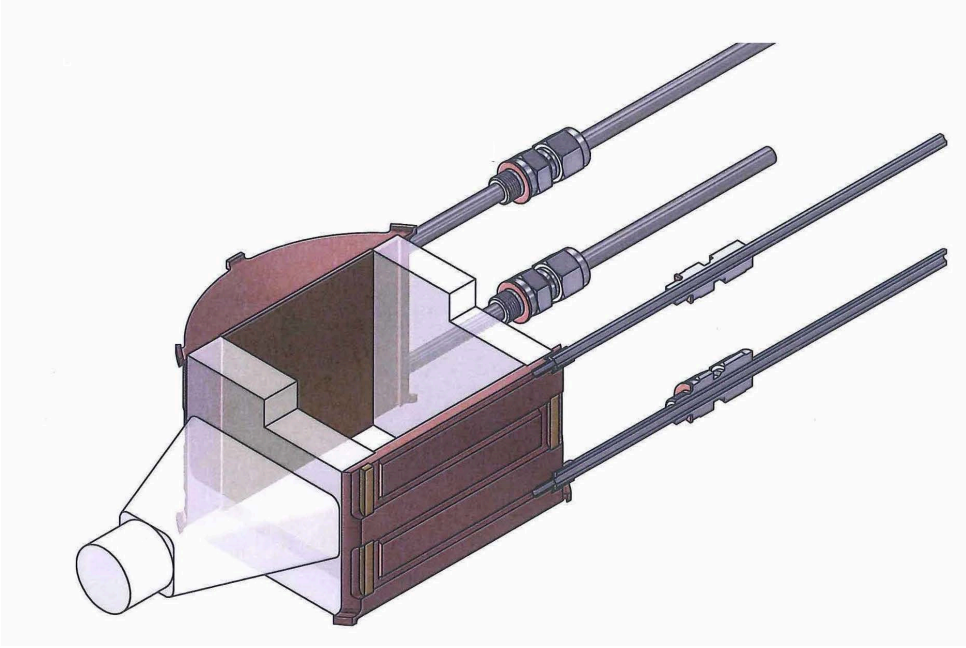


Figure 4.3: Internal part of the Rayleigh-Bénard high-pressure convection cell. The two horizontal copper-plates with heating and cooling circuits and two glass lateral-walls are shown. Next to one glass lateral-wall, there is a glass with a pyramid shape, to guide the laser sheet into the measurement section.

internal dimension of the cube shown in Figure 4.3 is 70 mm. This value is the result of an optimization between the spatial resolution of the PIV measurements (see Chapter 5) and technical constrains due to the high operative-pressure of the

set-up. A larger size of the cube would require in fact more stainless-steel volume around it to hold the high operative-pressure. The actual RB set-up weight is about 60 kg. An heavier cell would be extremely difficult to manage when it needs to be turned and opened for the insertion of the PIV tracer-particles, for example. The cube shown in Figure 4.3 has two glass lateral-walls that are 10 mm thick. This thickness value is the result of an optimization between technical-construction constrains and having as much as possible equal thermal conditions at the side walls of the cube. The other two walls of the cube are made by quartz that holds high pressure, and it is 20 mm thick. One of the two lateral glass-walls of Figure 4.3 is a simple parallelepiped. The opposite one is also a parallelepiped that is in contact with a pyramid-shaped glass, which is used to guide the laser sheet straight to the cell. This glass guide fills in the space between the borosilicate window and the glass wall of the measurement section. It does not allow particles that went out the measurement domain to go in front of the laser sheet. The surfaces of the glass walls and pyramid are polished according to optical standards to minimize losses of light intensity at the interfaces. The thickness of the pyramid-shaped glass is 10 mm. This allows to regulate the laser-sheet thickness as desired. The other two glass lateral-walls of the RB cell (shown in Figure 4.4) are made of a special borosilicate for high-pressure applications: METAGLAS® Sight Glass Flange, Connection to DIN 2501 - Type 11. In these flanges the sight glass is fused to the metal (stainless steel) conforming to DIN 7079.

As can be seen in Figure 4.3, inside each copper plate, a conduct for water was made. These two conducts are included in two low-pressure water-circuits (see Figure 4.1) and provide the heat exchange to the RB cell. The diameter of the circular section of the conducts that run through the copper plates is 2 mm, and it was chosen to guarantee a sufficient surface for the heat exchange between water and copper, while keeping the safety structural limits of the facility at operational conditions (working pressure up to 70 bars). An estimate of the cooling-power needed for the Rayleigh number of the experiments was taken from [18] and multiplied by a factor 10 to take into account possible increases due to the non-Boussinesq conditions that occur in the present work. The flow rate of the water in the cooling and heating circuit was chosen to keep the difference in water temperature between entering and leaving the plate within 0.6 K, being of the order of the uncertainty range of the thermocouples.

For insulation purposes, the copper plates are not in direct contact with the stainless steel, but there is a gap between them as shown in Figure 4.4. This gap is filled with an insulator material, which is a kind of plastic that does not react with the supercritical freon R-23 used. The insulator material is polyetheretherketone, DIN-abbreviation: PEEK. Its average thickness is 2.5 mm and its thermal conductivity at 23°C is 0.25 W/(m K). The PEEK insulator thermal conductivity is three order of magnitude smaller than the thermal conductivity of the copper plate, which is about 401 W/(m K) at 20°C and two orders of magnitude smaller than the stainless steel, which is about 16 W/(m K) at 25°C. This material was chosen both because of its thermal-insulation characteristics and because of chemical compatibility with

supercritical-freon R-23.

A very delicate part of the design of the copper plates was their connection with the water-cooling pipes. This connection (shown in Figures 4.3 and 4.5) allows the low-pressure water-circuit to enter the high-pressure stainless-steel cylinder first and then the copper plates. It is a delicate part because it should withstand the difference in pressure between the high-pressure freon and the low-pressure water circuit (up to 70 bars) and be flexible enough to allow mobility of the copper plates. The internal structure of the cell is indeed very delicate, due to the two lateral-glass-walls of the cube (the internal ones made by simple glass shown in Figure 4.3) and of the pyramid-shaped glass that guides the laser-sheet into the cubical measurement-domain. These internal glass-components are meant only for optical access, and they are not supposed to hold any pressure. During the commissioning tests of the facility this glass structure broke, because there was not enough flexibility when the cell was put under pressure. During pressurization, some flexibility is needed to avoid tension on the fragile internal glass-walls. This problem was solved by using a flexible pipe that connects the low-pressure water-circuit to the copper plates (see Figure 4.5) and allows them to move if necessary. As shown in Figures 4.3 and 4.4, the flexible pipe is connected to the copper plate that may need to move and to the rigid external stainless-steel-structure, allowing flexibility to the system.

Table 4.2 summarizes the operative pressure and temperature of the facility.

Table 4.2: Operative conditions of the Rayleigh-Bénard facility. T_{max} and T_{min} are the maximum and minimum temperatures that can be reached in the copper plates of the cell, while P_{max} and P_{min} are the maximum and minimum operative pressures of the facility.

$P_{max}[bar]$	$P_{min}[bar]$	$T_{max}[°C]$	$T_{min}[°C]$
60	0.1	70	20

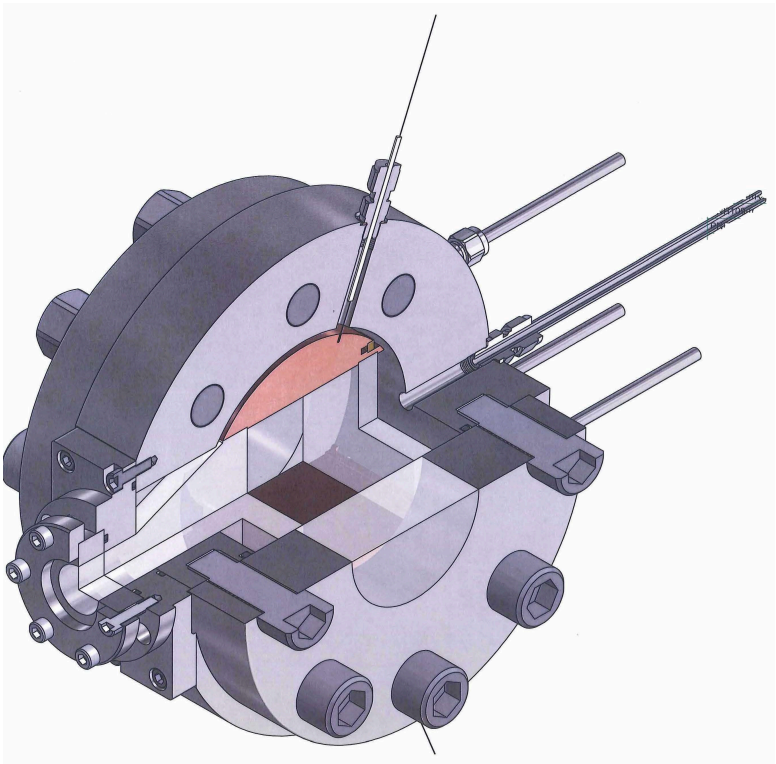


Figure 4.4: Picture of the whole Rayleigh-Bénard high-pressure convection-cell.

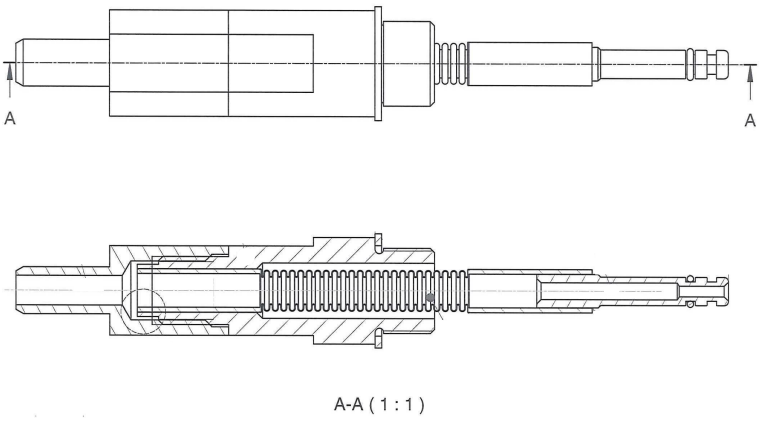


Figure 4.5: Flexible-pipe connection between the water circuit and the copper plates. This connection is inserted in the copper-plate conduct and in the stainless-steel external-structure. Its flexible part allows the copper plate to move, while the flexible-pipe connection is externally fixed to the stainless steel.

4.4. Summary

A set-up to study Rayleigh-Bénard convection of a supercritical fluid with optical access was designed, built and put in operation. The result of this work allows the study of a Rayleigh-Bénard flow at supercritical conditions, with optical visualization of the fluid-flow velocities. This is the first set-up designed for PIV measurements of a supercritical fluid and also the first Rayleigh-Bénard cell designed for PIV of a supercritical fluid. It can operate with working pressures up to 70 bar and temperatures of the plates from 20 to 70°C. It allows to experimentally study the velocity fields of supercritical fluids in thermal convection. The visualization of velocity fields of a supercritical fluid in Rayleigh-Bénard convection is the starting step for a better understanding of the fluid mechanics of supercritical fluids. These fluids can be used for a more efficient cooling of fossil and nuclear-cooled power-plants for electrical-energy production.

Appendix

Before filling the facility with freon, the air present in the facility should be removed by a vacuum pump. The pump can be connected to the bottom part of the set-up at the outlet of the pressure-regulator cylinder on the freon side (see Figure 4.1). This can be done by closing valve 1 (V_1) and opening valve 0 (V_0).

Filling procedure

When the facility is empty, the high-pressure circuit can be connected to the freon bottle, by opening valve V_1 and valve V_2. The heat exchangers of the cell should be off during the entire filling and emptying procedure. The high-pressure freon-bottle is at about 23 bar. It has two openings at the top: one on the gas side and another one on the liquid side. To fill the facility, it is convenient to first connect it to the gas side of the freon bottle with a pressure reducer built in between. This allows the user to gradually increase the pressure in the facility. The Rayleigh-Bénard cell is very delicate because of its glass internal-structure so that a sudden difference of pressure between two sides of a glass wall may actually break it. When the pressure in the facility is about 22 bar, gas freon does not flow anymore from the bottle to the cylinder, because its pressure is approximately equal on both sides. It is then convenient to change the connection of the facility from the gas side to the liquid side of the freon bottle and remove the pressure reducer. The pressure of the facility can then be increased up to the pressure of the freon bottle. To further increase the pressure it is necessary to use the pressure-regulator piston (see Figure 4.1) and follow these instructions:

1. close the connection valve between the freon bottle and the facility, V_2;
2. open the connection valve between the pressurized-air bottle (up to 200 bar) and the pressure-regulator piston, V_3;
3. open the connection valve between the freon side of the piston and the facility, V_1;
4. increase the pressure on the air side of the piston, by a valve-controlled air-flow from the pressurized-air bottle to the piston. In this way also the pressure in the facility increases;
5. when the piston reaches its lowest position, the freon cannot be compressed further, and the air flow can be stopped, by closing valve V_3;
6. close the connection between the facility and the piston, valve V_1
7. open the valve at the top of the cylinder, V_4 and release air until the pressure in the air side of the cylinder is about 1 bar;
8. at this stage the pressure on the freon side of the cylinder is less than the pressure in the freon bottle, and valve V_2 can be opened to allow freon to flow from the bottle to the facility;

9. when the piston is at its highest position, no freon can flow into the cylinder anymore, and valve V_2 can be closed;

10. close valve V_4 to avoid air from flowing out;

11. open valve V_1 and valve V_3 and leave air flow into the cylinder, by controlling the flow through the aperture of the valve. The pressure in the facility increases;

12. when the pressure in the facility reaches its desired value, valve V_2 can be closed; otherwise leave valve V_2 open until the piston in the cylinder is at its lowest position;

13. to increase the pressure further repeat the procedure from the beginning and remember that the facility can be operated with a maximum of 70 bars; above this limit a safety valve opens, and freon is released from the facility.

Procedure for emptying the facility

1. open valve V_1

2. open valve V_4 and release air until the piston is at its highest position in the cylinder, and the air pressure on the air side of the piston is about 1 bar (air can no longer flow out);

3. close valve V_2 and open valve V_2 to let freon flows back into the bottle;

4. when the freon pressure in the cylinder equals the pressure of the freon bottle, close valve V_2;

5. close valve V_1, open valve V_3 and leave air flow into the cylinder until the piston is at its lowest position;

6. close valve V_3 and open valve V_2. Since the pressure of the freon in the cylinder is higher the pressure of the freon in the bottle, fluid flows back into the bottle;

7. when the pressure of the freon in the cylinder equals the pressure of the freon bottle, close valve V_2;

8. open valve V_4 and release air from the piston;

9. open valve V_1 and gradually release pressure from the facility;

10. repeat the procedure until the pressure in the facility is about 1.3 bar; then valve V_0 can be opened, and also the facility can be opened.

References

[1] X. Chavanne, F. Chillà, B. Castaing, B. Hébral, B. Chabaud, and J. Chaussy, *Observation of the Ultimate Regime in Rayleigh-Bénard Convection,* Physical Review Letters **79**, 3648(4) (1997).

[2] S. Ashkenazi and V. Steinberg, *High Rayleigh Number Turbulent Convection in a Gas near the Gas-Liquid Critical Point,* Physical Review Letters **83** (1999).

[3] J. R. de Bruyn, E. Bodenschatz, S. W. Morris, S. P. Trainoff, Y. Hu, D. S. Cannell, and G. Ahlers, *Apparatus for the study of Rayleigh-Bénard convection in gases under pressure,* Review of Scientific Instruments **67** (1996).

[4] Y. Burnishev, E. Segre, and V. Steinberg, *Strong symmetrical non-Oberbeck-Boussinesq turbulent convection and the role of compressibility,* Physics of Fluids **22**, 035108 (2010).

[5] Y. Burnishev and V. Steinberg, *Statistics and scaling properties of temperature field in symmetrical non-Oberbeck-Boussinesq turbulent convection,* Physics of Fluids **24**, 045102 (2012).

[6] J.-Q. Zhong, D. Funfschilling, and G. Ahlers, *Enhanced Heat Transport by Turbulent Two-Phase Rayleigh-Bénard Convection,* Physical Review Letters **102**, 124501 (2009).

[7] M. Assenheimer and V. Steinberg, *Rayleigh-Bénard Convection near the Gas-Liquid Critical Point,* Physical Review Letters **70**, 3888 (1993).

[8] X.-Z. Wu and A. Libchaber, *Non-Boussinesq effects in free thermal convection,* Physical Review A **43** (1991).

[9] J. Y. Yoo, *The turbulent flows of supercritical fluids with heat transfer,* Annual Review of Fluid Mechanics **45**, 495 (2013).

[10] I. Pioro and P. Kirillov, *Current status of electricity generation in the world*, edited by A. Méndez-Vilas, Vol. Materials and processes for energy: communicating current research and technological developments (A. Méndez-Vilas, 2013).

[11] I. L. Pioro and B. Romney, *Handbook of Generation IV Nuclear Reactors*, edited by I. L. Pioro, Woodhead Publishing Series in Energy (Woodhead Publishing, 2016).

[12] I. Pioro, *Nuclear Power as a Basis for Future Electricity Production in the World: Generation III and IV Reactors* (2012).

[13] sCO2-HeRo Project, (2017).

[14] M. Rohde, C. Marcel, C. T'Joen, A. Class, and T. van der Hagen, *Experimental study of the coupled thermo-hydraulic–neutronic stability of a natural circulation HPLWR,* International Journal of Heat and Mass Transfer **54**, 65 (2011).

[15] C. T'Joen and M. Rohde, *Experimental study of the coupled thermo-hydraulic-neutronic stability of a natural circulation HPLWR,* Nuclear Engineering and Design **242**, 221 (2012).

[16] R. American Society of Heating and A.-C. Engineers, *https://www.ashrae.org,* (2017).

[17] E. Lemmon, M. Huber, and M. McLinden, *NIST reference database 23: reference fluid thermodynamic and transport properties-REFPROP, version 9.1,* Standard Reference Data Program (2013).

[18] J. J. Niemela, L. Skrbek, K. R. Sreenivasan, and R. J. Donnelly, *Turbulent convection at very high Rayleigh numbers,* Nature **404**, 837 (2000).

5

PIV measurements of a Rayleigh-Bénard flow in a supercritical fluid

5.1. Introduction

The design, construction and commissioning tests of a high-pressure convection cell with optical access, presented in Chapter 4, were the first steps to perform experiments at supercritical fluid conditions. To the knowledge of the author, PIV measurements have never been done previously at supercritical conditions, and only two previous velocity studies with optical measurements (laser Doppler velocimetry) near or above the critical point were previously reported, but for very particular conditions. In the study by Ashkenazi and Steinberg [1], the temperature gradient between the two horizontal plates of their thermal convection system was kept of the order of 10^{-3} K, in order to maintain Boussinesq conditions for the working fluid [2]. In the other study, performed by Licht *et al.* [3], the measurements were done in a square annulus, with forced and mixed convection. In the latter case a correction in the experimental results was made with a ray-tracing program to take into account the radial variation in the index of refraction of the fluid.

In this chapter the applicability of the PIV technique in supercritical fluids was tested, since strong optical distortion can occur due to a strong variation of the index of refraction of the fluid, especially near the critical point of the fluid. The aim of this test was to investigate how strong changes in the local properties of the fluid influence the flow structures and the heat transfer in natural convection. Strong optical distortions, due to strong changes of thermo-physical properties, and more specifically due to sharp density changes and associated fluid refractive index changes, make it difficult to perform PIV measurements for several reasons. One is that due to the strong density changes within the flow domain, the particles may

not be able to follow the flow or to remain suspended in the flow at all. Because of density changes also the number of the particles within the measurement domain may not be sufficiently high or uniform as desired for PIV measurements. Other reasons are due to blur and errors in measured the position of the particles and in their velocity, as shown by Elsinga *et al.* [4]. In this study a method was developed to quantify and correct for PIV errors due to refractive index changes in 2D compressible flows with a stationary and smoothly varying density distribution. They show by PIV recordings, BOS (background-oriented schlieren) measurements, and numerical simulations that the second derivative of the refractive index is the mayor source of velocity errors. PIV studies in fluids with strong localized changes in the refractive index were performed in compressible flows by Murphy *et al.* [5] and by Elsinga et al. [6]. Murphy et al. [5] developed a high speed PIV system to study blast waves. Elsinga *et al.* [6] performed PTV (particle tracking velocimetry) and PIV measurements together with light-ray tracing predictions and found that optical errors in the velocity measurements of shock waves depend strongly on the viewing angle between the viewing direction and the plane of the shock.

Some background information about the PIV and the BOS (background oriented schlieren) techniques and the challenges of using optical measurements with a supercritical fluid are provided in Sections 5.2, 5.3 and 5.5. The approach used for the PIV feasibility study at supercritical conditions consisted first in an optical distortions study (paragraph 5.8.1) to know whether the optical distortions allowed to see the particles and to adequately estimate their position and velocity [4]. This part was done with the BOS technique. After that, PIV measurements at supercritical fluid conditions (paragraph 5.8.6) and an estimation of the statistical measurement uncertainty were made (paragraph 5.8.4). Finally, a general method to estimate the uncertainty of the PIV cross-correlation algorithm for the unconventional conditions of a supercritical fluid was applied. It was found that at supercritical conditions, as is the case at sub-critical conditions, the large scale flow structure is organized in one big roll. This roll differs with respect to the one at sub-critical conditions, because of its strong asymmetries and its complex inner structure.

5.2. Basic information on particle image velocimetry

A thorough description of the PIV technique can be found in the reviews by Westerweel *et al.* [7] and by Adrian [8], and in the books by Adrian and Westerweel [9] and by Raffael *et al.* [10]. In the present work, PIV was used to study the velocity fields of a supercritical fluid (freon R-23) in a Rayleigh-Bénard convection cell. With this technique the local and instantaneous velocities of a fluid at multiple points in a planar cross-section of the domain were measured simultaneously. Planar PIV was used to measure the two components of the velocity field that are in the measurement plane.

PIV works by tracing the fluid flow with particles chosen such that they accurately follow the flow. The fluid is seeded with particles, which is then illuminated by a laser sheet at two different instants of time. The region illuminated by the laser sheet defines the measurement section, and it is the only part of the flow that is illuminated. Only in this section the particles are visible, because they scatter the

laser light.

A camera, placed in front of the laser sheet, takes two recordings of the tracer particles at the two time instants when they are exposed by the laser-light pulses. The two exposures are captured in two successive frames of a digital camera two camera called frame 0 and frame 1. The exposure time delay (Δt) between them is known, and it can be chosen accordingly to the flow velocity to achieve a desired displacement of the particle images recorded by the camera. By measuring the displacement of the particle images from frame 0 to frame 1, the local and instantaneous fluid velocities can be reconstructed. A detailed description of the PIV working principle can be found in [7, 8].

5.3. Optical distortions in supercritical fluids and applicability of PIV

Fluids above the gas-liquid critical point are characterized by sharp changes of properties within a narrow range of temperatures and pressures (see Figure 3.1). In particular the density changes sharply from a liquid-like value to a gas-like value, when temperature is increased at constant pressure. Density changes of the fluid are associated with changes in refractive index. The relation between density and refractive index can be expressed by the empirical law of Gladstone-Dale:

$$n = 1 + K\rho, \tag{5.1}$$

where K is a material constant that depends on gas characteristics and the light wavelength; it is a weak function of temperature and pressure [11]. For the Gladstone-Dale law, when the density of a material increases, its refractive index also increases, because light travels slower through this material. This relation is valid for homogeneous materials.

In PIV measurements in fluids with varying refractive index, the light scattered by a particle may be deviated, because of refractive index gradients, as described by formulas (5.2) and (5.3).

$$\epsilon_X = \frac{1}{n}\int \frac{\partial n}{\partial X} dZ, \tag{5.2}$$

$$\epsilon_Y = \frac{1}{n}\int \frac{\partial n}{\partial Y} dZ, \tag{5.3}$$

where X and Y indicate the horizontal and the vertical directions of the measurement plane, while Z is the normal direction to the measurement plane, as shown in Figure 5.1. Refractive index changes lead to several difficulties in the applicability of optical techniques. One is that strong optical distortions due to density and associated refractive index changes may blur a particle image or, in an extreme case, make it invisible to the camera. This can make difficult to find a peak in the cross-correlation between the interrogation windows of frame 0 and frame 1. Optical distortions are also responsible for errors in the registration of the particle-image

position of a particle, that may not correspond to the real one. Since this position error may be in both frames, it additionally leads to an error in the determination of the particle displacement from frame 0 to frame 1 with an erroneous conversion to a velocity. Elsinga *et al.* [4] showed that the mayor source of error in PIV measurements in continuously changing refractive index media is the second derivative of the refractive index in the direction of the flow. This is due to the contribution of particle-position errors to the velocity measurements.

Figure 5.2 shows a camera image of the tracers particles at the experimental conditions studied in this thesis. An uncertainty estimation of the velocity errors of this experimental study is done in Section 5.8.4.

5.4. Instrumentation for PIV measurements

Planar PIV measurements were performed at supercritical conditions in the cell described in section 4.3. The instrumentation used consists of a laser, a camera, a software package that controls them (DaVis 8.3 from LaVision), and tracer particles injected into the fluid. The camera is placed in front of the large side window of the cell, and the sensor of the camera is parallel to it. The laser is placed in front of the small window of the cell, and the laser beam is aligned with the center of the circular window. Figure 5.1 shows the relative positions of the camera, cell, and laser sheet.

5.4.1. Particles

When selecting particles for the experiments at supercritical conditions we firstly need to look for appropriate mechanical particle properties allowing them to follow the fluid motion accurately. The difference between the fluid velocity, u and the particle velocity, u_P is known as slip velocity, U_{slip}. For very low Reynolds numbers, the slip velocity of a particle in a continuously accelerating fluid can be calculated using the Stokes' drag law [10] as:

$$U_{slip} = U_P - U = d_P^2 \frac{(\rho_P - \rho)}{18\mu} a, \tag{5.4}$$

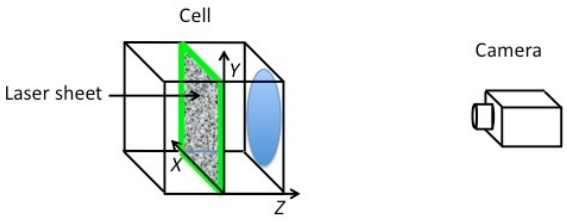


Figure 5.1: Sketch of the relative position of camera, cell, and laser sheet for planar PIV measurements, with indication of X, Y, and Z coordinates.

where d is the particle diameter, ρ_P the density of the particle, and ρ and μ the density and the dynamic viscosity of the fluid respectively. From formula (5.4), it can be seen that to reduce U_{slip} the density of the particle should closely match the density of the fluid and d_P should be as small as possible. d_P however should be also large enough to allow good light scattering properties of the particle.

At higher flow velocities the velocity-slip equation is more complex [9, 10, 12–14] and also other aspects like unsteady history, added mass and fluid stress terms should be taken into account in the choice of appropriate tracers particles. Their effect was studied by Mei, 1996 [13] with a frequency response analysis of the particle to a sinusoidal oscillation of the free stream. In this study, the frequency response of the particle was expressed as a function of a Stoke's number, defined as non-dimensional frequency of the fluid oscillation, and the density ratio between the particle and the fluid density. Cut-off limits in the frequency-defined Stokes number are proposed based on the value of the energy transfer function, which is expressed as the mean square value of the frequency-response function of the particle. From them, an ideal ratio between the density of the particle and the density of the fluid, to guarantee good tracer properties of the particles can be determined. For a density ratio between particle and fluid comprised between 0.56 and 1.62 a very good response of the tracer particles was found. The present experiments were characterized by a substantial variation of the fluid density and viscosity. Which particles were used in an experiment depends both on the density of the fluid at the average temperature between the bottom and top plate temperatures of the Rayleigh-Bénard cell, and on the densities of the fluid at the bottom and top plates. The former was considered in order to minimize the velocity slip due to Stokes' force and the latter to make sure that the largest and smallest density ratio of the experiments were within the limits of good particle-frequency response analyzed by Mey, 1996 [13].

Table 5.1 reports the density and the diameter of the particles used in the experiments, the ratio between a characteristic time due to Stokes' drag and the integral time of the flow estimated from experiments and the values of the density ratio between the particle density and the fluid density for each experiment. This density ratio is comprised between 0.89 and 1.61, allowing good tracer properties of the particles at the experimental conditions of the measurements according to Mey's study [13]. The particles used are hollow glass microspheres, produced by Cospheric LLC. They are made of sodium silicate (77-88 % in weight), sodium borate (7-18 % in weight) and amorphous silicon dioxide (< 5% in weight). Particles of these materials were selected because they are chemically compatible with the supercritical trifluoromethane (R-23) used in the experiments. It was seen in previous experiments done in the same lab at the Reactor Institute of TU Delft that plastic materials dissolve in supercritical R-23 and hence are not suitable for the experiments. Other kinds of particles were also tested, in particular silver coated hollow glass spheres and titanium coated hollow glass spheres. These particles, however, were unsuitable for the experiments, because they stayed attached to the walls and formed a kind of "crust" when exposed to the supercritical freon. Since the non-coated hollow glass particles showed the tendency to agglomerate

in static big clusters as well, it was necessary to prevent the formation of these clusters before starting the operation of the facility. It was not possible to open the high-pressure set-up and to manually break them. A solution was found by cleaning the particles with ethanol before putting them into the set-up. Ethanol dissolves and removes chemicals that may be attached to the particles. Also the internal walls of the set-up were cleaned with ethanol to avoid adhesion of the glass particles on the surfaces. Figure 5.2 shows a camera recording of the particles acquired in a thermally convective flow at supercritical conditions.

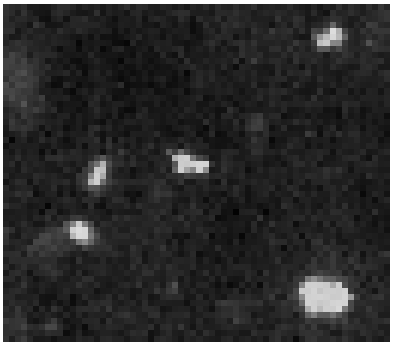


Figure 5.2: Camera image of particles at supercritical conditions in a thermally convective flow (pressure: 5.52 MPa, temperature bottom plate: 309.5 K, temperature top plate: 307 K, fluid:R-23). The particles that are illuminated by the laser are visible as bright spots.

Introduction of particles into the set-up

Particles were put into the set-up, in the internal glass-cube of the RB cell, before filling it with freon. Then the air in the set-up is drained with a vacuum pump, and the set-up is filled with freon, as described in Chapter 4. During operation of the facility, particles went outside the internal glass-cube of the cell, where there was thermal convection motion, and settled between the glass cube and the stainless steel structure of the RB cell, where the fluid is at rest. To avoid this quick loss of particles from the measurement volume, while maintaining the possibility for the fluid to expand or compress as needed, the internal cube was partially sealed in the regions with the largest gaps. The sealing was made of rubber, allowing the particles to stay within the measurement volume (for about 16 hours of operation of the facility at stationary conditions) and to perform PIV measurements. After approximately two days or after changing the operational conditions of the facility, the particle concentration becomes too low to allow measurements and the set-up needs to be opened and cleaned, before inserting new particles.

5.4.2. Laser

The laser used in the measurements is a diode pumped solid state laser. It is a continuous wave laser of class IV, with a power of 5 W and a wavelength of 532 nm. It is controlled and triggered by the DaVis software with a frequency from 0 to 10 kHz. For the PIV experiments the images were acquired at a frame rate

of 3 Hz with a pulse separation time of 20 μs, which corresponds to a maximum displacement of 10-12 pixels. A spherical and a cylindrical lens were used to make a laser sheet. The spherical lens makes the laser beam smaller, while the cylindrical lens spreads it into a sheet. The lenses are made of glass BK7, which is ideal to transmit the wavelength of the laser (λ = 532 nm). They have an antireflective coating for frequencies from 527 to 532 nm, optimized for 532 nm with overall transmission > 95%. The cylindrical lens has a focal length of -3.9 mm. This small focal length was necessary to create a laser sheet that covers the full height of the cell (H=70 mm) through the small lateral window of the cell (see Figure 4.4). The lens was placed right in front of the window. The laser sheet generated for the measurements was about 1 mm thick (measured value) and. Its wideness is limited by the dimensions of the optical window and it is approximately 70 mm only on one side of the measurement section, not allowing to illuminate at the same time both the bottom and the top horizontal boundary layers. This was not a problem for the present study, because only the large-scale flow structures were studied. The lasr-sheet thickness is smaller than the focal depth thickness calculated from equation (5.5), ensuring good focusing conditions of the particles.

5.4.3. Camera

The camera used for the PIV measurements is a LaVision Imager MX, with resolution of 2048 X 2048 pixels and pixel size of 5.5 μm. The image sensor is a CMOSIS CMV4000 with dimensions of 11.26 X 11.26 mm.In the experiments shown in this thesis the camera was operating with a dynamic range of 12 bits per pixel, and an interframing time of 20 μs. The camera is equipped with an objective with a focal length of 50 mm and the aperture stop used for the measurements was either 8 or 5.6, depending on the experiment (see table 5.1). The field of view of the recordings is 7×7 cm^2 and the image magnification factor is M_0 = 0.13. The depth of field (δ_Z) of the measurements computed from equation (5.5) is about 5 mm for $f_\# = 5.6$ and 10 mm for $f_\# = 8$. All particles that lie within $\pm(\delta_Z)/2$ can be considered being well focused because of diffraction limits. The effect of aberrations was not quantified in the present study.

$$\delta_Z \cong 4\left(1 + \frac{1}{M_0}\right)^2 f_\#^2 \lambda \tag{5.5}$$

5.5. Background oriented schlieren

The background oriented schlieren (BOS) technique is an optical technique that was used in this study to quantify optical distortions due to refractive index changes in supercritical fluids. It does not need tracer particles, and it was used before performing PIV measurements to estimate optical distortions and associated errors. An explanation of the BOS working principle can be found in a paper by Richard *et al.*, 2001 [15]. The set-up used for the BOS measurements consists of a Rayleigh-Bénard cell, a background dot pattern, and a camera. It is the same set-up used for the PIV measurements, with only two main differences: One is that the particles and the laser were substituted by a computer generated background

dot pattern and a table light as shown in Figure 5.3; The other one is that while the PIV laser sheet is at half depth of the cell, the BOS background is at the back of the cell. The background dot pattern is a computer generated image that should

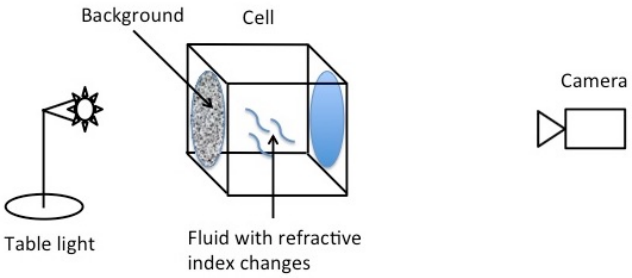


Figure 5.3: Sketch of the set-up used for background oriented schlieren measurements. The main components of the set-up are shown: the RB cell, represented by a cube with a window drawn as a light-blue circle and a background pattern attached to its back face, a camera and a table light.

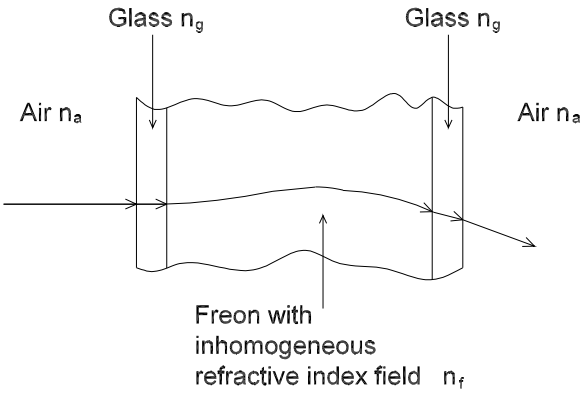


Figure 5.4: Sketch of a light ray optical path from the table light to the camera objective, when the cell is filled with freon with inhomogeneous refractive index field. n indicates the refractive index of a media.

replicate a camera recording of PIV particles. For this reason, the particles were drawn such that their intensity goes gradually from white to black with a gaussian intensity distribution, as it is in a PIV recording, due to imaging-optics effects. An example of this background is reported in Figure 5.5, while camera images of this background are shown in paragraph 5.8.1. Figure 5.4 shows the optical path of a light ray coming from the table light and going through the cell filled with freon with a temperature induced refractive index field.

A BOS instantaneous measurement consists of two camera recordings of the background image placed at the back of the cell. One is taken as a reference, and

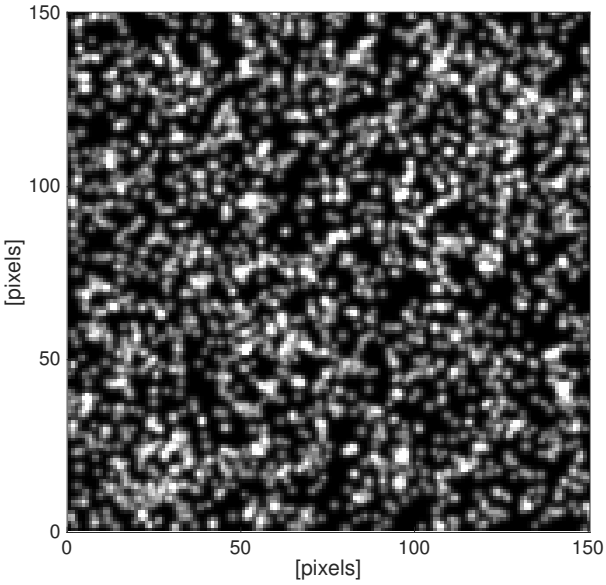


Figure 5.5: Example of computer generated background dot pattern for BOS measurements. This kind of background was made 2000 ×2000 pixels with a mean diameter of the white dots of about 2 pixels, and it was printed with dimensions of 80 ×80 mm^2.

it is acquired without temperature gradient, which means also without optical distortions and flow. Another one is acquired with a temperature gradient imposed on the cell with the fluid moving due to thermal convection. In this case the density differences within the fluid lead to optical distortions due to the variations of the refractive index that changes with the local density of the fluid. Deviations of the light coming from the back of the set-up are visible in the recorded background image. By cross-correlating the two recordings (with the same algorithm used for the PIV measurements), it is possible to compute a displacement due to the variations of the instantaneous refractive index integrated along the line-of-sight of the fluid (see Paragraph 5.8.3). In a two dimensional flow, this displacement can be used to determine local density values [16]. In this case the flow is three dimensional, and the measured BOS deflection is proportional to the mean spatial gradients of the refractive index integrated along the line-of-sight. Hence it is not possible to determine local density values, but only integrated ones along the depth of the domain (line-of-sight), which are not directly useful for the present study.

BOS measurements were used as a preliminary investigation before doing PIV measurements, to check whether at the chosen experimental conditions the optical distortions still allowed to sufficiently see the particles. The autocorrelation of image intensity allows the assessment of a particle image size with and without optical distortions by the fluid. The difference is a measure for image blur. A broad

correlation peak is known to increase uncertainty in the PIV measurements, or may even result in velocity vector outliers.

5.6. Data process settings and spatial resolution of the measurements

The PIV and BOS images were processed with the DaVis 8 software from La Vision. A two passes cross-correlation algorithm with decreasing interrogation window size was used. The size of the second pass is $[32 \times 32]$ pixels for all the BOS measurements and $[48 \times 48]$ pixels for all the PIV experiments, except for one case, that is PIV $SC_{max\Delta\rho}$ (see Table 5.2), where it is $[64 \times 64]$ to gain a larger number of good vectors resulting from the interrogation algorithm. The overlap of the interrogation windows is 50%. The spatial resolution of the BOS measurements is 1.35 mm, while of the PIV measurements is 2 mm, except for the $SC_{max\Delta\rho}$ case, where it is 2.7 mm.

Table 5.1: Aperture stop, $f_{\#}$, values of the BOS (BOS SC_{liquid}, BOS $SC_{max\Delta\rho}$, BOS SC_{gas}) and PIV experiments (PIV SC_{liquid}, PIV $SC_{max\Delta\rho}$, PIV SC_{gas}). BOS indicates all the three BOS experiments, ρ_P the density of the particles and d_P the particle diameter. $U_{slip}/(a\tau_I)$ is the ratio between the particle response time computed as in equation (5.4) (with density, ρ, and dynamic viscosity, μ, taken from CoolProp [17] at the average top-bottom temperature of the cell, T_m) and an integral time scale of the flow estimated from experiments, τ_I. The last two rows show respectively the minimum and the maximum values of the ratio between the particles density, ρ_P, and the fluid density, ρ_f, for each PIV experiment (values of ρ_f at the top and the bottom temperatures of the cell at the pressures of the experiments were taken from the CoolProp database [17]).

	BOS	PIV SC_{liquid}	PIV $SC_{max\Delta\rho}$	PIV SC_{gas}
$f_{\#}$	8	8	5.6	5.6
ρ_P [g/cm^3]	/	0.68	0.55	0.55
d_P [μm]	/	5-20	5-27	5-27
$U_{slip}/(a\tau_I) * [10^{(-2)}]$	/	0.003	0.015	0.035
$[\rho_P/\rho_f]min$	/	0.89	0.93	1.35
$[\rho_P/\rho_f]max$	/	1.05	1.32	1.61

5.7. Experimental programme

BOS measurements were performed at supercritical conditions to check the applicability of PIV in a region with strong optical distortions. Three experiments were done with different density difference between the top and the bottom of the cell. Afterwards PIV measurements were done at the same experimental conditions. Table 5.2 shows the experimental conditions of all the BOS and the PIV experiments. In this table, in the first six lines the pressure (p) and the temperatures of the top and of the bottom plates of the cell (T_t) and (T_b) are reported, together with the standard deviations (std) of the electric signal from the thermistors. The std was computed as:

$$std(X) = \sqrt{\frac{1}{N-1}\sum_{i=1}^{N}|X_i - \mu|^2}, \tag{5.6}$$

where X is a generic quantity, N is the number of samples, (N = 10800 as explained in Chapter 4) and μ is the mean of X, computed as:

$$\mu = \frac{1}{N}\sum_{i=1}^{N} X_i. \tag{5.7}$$

The uncertainty of the temperature and pressure measurements are reported in Chapter 4, Section 4.2.1. The three experimental conditions chosen for the PIV and the preliminary BOS study are called SC_{liquid}, $SC_{max\Delta\rho}$ and SC_{gas} and are shown in the Pr(T,p) plane of Figure 5.6.

The calculated densities (ρ) and refractive indices (n) at the top and bottom plate temperatures of the cell are reported in the last six rows of Table 5.2. The density values of freon R-23 were taken from the CoolProp database [17] and the refractive index values as a function of ρ were taken from Avdeev *et al.* [18], using

Table 5.2: Data matrix of the BOS and of the PIV experiments. p is the pressure of the cell and std(p) its standard deviation, T_t is the top plate temperature and std(T_t) its standard deviation, T_b is the bottom plate temperature and std(T_b) its standard deviation, $\rho(T_t)$ and $\rho(T_b)$ are the densities of F_3CH at T_t and T_b respectively, $\Delta\rho$ is the difference between $\rho(T_t)$ and $\rho(T_b)$, n($\rho(T_t)$) and n($\rho(T_b)$) are the refractive indexes of F_3CH at T_t and T_b respectively and Δn is the difference between n($\rho(T_t)$) and n($\rho(T_b)$). ρ values taken from the CoolProp database [17] and n(ρ) values taken from Avdeev *et al.* [18].

	p [kPa]	**std(p) [kPa]**	**T_t [K]**	**std(T_t) [K]**	**T_b [K]**	**std(T_b) [K]**
BOS SC_{liquid}	5519	6.10	301.0	0.07	303.6	0.07
BOS $SC_{max\Delta\rho}$	5516	4.25	304.1	0.08	306.5	0.08
BOS SC_{gas}	5512	4.94	307.1	0.08	309.6	0.08
PIV SC_{liquid}	5516	6.93	301.0	0.08	303.5	0.07
PIV $SC_{max\Delta\rho}$	5500	3.18	304.1	0.08	306.5	0.08
PIV SC_{gas}	5519	6.37	307.0	0.08	309.5	0.08
	$\rho(T_t)$ [kg/m^3]	**$\rho(T_b)$ [kg/m^3]**	**$\Delta\rho/\rho(T_b)$ X 100**	**n($\rho(T_t)$)**	**n($\rho(T_b)$)**	**$\Delta n/n(\rho(T_b))$ X 100**
BOS SC_{liquid}	759.57	645.65	17.64	1.1134	1.0978	1.42
BOS $SC_{max\Delta\rho}$	608.91	426.72	42.69	1.0926	1.0633	2.76
BOS SC_{gas}	401.48	338.54	18.59	1.0589	1.0501	0.84
PIV SC_{liquid}	760.38	649.03	17.16	1.1135	1.0963	1.57
PIV $SC_{max\Delta\rho}$	592.65	416.97	42.13	1.0901	1.0615	2.69
PIV SC_{gas}	407.01	341.97	19.02	1.0597	1.0506	0.87

the Lorentz-Lorentz equation (5.8). The Lorentz-Lorenz equation relates density and refractive index of a substance as:

$$\frac{n^2-1}{n^2+2} = A\rho, \tag{5.8}$$

where A is a material constant related to polarizability which does not depend on temperature. The values of $(\rho_t - \rho_b)/\rho(T_m)$ and $(n(\rho_t) - n(\rho_b))/n(\rho(T_m))$ show the importance of the difference of density or refractive index between the top and the bottom of the cell with respect to its value at the mean top-bottom temperature (T_m). The values of density as a function of temperature for all the BOS and PIV experiments are also plotted in Figure 5.7. The experiment $SC_{max\Delta\rho}$ is the one with the biggest difference of density and refractive index between the top and the bottom of the cell. The experiment SC_{liquid} is characterized by larger values of densities, closer to the liquid phase, while the experiment SC_{gas} by lower values, closer to the gas phase.

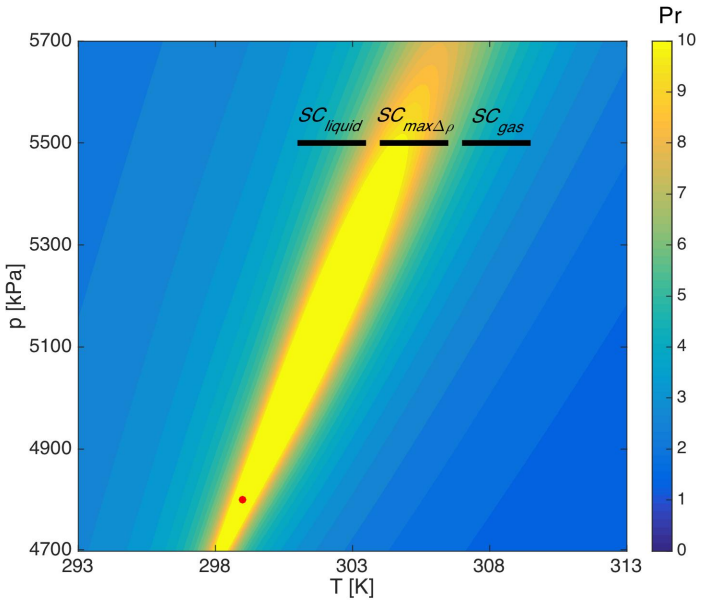


Figure 5.6: Prandtl number values of freon R-23 as a function of temperature and pressure. Red dot: critical point. Black lines: temperature values of the experiments SC_{liquid}, $SC_{max\Delta\rho}$ and SC_{gas} (see Table 5.2 for further details about these three experiments).

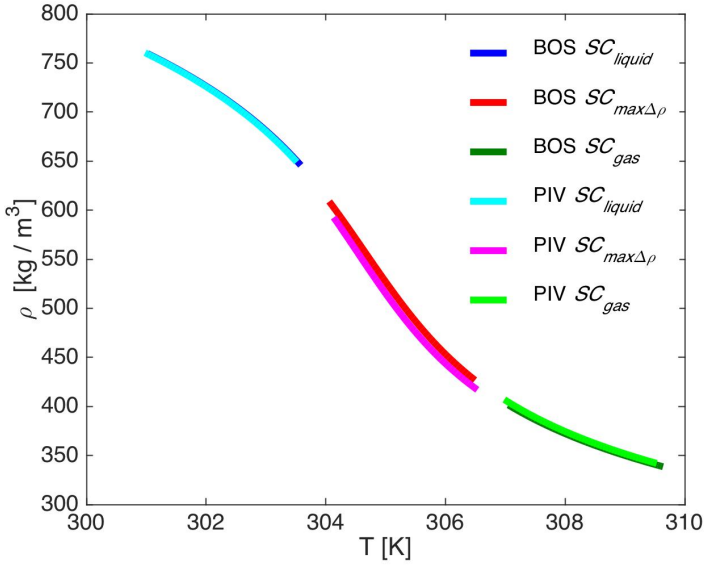


Figure 5.7: Density as a function of temperature for every BOS and PIV experiment (BOS SC_{liquid}, BOS $SC_{max\Delta\rho}$, BOS SC_{gas}, PIV SC_{liquid}, PIV $SC_{max\Delta\rho}$ and PIV SC_{gas}).

5.8. Results

Results of the preliminary BOS study and of the PIV measurements at supercritical conditions are presented here. A BOS study was done before performing PIV measurements to estimate their feasibility and uncertainty.

5.8.1. Preliminary investigation with BOS images

The BOS reference image with and without temperature gradient applied on the horizontal plates of the cell is shown in panels (a) and (b) respectively of Figures 5.8, 5.9 and 5.10. Figure 5.8 shows instantaneous BOS images at the experimental conditions of SC_{liquid}, while Figures 5.9 and 5.10 relate to the experimental conditions of $SC_{max\Delta\rho}$ and SC_{gas} respectively. The optical distortions due to temperature gradients are visible in panels (a) of these three figures as a blurring in the background image, that is not visible in the corresponding (b) panels.

In panel (a) of Figure 5.9 one finds three red dots. Two of that are located in blurred regions, close to the bottom boundary layer and in a plume at the center of the cell. The other one is in a region without optical distortions. From this figure it can be seen that the white dots on the background are difficult to distinguish in the blurred regions. This is what also may happen with images of tracers particles in PIV measurements, even if the illuminated PIV particles are located at half depth of the cell and not on its back wall as it is the case for the BOS background target. Therefore, the thickness of the layer of fluid with refractive index changes in the PIV measurements is half than in the BOS measurements.

To quantify the effect of optical distortions on the blurring of a particle, the spatial autocorrelation function of the particle intensity was computed for each of the three red points of Figure 5.9, both with and without temperature gradient. They are shown in panels (a) and (b), respectively. The intensity autocorrelation function (I_a) in a region of $[128 \times 128]$ pixels (X_{ref}, Y_{ref}) around a generic point (X_0, Y_0), was computed with formula (5.9). The size of the reference region was chosen of [128 ×128] pixels, because it is the same size of the first-pass interrogation window used for the PIV measurements made at the same experimental conditions.

$$I_a(X_{ref}, Y_{ref}) = \frac{\sum_{x=-20}^{20} I_f(X_{ref}, Y_{ref}) I_f(x, Y_{ref})}{I_a^*}, \tag{5.9}$$

where (X_{ref}, Y_{ref}) is calculated as: $(X_0 - 63) \leq X_{ref} \leq (X_0 + 64)$ and $(Y_0 - 63) \leq Y_{ref} \leq (Y_0 + 64)$, with dimensions in pixels,

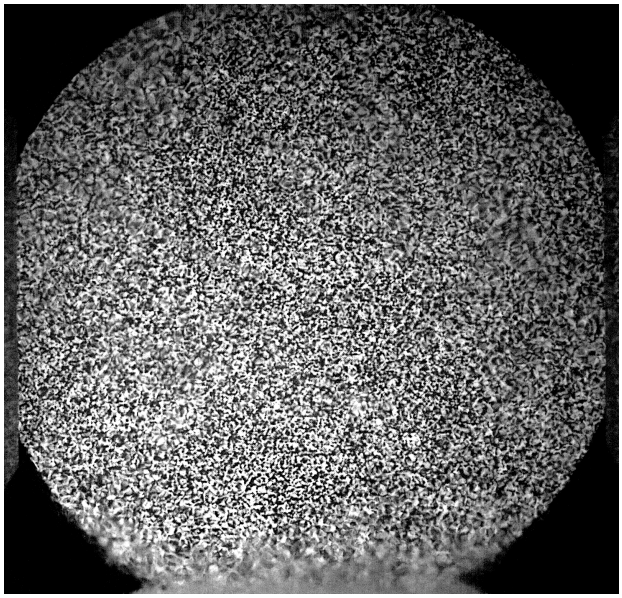
$$I_a^* = \sum_{x=-20}^{20} I_f(X_0, Y_0) I_f(x, Y_0), \tag{5.10}$$

and I_f is the fluctuating component of the intensity field, calculated as:

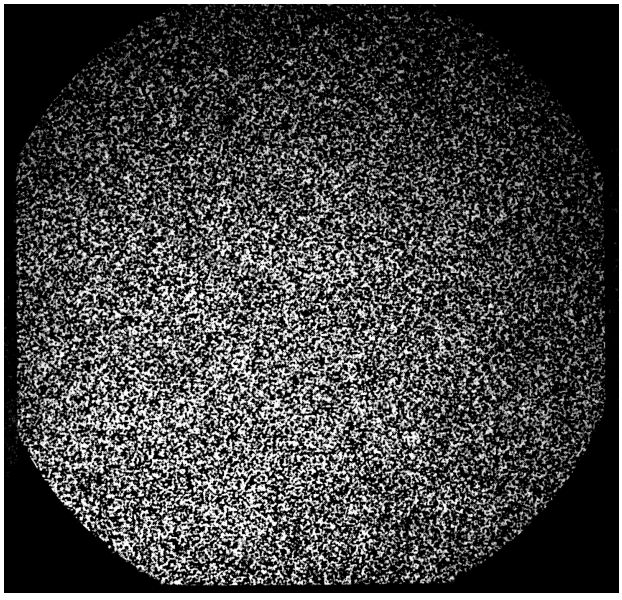
$$I_f(X_{ref}, Y_{ref}) = I(X_{ref}, Y_{ref}) - I_{mean}(X_{ref}, Y_{ref}). \tag{5.11}$$

$I_{mean}(X_{ref}, Y_{ref})$ is the spatial mean of the light intensities in the region (X_{ref}, Y_{ref}).

Figure 5.11 shows (I_a) calculated in the red points of Figure 5.9. In panel (a),

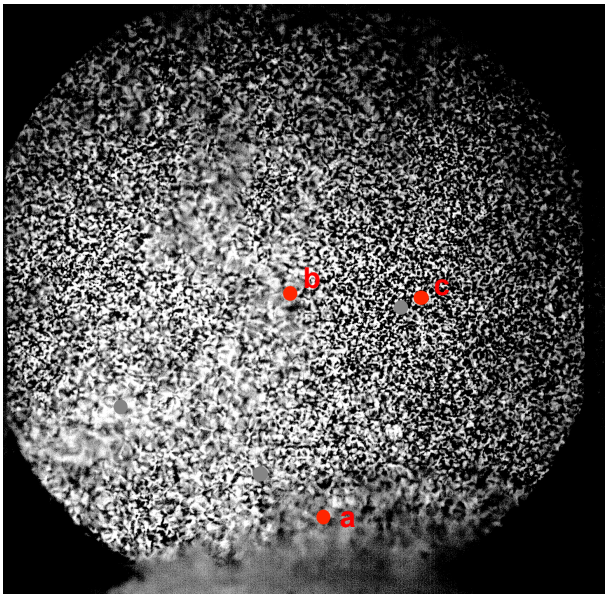


(a)

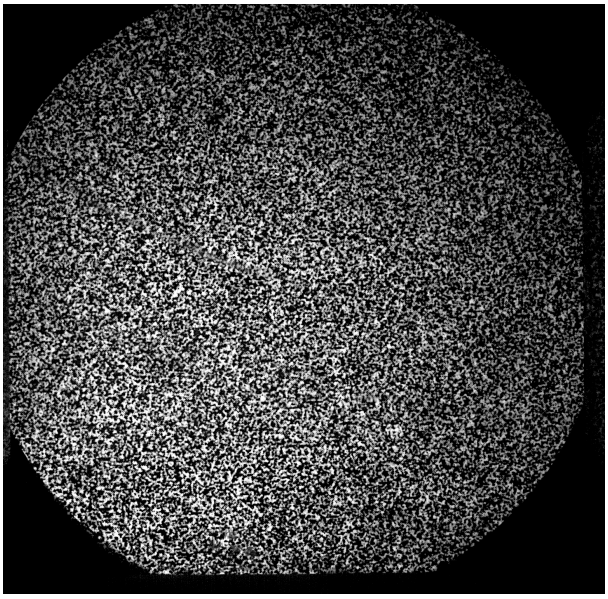


(b)

Figure 5.8: BOS SC_{liquid}: (a) Instantaneous camera image of the BOS background with temperature gradient (ΔT = 2.6 K); (b) Camera image of the BOS background without temperature gradient, used as reference.

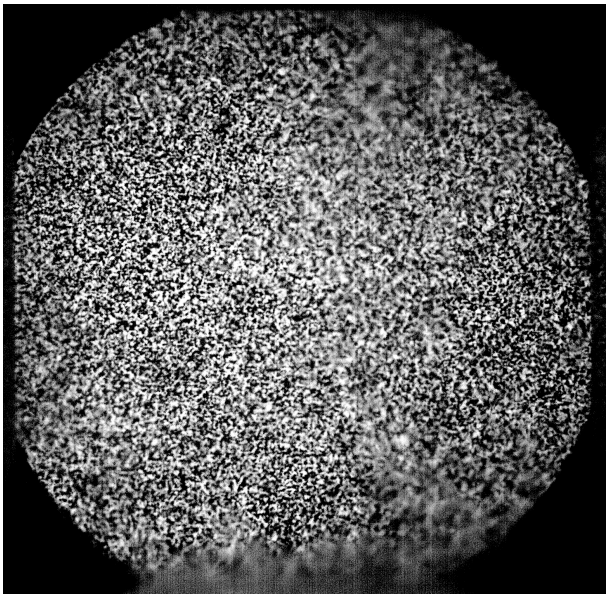


(a)

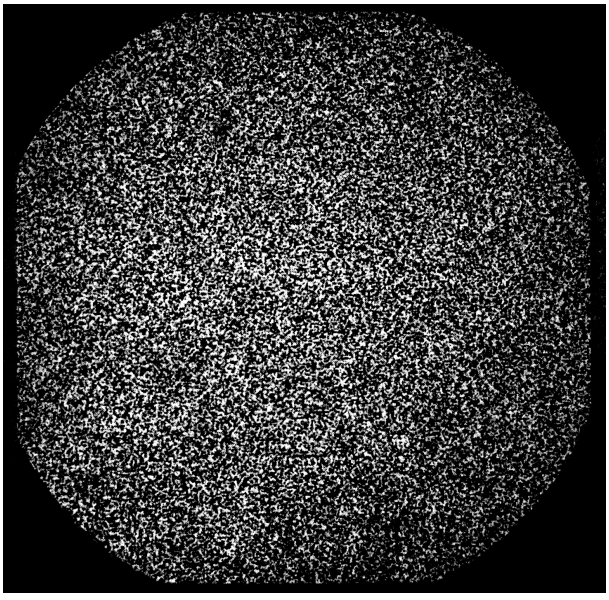


(b)

Figure 5.9: BOS $SC_{max\Delta\rho}$: (a) Instantaneous camera image of the BOS background with temperature gradient (ΔT = 2.4 K). The three red dots with letters indicate the points where the autocorrelation functions of Fig. 5.11 were calculated; (b) Camera image of the BOS background without temperature gradient, used as reference.



(a)



(b)

Figure 5.10: BOS SC_{gas}: (a) Instantaneous camera image of the BOS background with temperature gradient (ΔT = 2.5 K); (b) Camera image of the BOS background without temperature gradient, used as reference.

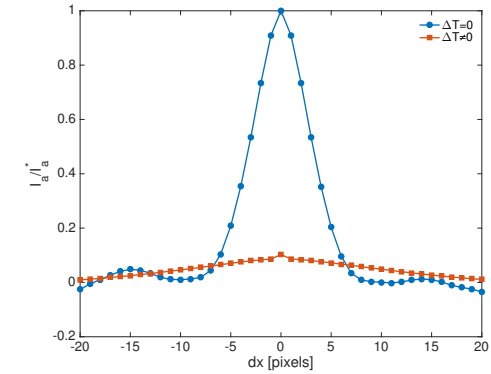
the autocorrelation function of the point close to the bottom boundary layer (indicated with a in panel (a) of Fig. 5.9) is plotted with and without temperature gradient, in panel (b) (I_a) in a plume at the center of the cell (indicated with b in panel (a) of Fig. 5.9) is plotted and in (c) (I_a) at the center of the cell in a region without evident optical distortions (indicated with c in panel (a) of Fig. 5.9) is plotted. An evident attenuation of the peak of the autocorrelation function in the case with temperature gradient is visible in panels (a) and (b). The autocorrelation in these cases becomes broader than the corresponding function without temperature gradient, indicating a larger standard deviation of the curve. In case (a) the autocorrelation with temperature gradient is lost. No important decrease or broadening of the autocorrelation function peak is visible in the point plotted in panel (c) instead. The comparison of the autocorrelation peaks shows that at the experimental conditions of the case $SC_{max\Delta\rho}$ (the one with the largest refractive index changes), the autocorrelation peaks are detectable, except in the boundary layer. This implies that the PIV cross-correlation algorithm is sufficiently accurate with this level of blurring, in most of the cross-section of the cell. In PIV measurements, since the laser sheet is at half depth of the cell, the light optical path is half with respect to BOS measurements and this should result in smaller optical distortions. An autocorrelation peak of a PIV measurement is shown in Figure 5.12.

5.8.2. BOS time averages and magnification factor of the recordings

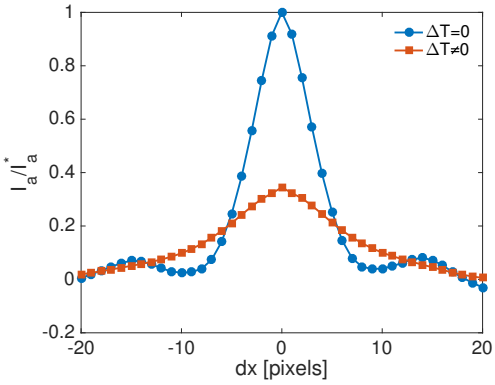
The time-averaged BOS displacement of one-hour long measurements with 10800 samples at the experimental conditions of SC_{liquid}, $SC_{max\Delta\rho}$ and SC_{gas} are shown in Figures 5.14, 5.15 and 5.16 respectively. The image displacements of the three experiments are of the order of 10 μm. This displacement is due to the temperature dependency of the isobaric thermal expansion coefficient of the fluid (shown in Figure 5.13) and it depends on two factors. One is that the mean temperature of the recording without temperature gradient is different from the one with temperature gradient and this leads to a different global magnification factor (M_0). The second one is that in the case with temperature gradient, the temperature field is not uniform through the measurement section, and this leads to non-uniform deflections. These two responsible factors make M_0 of the image with optical distortions different from the one without distortions (used as a reference) both globally and locally. M_0 is defined as the ratio between the dimension of the image in the sensor ($\delta_s = 9.3$ mm) and the dimension of the measurement domain ($H = 70$ mm):

$$M_0 = \frac{\delta_s}{H} \tag{5.12}$$

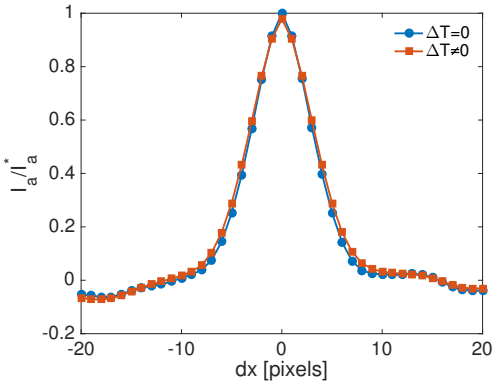
In this case M_0 without temperature gradient is 0.13, as already mentioned in paragraph 5.4.3. Considering the largest BOS displacement among the studied cases, the one of Figure 5.16, M_0 does not change. The image displacement of this experiment is about 40 μm (see Figure 5.16), which corresponds to 7.3 pixels. It can be concluded that the effect of the temperature dependency of the volumetric



(a)



(b)



(c)

Figure 5.11: Instantaneous autocorrelation functions in three points of the experiment BOS $SC_{max\Delta\rho}$, with and without temperature gradient (ΔT = 2.4 K, squares, red line and ΔT = 0 K, circles, blue line).The three points with a, b, c letters are shown in Figure 5.9 (a) with red dots. Panel (a): autocorrelation function in the point close to the bottom boundary layer (b): point at the center of the cell, where a plume is visible and (c): point at the center of the cell where no plumes are visually detectable.

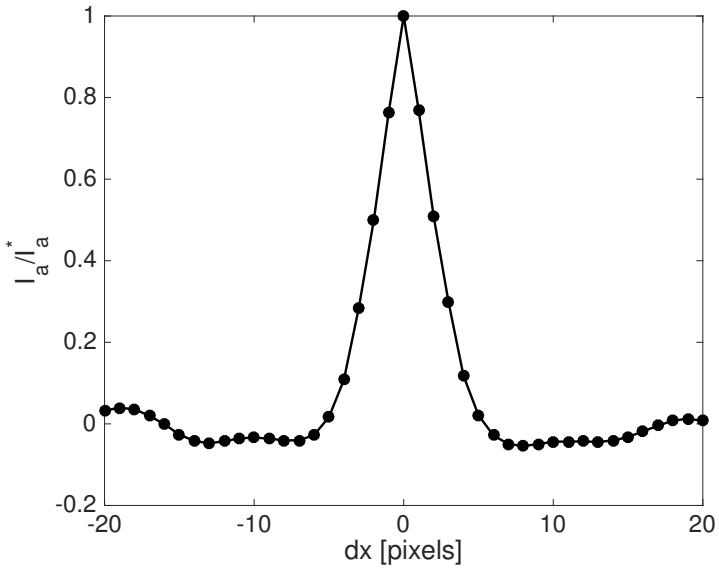


Figure 5.12: Example of autocorrelation function computed from a PIV recording.

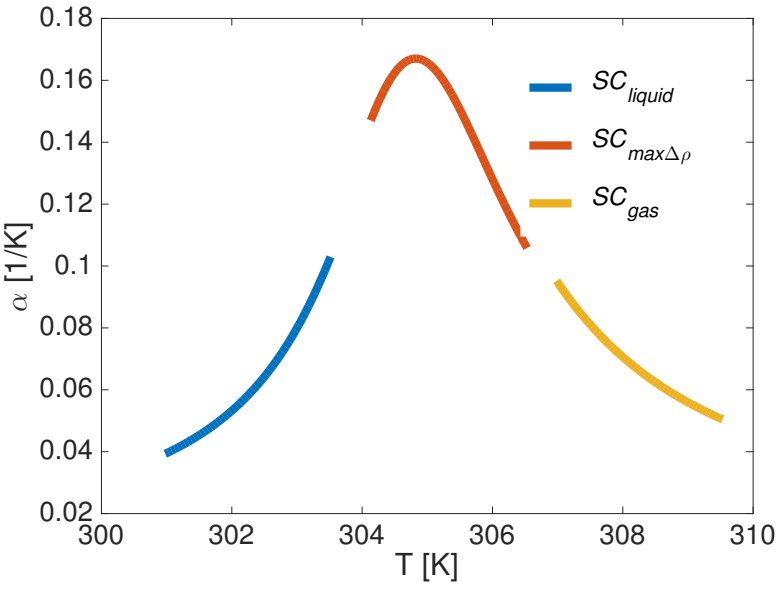


Figure 5.13: Temperature dependency of the isobaric thermal expansion coefficient α for the temperature values of the three BOS experiments SC_{liquid}, $SC_{max\Delta\rho}$ and SC_{gas}.

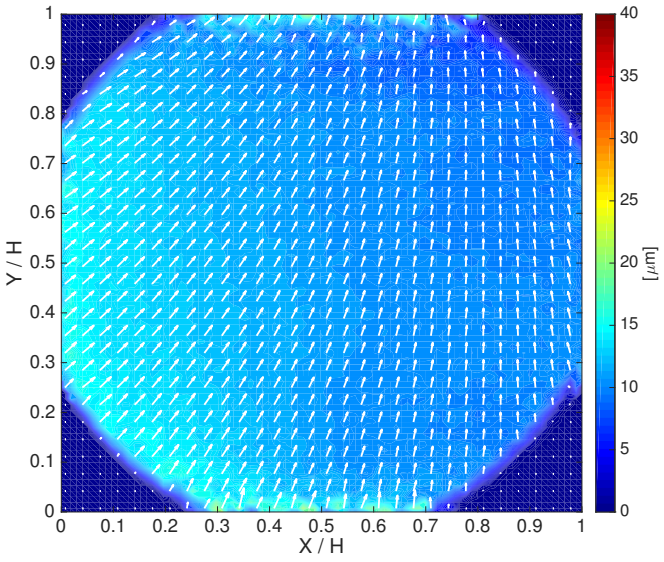


Figure 5.14: Time average of the experiment BOS SC_{liquid}. The color scale indicates the magnitude of the BOS time-averaged image displacement, while arrows indicate its direction. Only one of every nine data points is represented by arrows.

thermal expansion coefficient does not lead to a significant change in the magnification factor of the BOS measurements. For PIV measurements this magnification factor effect can be neglected, because they were acquired at half depth of the cell and the light optical path through the fluid is half long with respect to the BOS measurements.

The main direction of the time-averaged BOS displacement (Figures 5.14, 5.15 and 5.16) can be explained by looking at the values of the isobaric thermal expansion coefficient α in Figure 5.13. In experiment SC_{liquid}, α at the top of the cell is smaller than α at the bottom of the cell and this justifies the upwards BOS time-averaged displacement (Figure 5.14). The same explanation is valid for the experiment SC_{gas} (Figure 5.16), where the downwards time-averaged BOS displacement is due to the larger value of α at the top of the cell, with respect to the bottom. The temperature dependency of α is monotonic in both experiments. In experiment $SC_{max\Delta\rho}$, α exhibits a peak at a temperature comprised between the top and bottom temperature (Fig. 5.13). The main direction of the time-averaged BOS displacement in this case is horizontal and its direction depends on the direction of the large-scale circulation of the flow. The inhomogeneity of the temperature field leads to local deflections that are responsible for PIV velocity errors, as shown in Section 5.8.3.

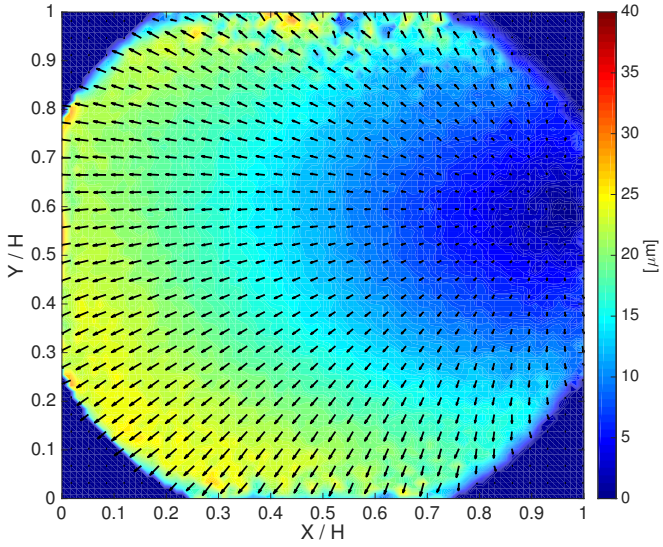


Figure 5.15: Time average of the experiment BOS $SC_{max\Delta\rho}$. The color scale indicates the magnitude of the BOS time-averaged image displacement, while arrows indicate its direction. Only one of every nine data points is represented by arrows.

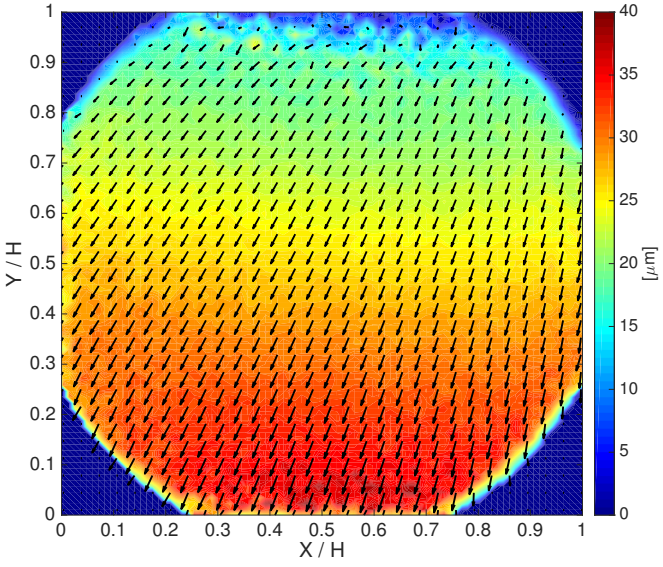
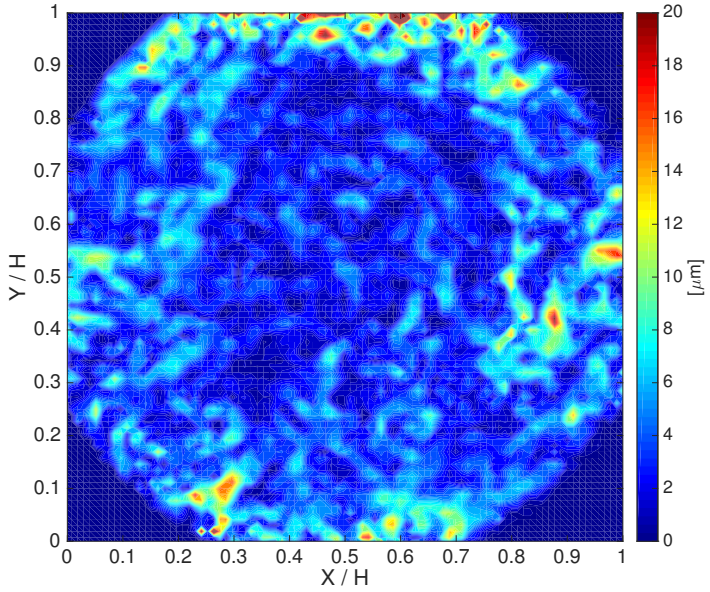


Figure 5.16: Time average of the experiment BOS SC_{gas}. The color scale indicates the magnitude of the BOS time-averaged image displacement, while arrows indicate its direction. Only one of every nine data points is represented by arrows.

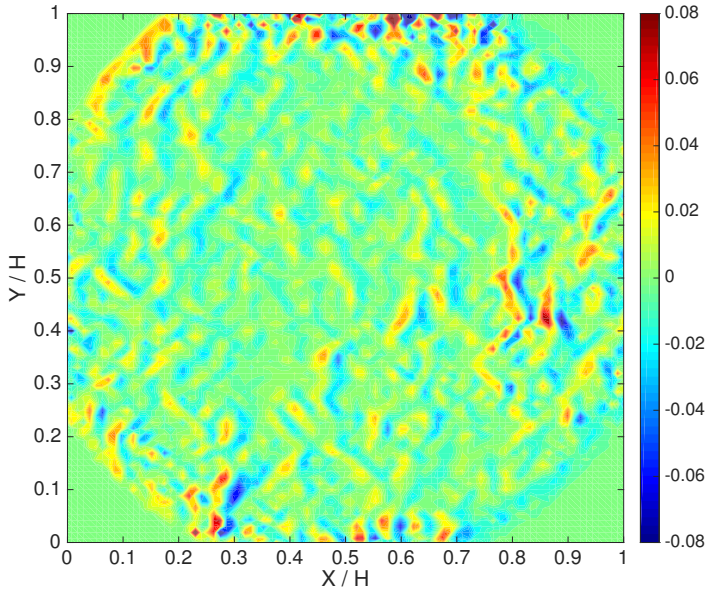
5.8.3. BOS instantaneous measurements

The instantaneous BOS displacements can be obtained by subtracting the time average displacement of the corresponding experiment. The result is shown in panels (a) of Figures 5.17, 5.18 and 5.19 for all three experiments. The density gradient within the flow reflects the thermal structure of the flow. It is associated to the refractive index gradient by the Gladstone-Dale relation 5.1. Light rays are deflected because of the non-zero gradient of the refractive index by an angle ϵ (see equations (5.2) and (5.3)). The deflection of the light rays is visible in the instantaneous BOS image displacements. The instantaneous thermal structures of the flow in the three cases look uniform through the section of the domain. Subtraction of the time-averaged image displacement does not reveal any asymmetry. Thermal plumes erupting from the bottom and top boundary layers are clearly visible in Figure 5.19. The maximum instantaneous BOS image displacement for all the three cases shown in panels (a) of Figures 5.17, 5.18 and 5.19 is about 20 μm (3.6 pixels). This value is about three times smaller with respect to the displacements observed in the PIV measurements.

Local changes in the magnification factor due to refractive index field are responsible for velocity errors in PIV measurements [4]. In particular, as already mentioned in the Section 5.1, it was shown that the second derivative of the refractive index in the direction of the velocity field is the mayor source for optical velocity errors in PIV. The second derivative of the refractive index ($\nabla^2 n$) is proportional to the derivative of the BOS displacement (∇d) [4]. These deflections expressed as ∇d are shown in panels (b) of Figures 5.17, 5.18 and 5.19. Since ∇d computed from these measurements is integrated through the depth of the domain and the flow is not 2D it is not possible to correct the PIV measurements for it as is the case for 2D flows. An uncertainty quantification of the PIV error due to optical distortion is done by using statistical correlations in Section 5.8.4.

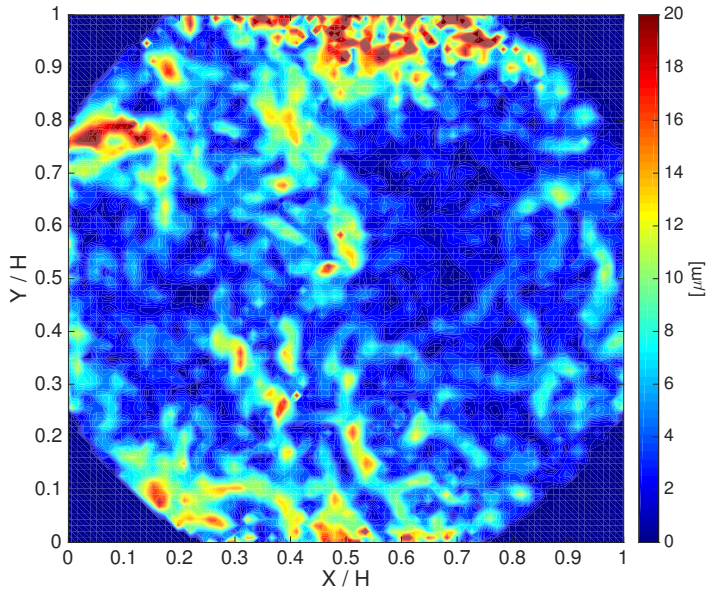


(a)

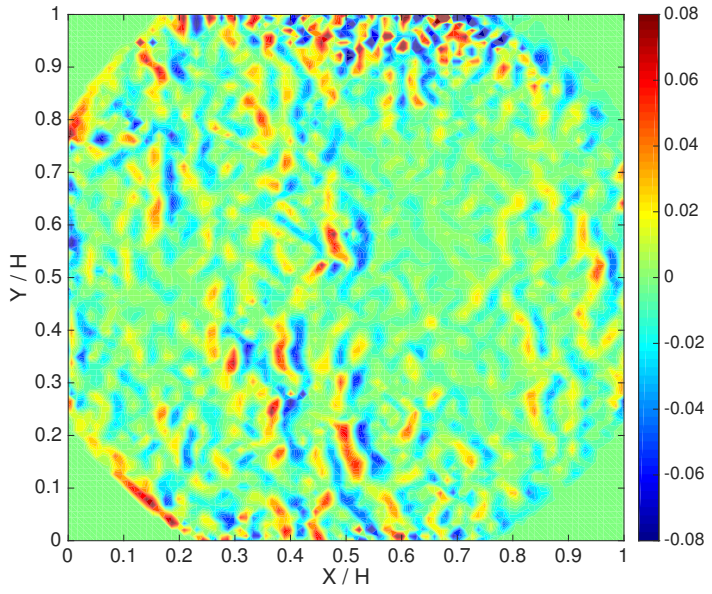


(b)

Figure 5.17: (a) Instantaneous BOS image displacement of the experiment BOS SC_{liquid}, after subtraction of the time average image displacement of that experiment (shown in Figure 5.14). (b) Magnitude of the spatial gradient (∇d) of the BOS image displacement shown in panel (a).

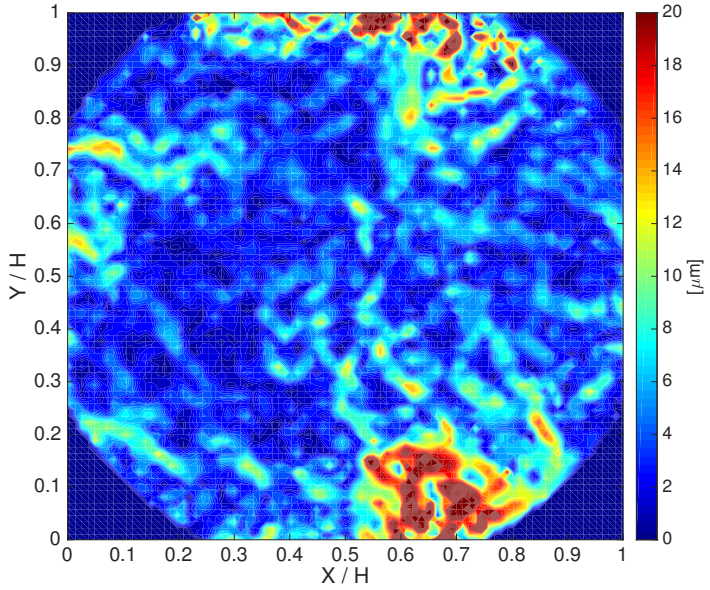


(a)

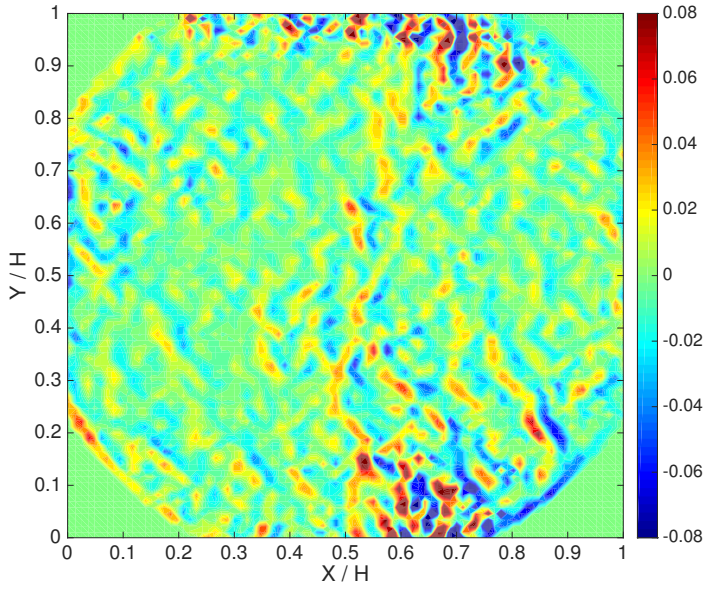


(b)

Figure 5.18: (a) Instantaneous BOS image displacement of the experiment BOS $SC_{max\Delta\rho}$, after subtraction of the time average image displacement of that experiment (shown in Figure 5.15). (b) Magnitude of the spatial gradient (∇d) of the BOS image displacement shown in panel (a).



(a)



(b)

Figure 5.19: Instantaneous BOS image displacement of the experiment BOS SC_{gas}, after subtraction of the time average image displacement of that experiment (shown in Figure 5.16). (b) Magnitude of the spatial gradient (∇d) of the BOS image displacement shown in panel (a).

5.8.4. PIV uncertainty from correlation statistics

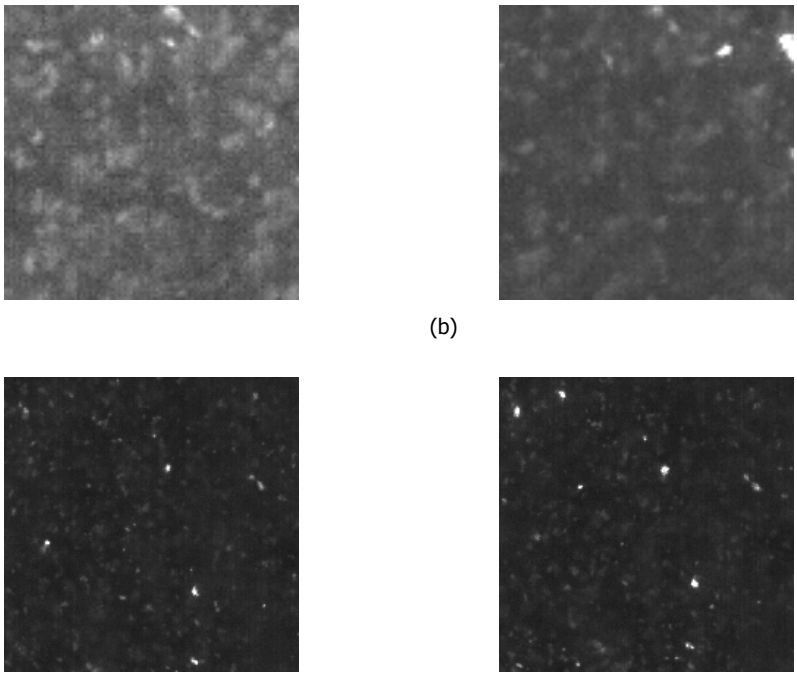
Several factors may contribute to uncertainty in PIV measurements. Some examples are out of plane motion, shear and refractive index fields. The latter leads to optical distortions that cause errors in the position and velocity of PIV tracer particles [4]. It causes also blur that, depending on its magnitude, deforms the viewed particles and decreases their brightness [4].

Out of plane motion is another important source of error for PIV measurements in this case. It is independent of optical distortions. It occurs when the flow moves normal to the plane of the laser sheet. A particle that is illuminated in frame 0 may be transported outside of the laser sheet in frame 1. This leads to a loss of correlation and increases uncertainty [9, 10].

Another kind of error is introduced when the particles within one interrogation window do not move all together in the same direction and with the same magnitude. In this case the cross-correlation map contains multiple peaks, corresponding to the different particle displacements in the cross-correlation window, or a deformed and non-symmetric peak [9, 10, 19]. The PIV algorithm computes the velocity over the interrogation window according to the maximum of the highest cross-correlation peak. Westerweel [19] showed that local gradients in the particle displacement field within the interrogation domain can be neglected, when they are smaller than the mean particle diameter. In the present study also out of plane motions and the above mentioned optical distortions problems lead to errors in the PIV measurements. Examples of PIV images in frame 0 and frame 1 of the above mentioned PIV error sources are shown in Figure 5.20.

The main uncertainty in the present velocity measurements was estimated *a posteriori*, using the method developed by Wieneke *et al.* [20]. It needs as inputs an instantaneous velocity vector field and its two corresponding camera images. Based on the measured velocity field, the two camera images are dewarped to the same time instant halfway in between the interval between the recordings. If there was no uncertainty in the measurements, the two dewarped frames should overlap perfectly. This part of the method was taken from the image matching method proposed by Sciacchittano *et al.* [21]. The two methods differ because in Sciacchitano *et al.* [21] the dispersion and the mean values of the disparity vectors are studied to estimate random and systematic errors respectively. Wieneke's method [20] instead focuses on the asymmetry in the peak of the cross-correlation function between the two dewarped images. It considers individual pixels contributions to the cross-correlation peaks. It is appropriate in the present case, especially because it allows to take into account the effect of optical distortions as deformed particle-image shapes in one or both frames. This may lead indeed to asymmetric cross-correlation peaks.

Figure 5.22 shows an example of the ratio between the cross-correlation function values at specific locations through the measurement section and the correlation values computed at $\pm$ 1 pixel in X-direction with respect to the considered location, for the instantaneous measurement of the experiment SC_{liquid} shown in Figure 5.21. For details of this calculation see [20]. Values of this ratio larger than unity



(a) (b)

(c) (d)

Figure 5.20: Examples of PIV particle images with blurring, out of plane motions and presence of very bright particles. (a) frame 0, (b) frame 1 of the same pixels shown in (a). (c) frame 0, (d) frame 1 of the same pixels shown in (a). These particle images of frame 0 and frame 1 are taken from the instantaneous measurement SC_{liquid}, shown Figure 5.21.

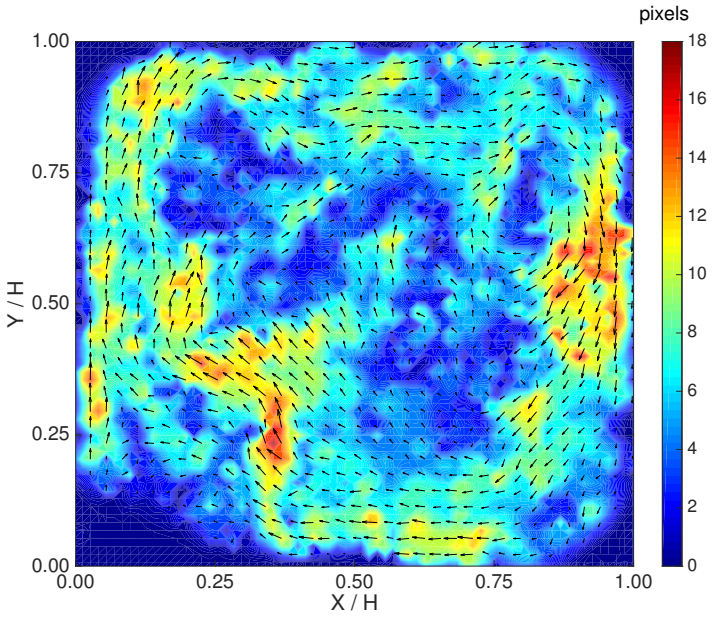


Figure 5.21: Instantaneous displacement field (in pixels) of the PIV experiment SC_{liquid}.

shows a peak of the correlation function. In these PIV measurements the cross-correlation function shows a peak on the whole measurement section with few exceptions. Most of them correspond to the appearance of a very bright particle only in one frame. Since these very bright particles are not present in both frames, the PIV algorithm has difficulties in cross-correlating the right intensity peaks. Very bright particles in only one of the two frames may be due to both out of plane motion and to optical distortions (e.g. in Figure 5.20). Figure 5.23 shows the velocity uncertainty (σ_u) for the instantaneous velocity field in Figure 5.21, computed as in [20]. The points where the estimated uncertainty value is within ± 1 pixel were considered reliable.

Figure 5.24 shows the values of the standard deviation in time of the PIV experiment SC_{liquid}. The standard deviation was computed as in equation (5.6). The points where the cross-correlation function does not present peaks were excluded from the standard deviation (std) calculation and they were set to zero. The std values were used for the calculation of the statistical uncertainty in Section 5.8.5.

5.8.5. Statistical uncertainty

Besides the PIV uncertainty, there is also a statistical uncertainty related to the time-length of the measurements. Rayleigh-Bénard flows are indeed characterized by a periodic large-scale circulation of the flow with large associated time scales. A sufficient number of statistically independent samples is necessary for an accurate measurement of the time-mean velocity ($\overline{u}$), from instantaneous velocity fields (u_i).

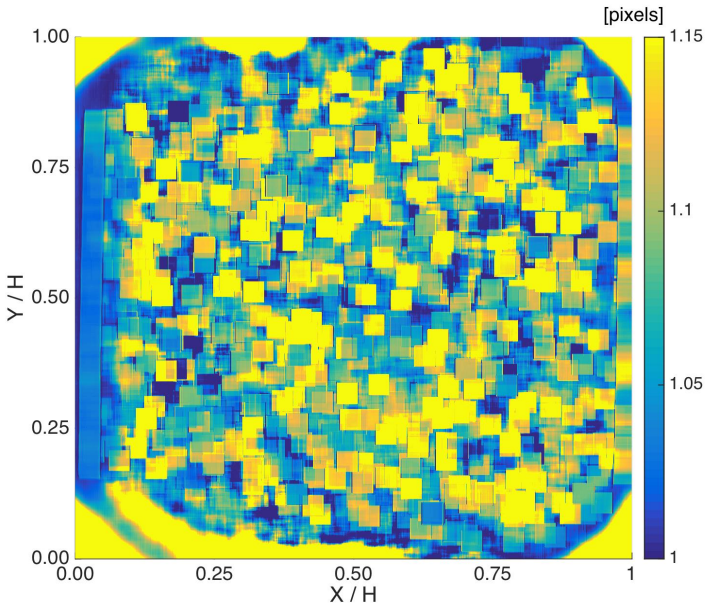


Figure 5.22: Ratio between the cross-correlation function at a specific location and its value at $\pm$ 1 pixel from that location, for the SC_{liquid} PIV instantaneous measurement of Figure 5.21.

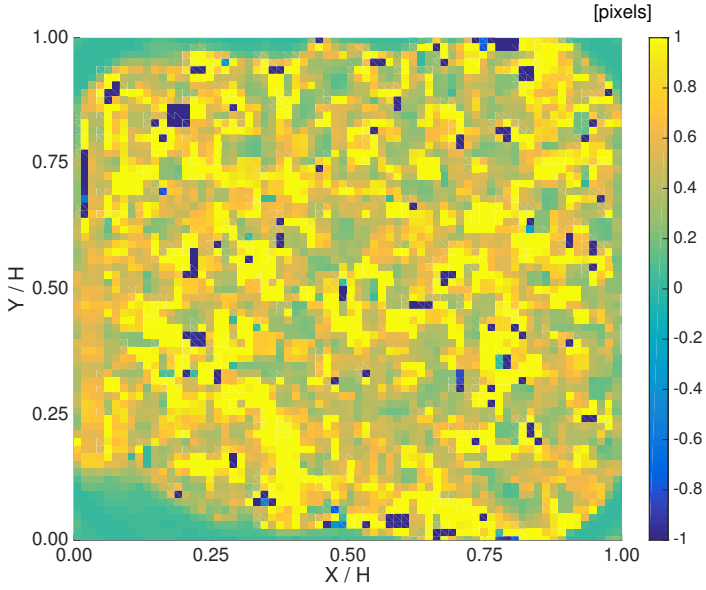


Figure 5.23: Estimation of the velocity uncertainty in the horizontal direction, for the SC_{liquid} PIV instantaneous measurement of Figure 5.21.

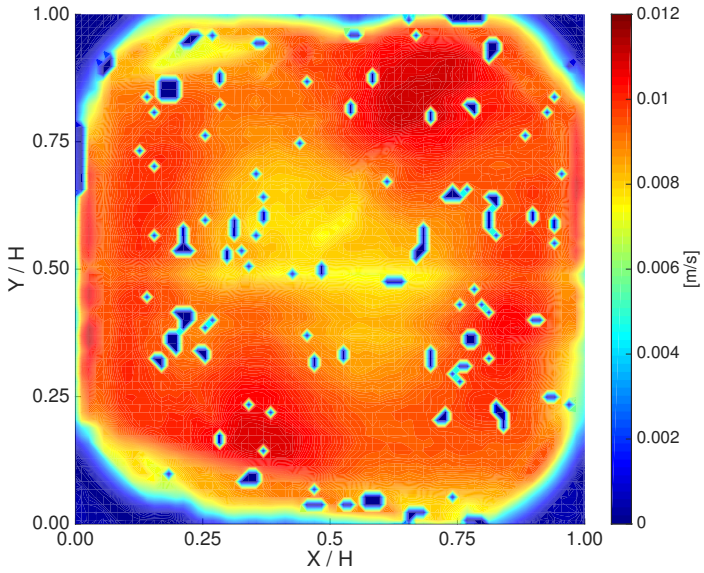


Figure 5.24: Standard deviation in time of the SC_{liquid} PIV experiment. Points where the uncertainty estimation made with Wieneke's method [20] is not valid were not used for the standard deviation calculation and their value was set to zero.

Table 5.3: Statistical relative uncertainties of the large-scale circulation velocity for the experiments PIV SC_{liquid}, PIV $SC_{max\Delta\rho}$ and PIV SC_{gas}, computed in a region of 10×15 data points centered in $X/H \simeq 0.9$ and $Y/H \simeq 0.5$; mean velocity, $\overline{u(X',Y')}$ and $std(\overline{u(X',Y')})$ in a region, (X',Y'), of 10×15 data points centered in $X/H \simeq 0.9$ and $Y/H \simeq 0.5$.

	PIV SC_{liquid}	PIV $SC_{max\Delta\rho}$	PIV SC_{gas}
$\delta(\overline{u(X',Y')})$	3%	1.7%	3.7%
$\overline{u(X',Y')}$ [mm/s]	13	19	6.5
$std(u(X',Y'))$ [mm/s]	5.11	5.04	2.18

The local statistical uncertainty on the mean velocity ($\delta\overline{u(X',Y')}$) was calculated as:

$$\delta(\overline{u(X',Y')}) = \frac{std(u(X',Y'))}{\overline{u(X',Y')}\sqrt{n}}, \tag{5.13}$$

where n is the number of uncorrelated samples, which is estimated by:

$$n = \frac{N}{\frac{4\times H}{\overline{u(X',Y')}}f}, \tag{5.14}$$

and $N = 10800$ is the number of samples acquired at the frequency of $f = 3$ Hz. $\frac{4\times H}{\overline{u(X',Y')}}$ represents the turnover time of the flow, τ, based on $\overline{u(X',Y')}$. $\overline{u(X',Y')}$ is computed with formula (5.7) and $std(u(X',Y'))$ with formula (5.6). Equation (5.13) is based on local velocity values. The region chosen for its calculation, (X',Y'), is within a rectangle of 10×15 data points centered in $X/H \simeq 0.9$ and $Y/H \simeq 0.5$. The spatial average of the velocity over this region represents the velocity of the downward flow along the side wall, which is a measure for the large-scale circulation of the flow. Its velocity values over the number of turnover times τ for the three experiments are shown in Figures 5.25, 5.27 and 5.29, in order to show their time-convergence. From the same figures a constant direction of the LSC of the flow can be seen. Figures 5.26, 5.28 and 5.30 are zoom-in of Figures 5.25, 5.27 and 5.29, respectively, over five turnover times. Time correlations of the experiments SC_{liquid}, $SC_{max\Delta\rho}$, and SC_{gas}, in the region (X',Y') are shown in Figures 5.31, 5.32, and 5.33, respectively. From them it can be seen that while a periodicity is clear for the experiments SC_{liquid} and $SC_{max\Delta\rho}$, it cannot be clearly seen in the case SC_{gas}. This is probably due to a larger integral time-scale of the flow and probably a larger number of samples is needed for a more accurate estimation of its periodicity.

Table 5.3 summarizes the statistical uncertainty $\delta\overline{u(X'Y')}$ on the large-scale circulation velocity of the three PIV experiments, the values of the velocity of the upward flow $\overline{u(X',Y')}$ in a region, (X',Y'), centered in $X/H \simeq 0.9$ and $Y/H \simeq 0.5$, and their the standard deviation values, $std(u(X',Y'))$, which were used for the calculation of $\delta(\overline{u(X',Y')})$.

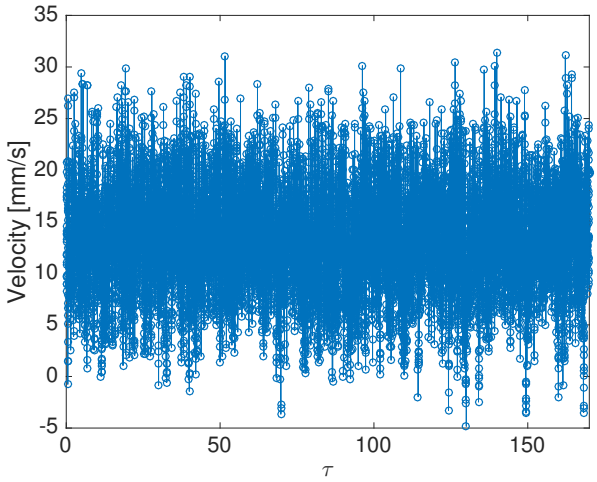


Figure 5.25: Velocity in a rectangular region of 10×15 data points centered in $X/H \simeq 0.9$ and $Y/H \simeq 0.5$ over the number of turnover times τ for the experiment SC_{liquid} ($Ra_{NOB=}5.44 \times 10^{11}$, $Pr_{NOB} = 4.89$). The spatial-mean velocity in this region represents the velocity of the downward flow along the side wall, which is a measure for the large-scale circulation of the flow.

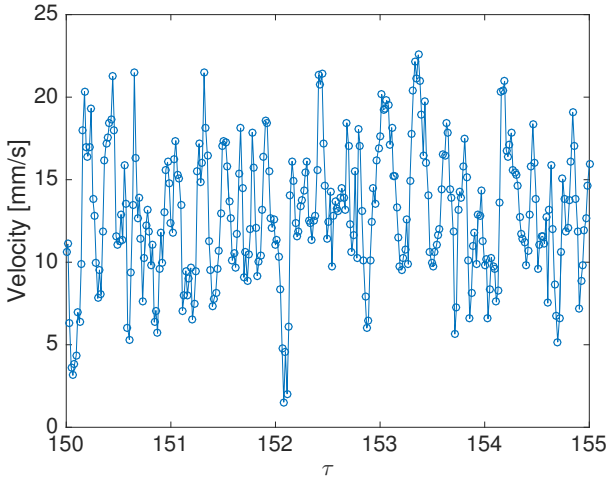


Figure 5.26: Zoom-in of Figure 5.25 for $150 < \tau < 155$. Velocity in a rectangular region of 10×15 data points centered in $X/H \simeq 0.9$ and $Y/H \simeq 0.5$ over the number of turnover times τ for the experiment SC_{liquid} ($Ra_{NOB=}5.44 \times 10^{11}$, $Pr_{NOB} = 4.89$).

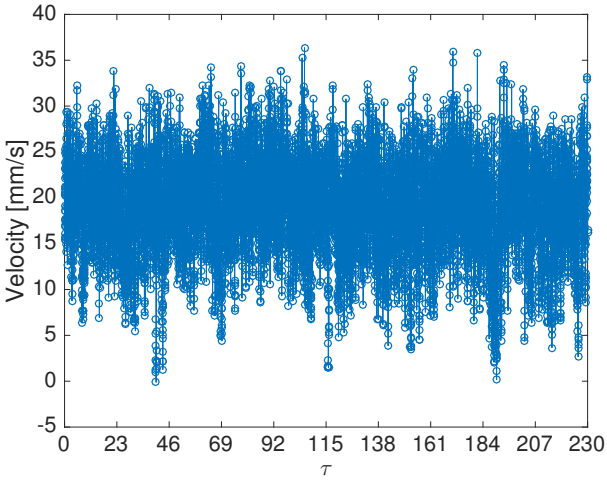


Figure 5.27: Velocity in a rectangular region of 10×15 data points centered in $X/H \simeq 0.9$ and $Y/H \simeq 0.5$ over the number of turnover times τ for the experiment $SC_{max\Delta\rho}$ ($Ra_{NOB} = 3.14{\times}10^{12}$, $Pr_{NOB} = 9.41$). The spatial-mean velocity in this region represents the velocity of the downward flow along the side wall, which is a measure for the large-scale circulation of the flow.

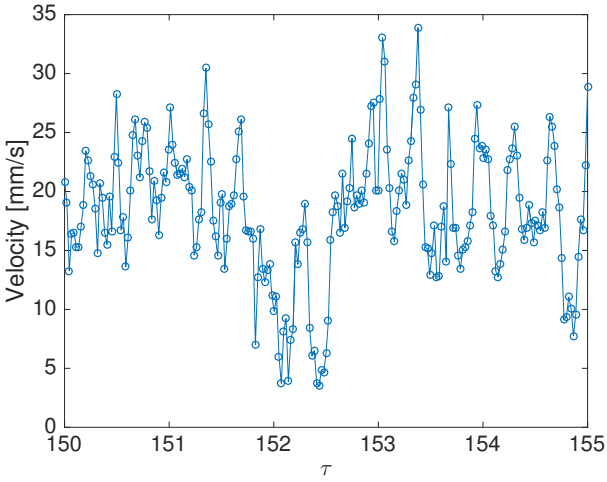


Figure 5.28: Zoom-in of Figure 5.27 for $150 < \tau < 155$. Velocity in a rectangular region of 10×15 data points centered in $X/H \simeq 0.9$ and $Y/H \simeq 0.5$ over the number of turnover times τ for the experiment $SC_{max\Delta\rho}$ ($Ra_{NOB} = 3.14 \times 10^{12}$, $Pr_{NOB} = 9.41$).

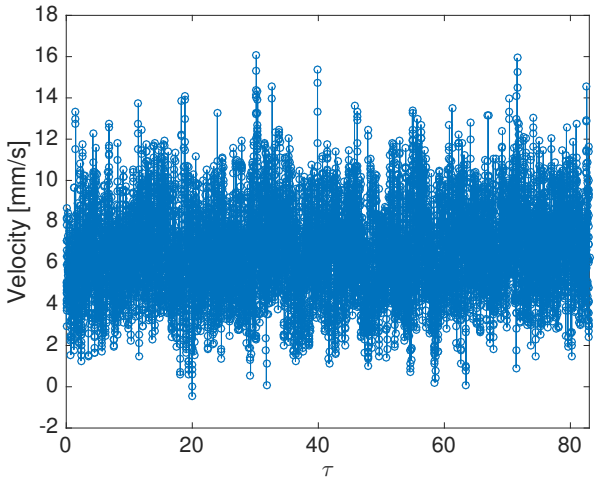


Figure 5.29: Velocity in a rectangular region of 10×15 data points centered in $X/H \simeq 0.9$ and $Y/H \simeq 0.5$ over the number of turnover times τ for the experiment SC_{gas} ($Ra_{NOB} = 5.33 \times 10^{11}$, $Pr = 4.15$). The spatial-mean velocity in this region represents the velocity of the downward flow along the side wall, which is a measure for the large-scale circulation of the flow.

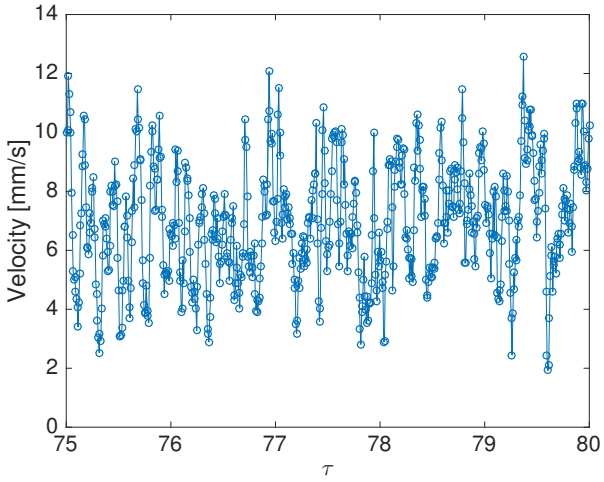


Figure 5.30: Zoom-in of Figure 5.29 for $75 < \tau < 80$. Velocity in a rectangular region of 10×15 data points centered in $X/H \simeq 0.9$ and $Y/H \simeq 0.5$ over the number of turnover times τ for the experiment SC_{gas} ($Ra_{NOB} = 5.33 \times 10^{11}$, $Pr = 4.15$).

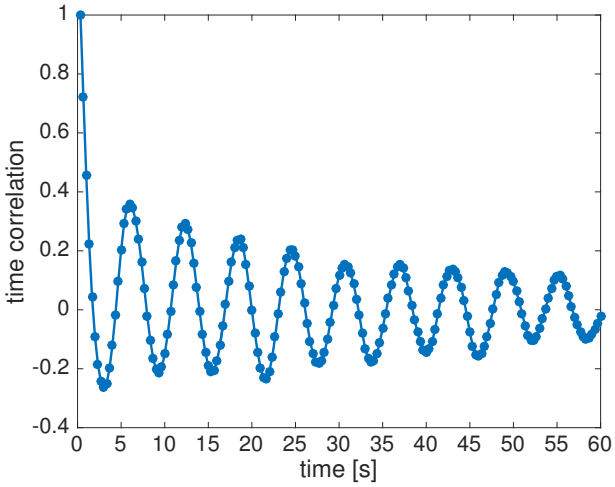


Figure 5.31: Time-correlation of the velocity in a rectangular region, (X',Y'), of 10×15 data points centered in $X/H \simeq 0.9$ and $Y/H \simeq 0.5$, for the experiment SC_{liquid} ($Ra_{NOB=}5.44\times10^{11}$, $Pr_{NOB} = 4.89$).

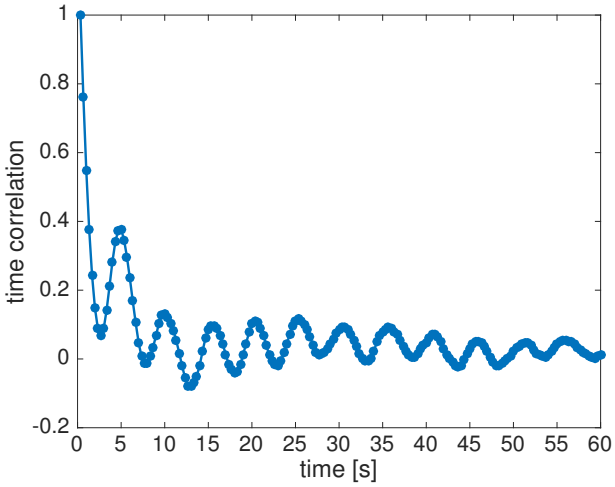


Figure 5.32: Time-correlation of the velocity in a rectangular region, (X',Y'), of 10×15 data points centered in $X/H \simeq 0.9$ and $Y/H \simeq 0.5$, for the experiment $SC_{max\Delta\rho}$ ($Ra_{NOB} = 3.14 \times 10^{12}$, $Pr_{NOB} = 9.41$).

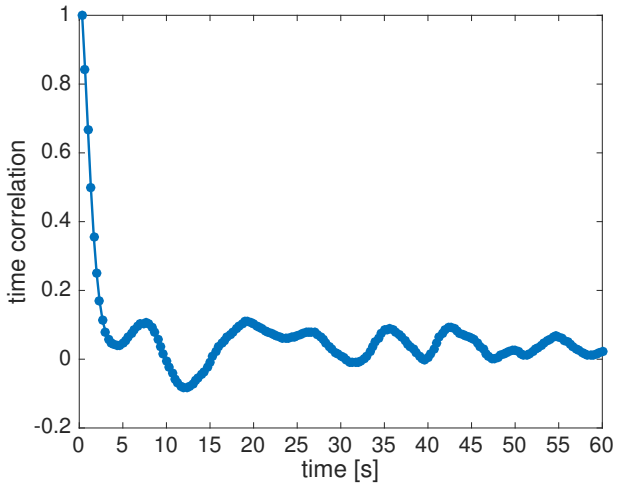


Figure 5.33: Time-correlation of the velocity in a rectangular region, (X',Y'), of 10×15 data points centered in $X/H \simeq 0.9$ and $Y/H \simeq 0.5$, for the experiment SC_{gas} ($Ra_{NOB} = 5.33 \times 10^{11}$, $Pr = 4.15$).

5.8.6. PIV measurements

Time-average velocity fields at the experimental conditions SC_{liquid}, $SC_{max\Delta\rho}$ and SC_{gas} summarized in Table 5.2 are shown in Figures 5.34, 5.35 and 5.36, respectively. The time average was made over one-hour long measurements with an acquisition frequency f of 3 frames/seconds, which corresponds to 10800 samples, as explained in Section 5.4. No preprocessing of the rough images was done, except for the experiment SC_{gas}, where a time-averaged local minimum image was subtracted from the camera recordings. This was necessary to better distinguish the particles from the background.

One large-scale-circulation roll, the typical average flow structure under Oberbeck-Boussinesq (OB) conditions [2, 22], is visible also in these experiments at supercritical conditions, but in this case the top and bottom part of the velocity plots are different. Since the flow direction was clockwise for the experiment SC_{liquid} and anti-clockwise for the other two cases, Figure 5.34 was mirrored with respect to the vertical axis Y. The shape of the velocity field of Figure 5.34 is very similar to the one of Figure 5.35. This shows that their asymmetric structure is not an artifact of the experimental set-up, otherwise it would have been difficult to find a good correspondence between them, after mirroring one of them. The experiment SC_{liquid} (Fig. 5.34) is the case with the largest magnitude of the large-scale circulation (LSC) velocity.

There are two regions with low velocity values in all three experiments, but while they are in the same position with respect to the direction of the flow for the experiments SC_{liquid} and $SC_{max\Delta\rho}$, in the experiment SC_{gas} they are in a different position. More specifically in Figures 5.34 and 5.35 the two regions with low veloc-

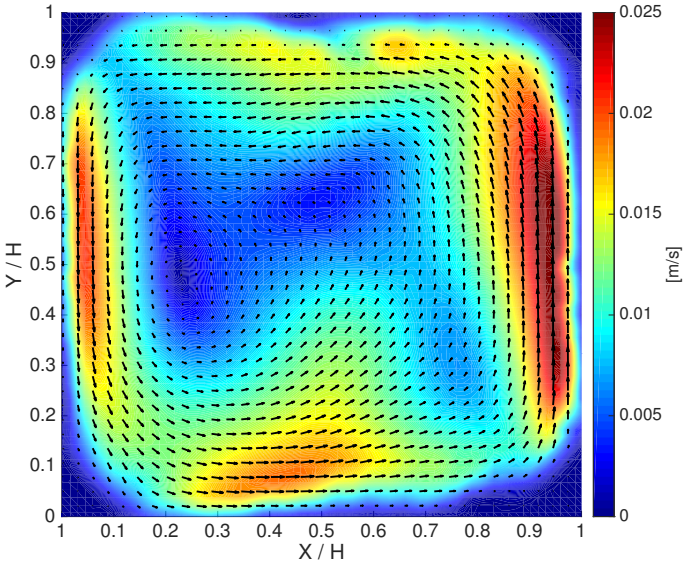


Figure 5.34: Time averaged velocity field of the PIV experiment SC_{liquid}.$Ra_{NOB=}5.44\times10^{11}$, Pr_{NOB} = 4.89. The color scale indicates the magnitude of the mean velocity $\overline{u}$, while the arrows show its direction. Only one arrow every four data points is plotted.

ity values are approximately symmetrical with respect to a diagonal of the square cross-section, while in Figure 5.36 they are approximately symmetrical with respect to a vertical axis in the middle of the measurement section. The presence of two low velocity regions in the time averaged velocity fields suggests that the instantaneous large-scale-flow structure is probably more complex than just one big roll. Table 5.4 presents the values of the large-scale circulation velocities of the flow (U_{LSC}). U_{LSC} can be defined in several ways, as summarized in Pandey *et al.* [23]. In this case U_{LSC} was taken from the experimental data as the absolute value of the maximum of the vertical velocity. The value of the peak of the vertical velocity is resolved in the horizontal direction (X axis) by at least two or three data points. The same definition of U_{LSC} was used also in Chapter 2. Table 5.4 also summarizes the corresponding Rayleigh and Prandtl numbers, defined for non-Oberbeck-Boussinesq (NOB) conditions as in equations (2.3) and (2.4) of Chapter 2. All the fluid properties in the non-dimensional numbers were taken at the average top-bottom temperature of the cell (T_m). For the same Rayleigh and Prandtl numbers of the experiments, Table 5.4 reports also the values of $U_{LSC(GL)}$ computed from the Grossmann-Lohse (GL) theory [24–26] with updated coefficients from Stevens *et al.* [27]; see Section 2.3. The $U_{LSC(GL)}$ values match the experimental U_{LSC} values quite well, considering that the GL theory assumes OB conditions. The largest differences between the theory and the measured ones are for the experiments SC_{liquid} and SC_{gas}, where the velocities are respectively underestimated and overestimated. The Pandey *et*

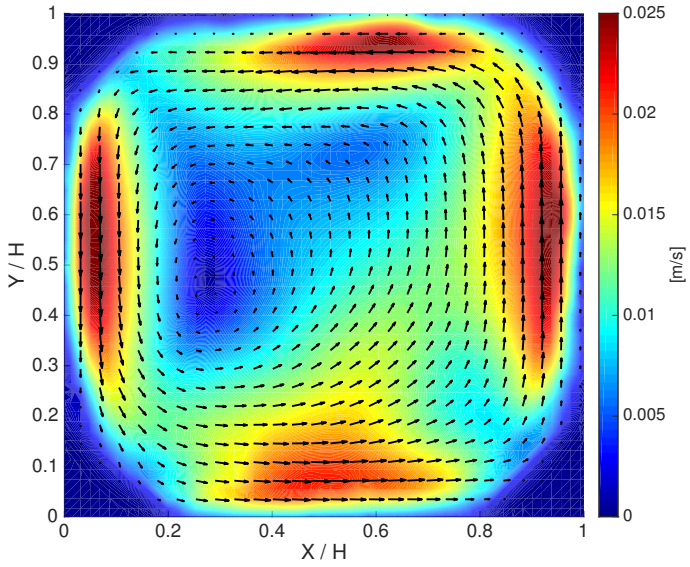


Figure 5.35: Time averaged velocity field of the PIV experiment $SC_{max\Delta\rho}$. $Ra_{NOB} = 3.14 \times 10^{12}$, $Pr_{NOB} = 9.41$. The color scale indicates the magnitude of the mean velocity $\overline{u}$, while the arrows show its direction. Only one arrow every four data points is plotted.

Table 5.4: Rayleigh and Prandtl numbers (defined for non-Oberbeck-Boussinesq conditions as in Formulas (2.3) and 2.4 and U_{LSC} measured in the experiments SC_{liquid}, $SC_{max\Delta\rho}$ and SC_{gas}. $U_{LSC(GL)}$ represents the LSC velocity computed from the Grossmann-Lohse theory, as in Chapter 2, Section 2.3.

	Ra_{NOB}	Pr_{NOB}	U_{LSC} [mm/s]	$U_{LSC(GL)}[mm/s]$
SC_{liquid}	5.44×10^{11}	4.89	27	18.4
$SC_{max\Delta\rho}$	3.14×10^{12}	9.41	27	24
SC_{gas}	5.33×10^{11}	4.15	18	20.2

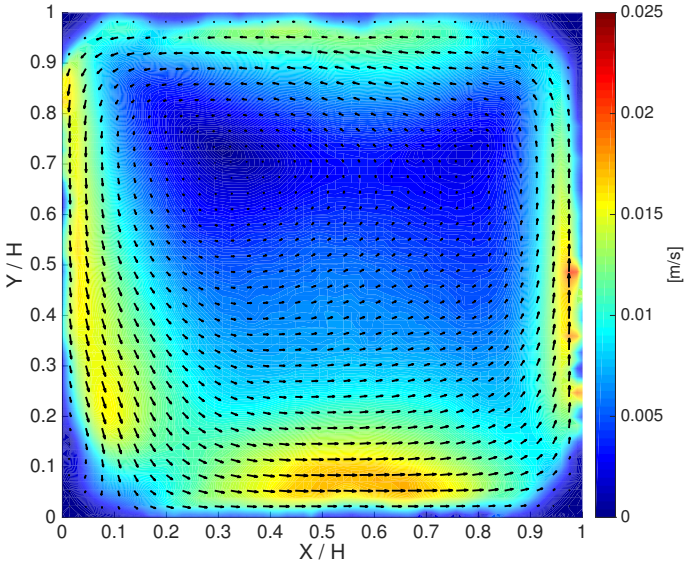


Figure 5.36: Time averaged velocity field of the PIV experiment SC_{gas}. $Ra_{NOB} = 5.33{\times}10^{11}$, $Pr = 4.15$. The color scale indicates the magnitude of the mean velocity $\overline{u}$, while the arrows show its direction. Only one arrow every four data points is plotted.

al. model, [23, 28] did not provide a reliable estimation of U_{LSC} under the studied SC conditions with strong fluid-property changes, probably because its coefficients were not experimentally validated close to the critical point, as it is the case for the GL theory.

Table 5.4 shows that U_{LSC} is smaller for the experiment SC_{gas} with respect to the other two cases, even when it is characterized by approximately the same non-dimensional numbers of the experiment SC_{liquid}. This may be related to differences in the flow structure. The shape of the large-scale circulation roll is different in the two cases. Also the regions with low velocity values are at different locations as previously observed. This difference in large-scale circulation velocity may be explained by the temperature dependency of the fluid properties. Figure 5.13 shows that the isobaric thermal expansion coefficient α is larger at the bottom of the cell than at the top, for experiment SC_{liquid}, enhancing thermal convection. For the experiment SC_{gas} the α dependency on temperature is reversed, and this opposes thermal convection. Looking also at the temperature dependency of other fluid properties, the situation seems more complex. In particular, the other two properties that contribute to the Rayleigh number, the kinematic viscosity ν, and the thermal diffusivity κ are shown in Figures 5.37 and 5.38, respectively. The slope of their temperature dependency is the opposite in experiment SC_{liquid} with respect to experiment SC_{gas}. However, it does not seem evident whether the positive or

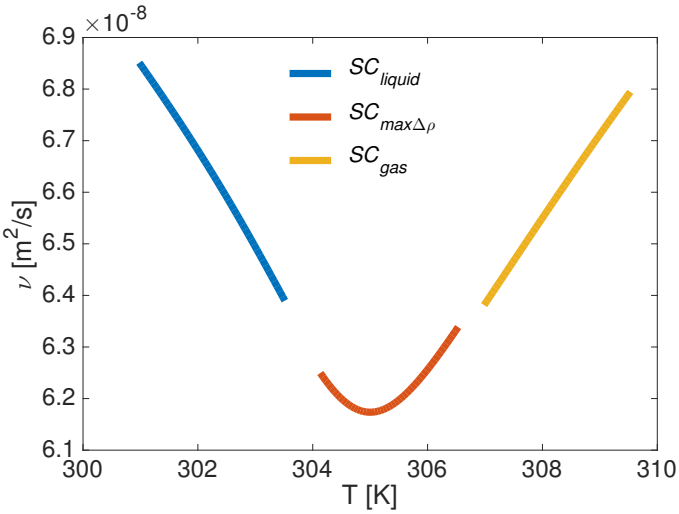


Figure 5.37: Kinematic viscosity (ν) values as a function of temperature for the three PIV experiments SC_{liquid}, $SC_{max\Delta\rho}$ and SC_{gas}. Values taken from the CoolProp database [17].

negative slope of a single fluid property by itself can be responsible for an enhanced or reduced large-scale circulation of the flow. For this reason also the temperature dependency of the ratio $\frac{\alpha}{\nu\kappa}$, which is contained in the Rayleigh number, was considered in Figure 5.39. The temperature dependency of $\frac{\alpha}{\nu\kappa}$ on temperature has the same slope of the one of α of Figure 5.13, and this can explain the difference between the U_{LSC} of experiment SC_{liquid} and SC_{gas}. Even if the two cases are characterized by the same non-dimensional numbers, Ra_{NOB} and Pr_{NOB}, the slope of the temperature dependency of the fluid property ratio $\frac{\alpha}{\nu\kappa}$, in one case enhances thermal convection, while in the other one it reduces it. More specifically, when $\frac{\alpha}{\nu\kappa}$ is larger at the bottom of the cell than at the top, like in the experiment SC_{liquid}, it enhances thermal convection, while when it is smaller at the bottom than at the top, like in the experiment SC_{gas}, it reduces convection. The experiment $SC_{max\Delta\rho}$ is characterized by different Ra_{NOB} and Pr_{NOB} than the other two cases, hence it is not possible to compare its U_{LSC} with the other two directly.

Figures 5.40, 5.41 and 5.42 show three instantaneous flow fields of the PIV experiments SC_{liquid}, $SC_{max\Delta\rho}$ and SC_{gas}, respectively. The regions with large velocity magnitudes can be localized quite well in the three cases, and this may show a preference of the plumes to agglomerate. This can be seen indeed also in the BOS instantaneous images of Figures 5.17, 5.18 and 5.19, where the regions with the largest displacements are also localized. It is interesting to observe in Figure 5.42 that there is a region with large velocity magnitudes on the left part of the measurement section for $0.2 \simeq Y/H \simeq 0.4$. This may be a high velocity plume that goes through the measurement region, showing a complex 3D structure of the flow. The orientation of the large scale circulation under Oberbeck-Boussinesq conditions [2, 22] is locked in a dominant direction on a diagonal of the cube [29]. The

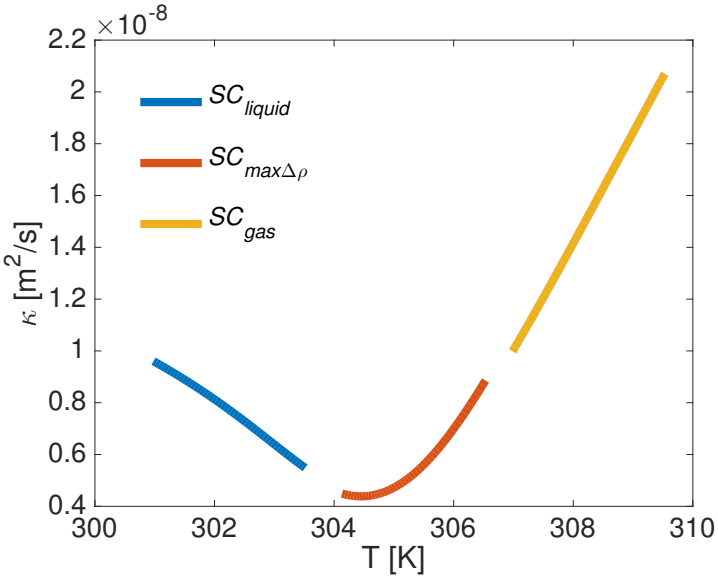


Figure 5.38: Thermal diffusivity (κ) values as a function of temperature for the three PIV experiments SC_{liquid}, $SC_{max\Delta\rho}$ and SC_{gas}. Values taken from the CoolProp database [17].

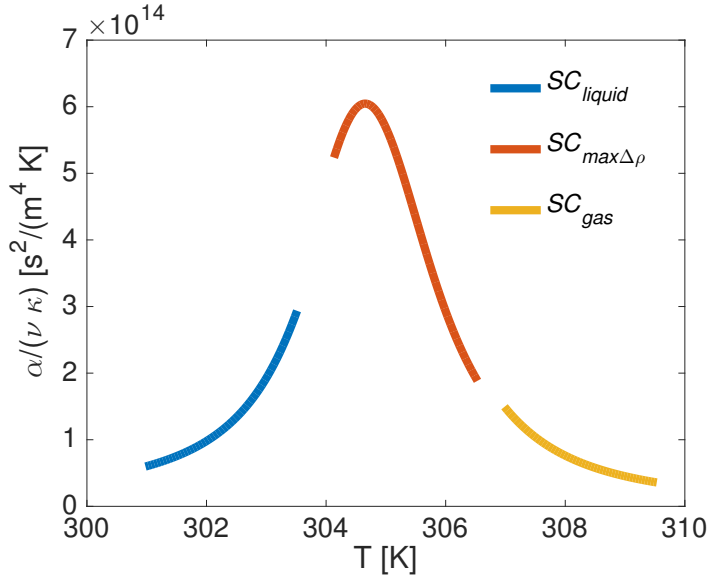


Figure 5.39: Ratio between the isobaric thermal expansion coefficient α and the product of the kinematic viscosity (ν) with the thermal diffusivity (κ) as a function of temperature for the three PIV experiments SC_{liquid}, $SC_{max\Delta\rho}$ and SC_{gas}. Values taken from the CoolProp database [17].

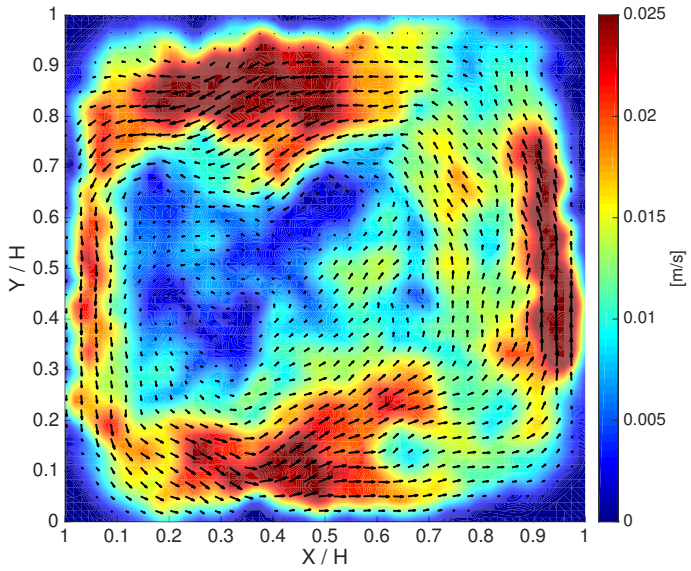


Figure 5.40: Instantaneous velocity field of the PIV experiment SC_{liquid}. $Ra_{NOB} = 5.33 \times 10^{11}$, $Pr = 4.15$. The color scale indicates the magnitude of the instantaneous velocity, while the arrows show its direction. Only one arrow every four data points is plotted.

smaller values of the U_{LSC} in the measurement section for the experiment SC_{gas} with respect to the other two cases considered, may be due to a more complex 3D circulation. To further study the physics of the flow and compute normal and Reynolds stresses, it is necessary to improve the quality of the velocity measurements. For example, as above cited, with an accurate control of the concentration of the tracer particles within the measurement volume.

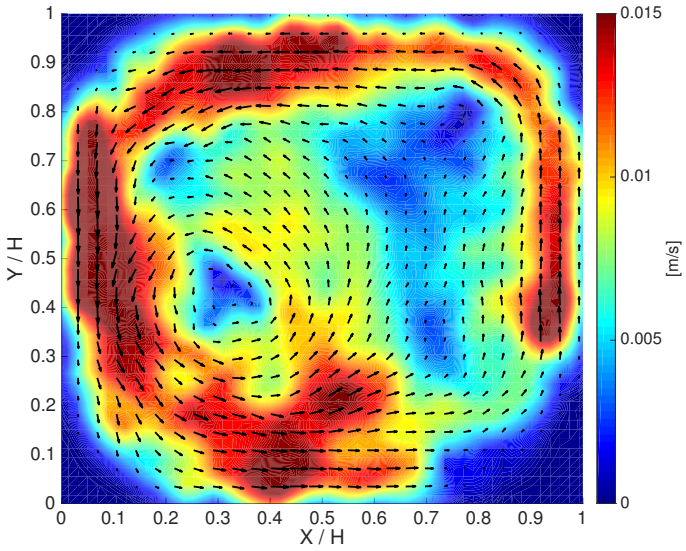


Figure 5.41: Instantaneous velocity field of the PIV experiment $SC_{max\Delta\rho}$. $Ra_{NOB} = 3.14 \times 10^{12}$, $Pr_{NOB} = 9.41$. The color scale indicates the magnitude of the instantaneous velocity, while the arrows show its direction. Only one arrow every four data points is plotted.

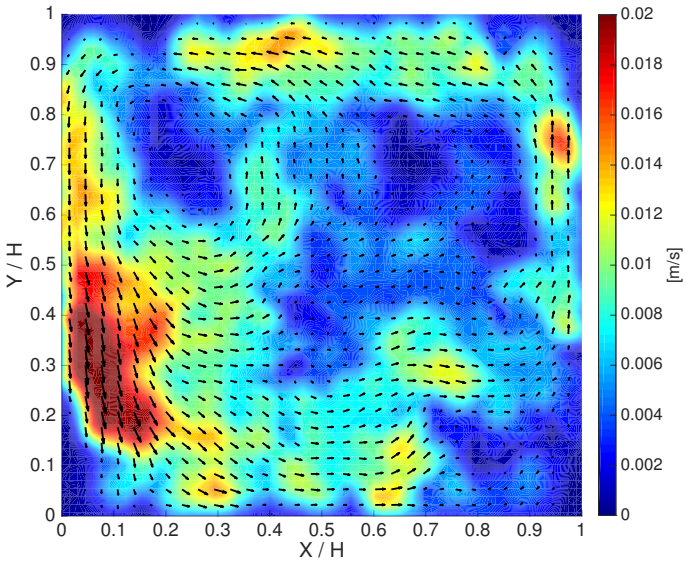


Figure 5.42: Instantaneous velocity field of the PIV experiment SC_{gas}. $Ra_{NOB} = 5.33 \times 10^{11}$, $Pr = 4.15$. The color scale indicates the magnitude of the instantaneous velocity, while the arrows show its direction. Only one arrow every four data points is plotted.

5.9. Conclusions

PIV measurements of a supercritical fluid in Rayleigh-Bénard convection were presented. A preliminary BOS study was performed to quantify the effects of strong density changes within the flow, which lead to strong optical distortions. It was found that for the present experimental conditions, blurring due to optical distortions did not obstructed the visualization of the particles, except in the boundary layer regions.

The experimental conditions for the PIV experiments were chosen to study different parts of the $\rho(T)$ versus T curve at constant pressure. Three experiments were done in the supercritical region, one at lower temperatures, towards the liquid phase, one at higher temperatures towards the gas phase and one in between. The latter is also characterized by the sharpest change of density from the bottom to the top of the cell.

It was observed that:

- the mean velocity fields show the presence of a large-scale circulation roll for all three cases. This large-scale flow structure is typical of Rayleigh-Bénard convection;
- the position of regions with low velocities and the magnitude of the LSC velocity of the flow are different in the PIV experiment near the gas phase with respect to the other two cases. More specifically, in the SC_{liquid} and in the $SC_{max\Delta\rho}$ experiments there are two local minimums at the center of the cell, approximately at $X/H \simeq 0.25$ and $Y/H \simeq 0.5$, and at $X/H \simeq 0.5$ and $Y/H \simeq 0.65$, while in the SC_{gas} case they are approximately at $X/H \simeq 0.3$ and $Y/H \simeq 0.75$, and at $X/H \simeq 0.8$ and $Y/H \simeq 0.75$;
- the LSC velocity of the experiment near the gas phase is smaller than the one of the experiment near the liquid phase, even if they are characterized by approximately the same Rayleigh and Prandtl numbers. The reason for this difference in LSC velocities can be found in the temperature dependency of the fluid properties that constitutes the Rayleigh number;
- in the experiment near the liquid phase, this ratio is larger at the bottom of the cell than at the top, enhancing thermal convection; while in experiment near the gas phase, it is smaller at the bottom than at the top, reducing thermal convection;
- the uncertainty of the PIV-measured LSC velocity was estimated using the method proposed by Wieneke *et al.* [20]. The major source of errors in the PIV measurements was due to the presence of very bright particles in only one of the two frames used for the velocity quantification. This may be due to out of plane motion and to optical distortions;
- in the present measurements the uncertainty in the LSC velocity due to statistical convergence was estimated of about 3% for all the three cases.

The visualization of the velocity fields of Rayleigh-Bénard convection and the measurement of the LSC velocity of the flow at different locations in the pressure versus temperature space, complement the heat transfer study at supercritical conditions presented in Chapter 3. The smaller LSC velocity measured in the experiment towards the gas phase with respect to the experiment towards the liquid phase, at the same non dimensional NOB Rayleigh and Prandtl numbers, can be the reason of the observed decrease in the Nusselt number trend of the data towards the gas phase after a threshold value.

References

[1] S. Ashkenazi and V. Steinberg, *High Rayleigh Number Turbulent Convection in a Gas near the Gas-Liquid Critical Point,* Physical Review Letters **83** (1999).

[2] J. Boussinesq, *Théorie analytique de la chaleur*, Vol. 2 (Gauthier-Villars (Paris), 1903).

[3] J. Licht, M. Anderson, and M. Corradini, *Characteristics in supercritical pressure water,* Journal of Heat Transfer **131**, 072502(1 (2009).

[4] G. E. Elsinga, B. W. van Oudheusden, and F. Scarano, *Evaluation of aero-optical distortion effects in PIV,* Experiments in Fluids **39**, 246 (2005).

[5] M. J. Murphy and R. J. Adrian, *PIV space-time resolution of flow behind blast waves,* Experiments in Fluids **49** (2010).

[6] G. E. Elsinga and G. C. Orlicz, *Particle imaging through planar shock waves and associated velocimetry errors,* Experiments in Fluids **56** (2015).

[7] J. Westerweel, G. E. Elsinga, and R. J. Adrian, *Particle image velocimetry for complex and turbulent flows,* Annual Review of Fluid Mechanics **45**, 409 (2013).

[8] R. J. Adrian, *Particle-imaging techniques for experimental fluid mechanics,* Annual Review of Fluid Mechanics **23**, 261 (1991).

[9] R. J. Adrian and J. Westerweel, *Particle Image Velocimetry*, edited by Cambridge University Press, Cambridge Aerospace Series (Cambridge University Press, 2011).

[10] M. Raffael, C. Willert, S. Wereley, and J. Kompenhans, *Particle Image Velocimetry*, second edition ed., edited by Springer (Springer-Verlag Berlin Heidelberg).

[11] W. Merzkirch, *Flow Visualization* (Academic Press London, 1987).

[12] R. Mei, *Flow due to an oscillating sphere and an expression for unsteady drag on the sphere at finite reynolds number,* Journal of Fluid Mechanics **270**, 133 (1994).

[13] R. Mei, *Velocity fidelity of flow tracer particles,* Experiments in Fluids **22**, 1 (1996).

[14] A. Melling, *Tracer particles and seeding for particle image velocimetry,* Measurement Science and Technology **8**, 1406 (1997).

[15] H. Richard and M. Raffel, *Principle and applications of the background oriented schlieren (BOS) method,* Measurement Science and Technology **12**, 1576 (2001).

[16] G. E. Elsinga, B. v. Oudheusden, F. Scarano, and D. Watt, *Assessment and application of quantitative schlieren methods: Calibrated color schlieren and background oriented schlieren,* Experiments in Fluids **36**, 309 (2004).

[17] I. H. Bell, J. Wronski, S. Quoilin, and V. Lemort, *Pure and pseudo-pure fluid thermophysical property evaluation and the open-source thermophysical property library coolprop,* Industrial & Engineering Chemistry Research **53**, 2498 (2014).

[18] M. V. Avdeev, A. N. Konovalov, V. N. Bagratashvili, V. K. Popov, S. I. Tsypina, M. Sokolova, J. Ke, and M. Poliakoff, *The fibre optic reflectometer: A new and simple probe for refractive index and phase separation measurements in gases, liquids and supercritical fluids,* Physical Chemistry Chemical Physics **6**, 1258 (2004).

[19] J. Westerweel, *On velocity gradients in PIV interrogation,* Experiments in Fluids **44**, 831 (2008).

[20] B. Wieneke, *PIV uncertainty quantification from correlation statistics,* Measurement Science and Technology **26**, 074002(10pp) (2015).

[21] A. Sciacchitano, B. Wieneke, and F. Scarano, *PIV uncertainty quantification by image matching,* Measurement Science and Technology **24**, 045302 (16pp) (2013).

[22] A. Oberbeck, *Ueber die Wärmeleitung der Flüssigkeiten bei Berücksichtigung der Strömungen infolge von Temperaturdifferenzen,* Annalen der Physiks **243**, 271 (1879).

[23] A. Pandey and M. K. Verma, *Scaling of large-scale quantities in Rayleigh-Bénard convection,* Physics of Fluids **28**, 095105 (2016).

[24] S. Grossmann and D. Lohse, *Scaling in thermal convection: a unifying theory,* Journal of Fluid Mechanics **407**, 27 (2000).

[25] S. Grossmann and D. Lohse, *Thermal convection for large Prandtl numbers,* Physical Review Letters **86**, 3316 (2001).

[26] S. Grossmann and D. Lohse, *Prandtl and Rayleigh number dependence of the Reynolds number in turbulent thermal convection,* Physical Review E **66**, 016305 (2002).

[27] R. J. Stevens, E. P. van der Poel, S. Grossmann, and D. Lohse, *The unifying theory of scaling in thermal convection: the updated prefactors,* Journal of Fluid Mechanics **730**, 295 (2013).

[28] A. Pandey, A. Kumar, A. G. Chatterjee, and M. K. Verma, *Dynamics of large-scale quantities in Rayleigh-Bénard convection,* Physical Review E **94**, 053106 (2016).

[29] G. Ahlers, S. Grossmann, and D. Lohse, *Heat transfer and large scale dynamics in turbulent Rayleigh-Bénard convection,* Reviews of Modern Physics **81**, 503 (2009).

6

Summary and perspectives

6.1. Summary

In this thesis the effect of variable properties on the heat transfer and velocity field of Rayleigh-Bénard (RB) convection at supercritical (SC) conditions was experimentally studied.

6.1.1. Velocity field with strongly temperature-dependent variable properties

The effect of strongly temperature-dependent variable properties was examined for RB convection at atmospheric pressure first. Particle image velocimetry (PIV) was applied to determine the velocity fields of two different cases. One case with strongly temperature-dependent fluid properties, which for this reason does not respect the assumptions of the Oberbeck-Boussinesq (OB) approximation [1, 2]. The working fluid used in this case was water. The other case studied was with a negligible temperature-dependency of the fluid properties and it was considered as a reference for OB conditions. The working fluid used in this case was methanol. Both experiments were performed at similar non-dimensional Rayleigh and Prandtl numbers. Different flow fields were observed in the two cases. In the non-OB case a significant asymmetry emerged between the bottom and the top part of the cell. The time-averaged horizontal velocity values at the bottom of the cell were about 13% larger than the ones at the top of the cell. The difference is larger than the experimental uncertainty, which was estimated to be about 3%. This was mainly caused by the strong temperature-dependency of the kinematic viscosity of water at the present experimental conditions (about 50% difference between its value at the top and at the bottom of the cell). This finding confirmed the so-called "broken symmetry" in the velocity field, which was observed in earlier theoretical and numerical studies, but until now not experimentally demonstrated. [3–5].

6.1.2. Heat transfer measurements at supercritical conditions

The heat transfer in a RB-cell at SC conditions was experimentally studied. Several data points were acquired at constant global Rayleigh and Prandtl numbers, along a so-called 'closed line'. This closed line can be ideally divided into two branches, with opposite sign of the difference between the local Prandtl number values at the top and at the bottom of the cell. It was found that the heat transfer through the cell, expressed as a Nusselt number, is different at different locations along the considered closed line, even if the global Rayleigh and Prandtl numbers were constant. The maximum difference in the measured Nusselt numbers was about 16%, which is larger than the experimental uncertainty, which was estimated at 2.6%. This shows that the global Rayleigh and Prandtl numbers are not sufficient to predict the heat transfer through the cell at SC conditions, as is the case under OB conditions. Also, other factors play a role in the determination of the heat transfer. Probably the strong temperature and pressure dependencies of the fluid properties, which are not taken into account in the global Rayleigh and Prandtl numbers, may be the cause of the observed heat transfer behavior. It was also found that the Nusselt number dependency on the top-bottom relative difference of the fluid properties is different for one branch of the constant Prandtl line, compared to the other branch. Along one branch the Nusselt dependency was monotonic, while along the other it exhibited a maximum. This shows that not only the magnitude of the relative difference of the fluid properties between the top and the bottom of the cell is important, but also its sign. Finally it was seen that the measured Nusselt number was always larger than the prediction by the Grossmann-Lohse (GL) theory for OB conditions. The difference between the lowest measured Nusselt number and the GL prediction was about 16%, which indicates a significant heat-transfer increase at SC conditions with respect to OB conditions.

6.1.3. PIV measurements at supercritical conditions

A RB set-up was designed to perform PIV measurements at SC conditions with freon R-23 as a working fluid. The working pressures of this set-up are up to 70 bar and the temperatures of its horizontal plates can be chosen from 20 to 70 °C. This RB-cell is a cube of 7 cm, made of lateral glass-walls for optical access. The most difficult part of the commissioning tests of this facility was to avoid any tension on its fragile internal structure, in the pressurizing and depressurizing phases. Another difficulty concerned the leakage of tracer particles for the PIV measurements outside the measurement volume.

A feasibility study of PIV at SC conditions was made. It was shown by using background oriented schlieren measurements, that the optical distortions due to strongly varying fluid density still allows to perform sufficiently accurate PIV measurements. The order of magnitude of the accuracy of the PIV measurements was estimated using a statistical correlation method proposed by Wieneke *et al.* [6]. Experiments were performed at three different mean pressures and temperatures of the cell. The three cases were characterized by different relative density changes between the top and the bottom of the cell. They were referred to as SC_{liquid},

$SC_{max\Delta\rho}$ and SC_{gas}, because they were located in the SC region close to the liquid phase, in the part with the strongest density gradient, and close to the gas phase, respectively. Two of them, the SC_{liquid} and the SC_{gas} cases, were characterized by an opposite sign of the difference between the local Prandtl number values at the top and at the bottom of the cell. The global NB Rayleigh and Prandtl numbers of both cases were approximately the same. The third case studied, $SC_{max\Delta\rho}$ was located in between the other two cases, in the pressure-temperature space. The time-averaged velocity profiles of the three cases showed the presence of an asymmetric large-scale-circulation (LSC) roll, which covers the entire cross-section of the cell. The LSC velocity of the flow was larger for the case SC_{liquid} than for the case SC_{gas}, even when they were characterized by the same Rayleigh and Prandtl numbers. This finding is coherent with the different Nusselt number regimes found in the two branches of the constant Prandtl number line in Chapter 3. The lower LSC velocity of the SC_{gas} case with respect to the SC_{liquid} case may partially explain the decrease of the Nusselt number of the lower branch of the constant Prandtl number line, after showing its local maximum, when increasing mean temperatures and pressures. The flow structures of the SC_{liquid} and SC_{gas} case were also different. The position and the shape of the regions with lower velocity values in the central part of the cell are different in the case SC_{liquid} with respect to the case SC_{gas}. This is probably due to different three-dimensional (3D) flow structures in the two cases.

6.2. Perspectives

Velocity fields and global heat transfer measurements of RB convection with strongly variable fluid properties at SC conditions were shown in this thesis. Further research is recommended to improve the quality of the PIV measurements in SC fluids with strong density changes. Blurring and out of plane motion of the particles were identified as the main source of errors in the PIV measurements. A more accurate control of the concentration of the tracers particles within the measurement volume would allow to gain more precise velocity measurements. Modifications in the PIV RB set-up can be accomplished for example by filling in the empty spaces between the glass cube and the stainless steel structure. This can block the migration of tracers particles out of the measurement volume that usually happens during the regulation of the pressure of the cell and of the temperatures of the copper plates.

The heat transfer study showed that buoyancy driven heat transfer at SC conditions is larger than predicted for OB conditions. The main difficulties in the heat transfer measurements were due to uncertainties in the quantification of fluid properties values close to the critical point, because of their strong temperature and pressure dependency. A solution could be to investigate Nusselt number regimes at different values of Rayleigh and Prandtl numbers, at SC conditions farther from the critical point, where the sensitivity of the fluid properties on temperature and pressure is smaller. From the physical point of view, research is recommended to explain the non-monotonic behavior of the Nusselt number regime in the lower branch of the constant Prandtl number line studied in Chapter 3. The effect of

opposite signs in the difference of local properties at the top and at the bottom of the cell can be analyzed further with PIV velocity measurements, made at constant global Prandtl and Rayleigh numbers. Also the 3D structures in both cases can be studied to improve the understanding of the interaction between fluid structure and heat transfer. Due to the difficulties in performing accurate optical measurements with strong density changes, a first approach to study the 3D flow structure would be to perform planar PIV measurements in two perpendicular cross-sections of the cube. To incline the cube would also help to fix the 3D flow structure, because it forces the circulation of the flow in a preferred direction.

Improvements in the PIV measurements with strongly variable properties and the acquisition of more heat-transfer data at SC conditions are necessary to understand the main phenomena that were shown to play a crucial role in the heat transfer mechanism at SC conditions [7]. These phenomena are mainly modifications of the viscous and thermal boundary layer thicknesses and turbulence under SC conditions.

References

[1] A. Oberbeck, *Ueber die Wärmeleitung der Flüssigkeiten bei Berücksichtigung der Strömungen infolge von Temperaturdifferenzen,* Annalen der Physiks **243**, 271 (1879).

[2] J. Boussinesq, *Théorie analytique de la chaleur*, Vol. 2 (Gauthier-Villars (Paris), 1903).

[3] G. Ahlers, E. Brown, F. F. Araujo, D. Funfschilling, S. Grossmann, and D. Lohse, *Non-Oberbeck–Boussinesq effects in strongly turbulent Rayleigh–Bénard convection,* Journal of Fluid Mechanics **569**, 409 (2006).

[4] S. Horn, O. Shishkina, and C. Wagner, *On non-Oberbeck–Boussinesq effects in three-dimensional Rayleigh–Bénard convection in glycerol,* Journal of Fluid Mechanics **724**, 175 (2013).

[5] S. Horn and O. Shishkina, *Rotating non-Oberbeck–Boussinesq Rayleigh–Bénard convection in water,* Physics of Fluids **26**, 055111 (2014).

[6] B. Wieneke, *PIV uncertainty quantification from correlation statistics,* Measurement Science and Technology **26**, 074002(10pp) (2015).

[7] J. Y. Yoo, *The turbulent flows of supercritical fluids with heat transfer,* Annual Review of Fluid Mechanics **45**, 495 (2013).

Curriculum Vitæ

Valentina VALORI

1st March 1986	Born in Città di Castello, Italy.
July 2005	Leaving examination with full marks Liceo Scientifico "Città di Piero", Sansepolcro, Italy
Dec. 2008	Batchelor degree in Energy engineering 'cum laude' University of Bologna, Italy
July 2012	Master degree in Energy engineering 'cum laude' University of Pisa, Italy
Oct.2011-Apr.2012	Internship for master thesis preparation Laboratory of Nuclear Energy Systems ETH Zürich, Switzerland
2013-present	Ph.D. candidate Deft University of Technology, The Netherlands *Thesis:* Rayleigh-Bénard convection of a supercritical fluid: PIV and heat transfer study. *Promotors:* Prof. dr. T.H.J.J. van der Hagen and prof. dr. J. Westerweel
Oct.-Dec. 2015	Visitor at the Max Planck Institute for Dynamics and Self-Organization in Göttingen, Germany
Nov.2016-Apr.2017	EuHIT project: "Heat Transfer at Supercritical conditions in Natural Convection" with experimental work developed at the Max Planck Institute for Dynamics and Self-Organization in Göttingen

List of Publications

3. **V. Valori**, G.E. Elsinga, M. Rohde, M. Tummers, J. Westerweel, T-H.J.J. van der Hagen, *Experimental velocity study of non-Boussinesq Rayleigh-Bénard convection*, Physical Review E **95**, pp. 053113 (2017).

2. **V. Valori**,G.E. Elsinga, M. Rohde, M. Tummers, J. Westerweel, T-H.J.J. van der Hagen, *Natural Convection driven heat transfer in fluids with strongly variable properties: a Particle Image Velocimetry study*, NURETH-16, International Topical Meeting on Nuclear Reactor Thermal Hydraulics, Hyatt regency Chicago, August 30^{th}-September 4^{th}, 2015.

1. J. Kickhofel,**V. Valori**,H.-M. Prasser, *Turbulent penetration in T-junction branch lines with leakage flow*, Nuclear Engineering and Design **276**, pp. 43-53, (2014).